Interfacial Syntheses of Nanoelectronic Materials: High-*K* Perovskite Oxides and Electroresponsive Polymeric Systems

by

Kai Su

A dissertation submitted to the Graduate Faculty in Chemistry in partial fulfillment of the requirements for the degree of Doctor of Philosophy The City University of New York.

2007

UMI Number: 3283606

ProQuest Information and Learning Company
300 North Zeeb Road
P.O. Box 1346
Ann Arbor, MI 48106-1346

This manuscript have been read and accepted for the Graduate Faculty in Chemistry in satisfaction of the dissertation requirement for the degree of Doctor of Philosophy.

Nan-Loh Yang

Date — Chair of Examining Committee

Gerald Koeppl

Date — Executive Officer

David C. Locke

Steven A. Schwarz

Supervisory Committee

THE CITY UNIVERSITY OF NEW YORK

Abstract

INTERFACIAL SYNTHESES OF NANOELECTRONIC MATERIALS: HIGH-*K* PEROVSKITE OXIDES AND ELECTRORESPONSIVE POLYMERIC SYSTEMS

by

Kai Su

Mentor: Professor Nan-Loh Yang

The creation of fundamental building elements for Nanoelectronics is considered one of the crucial steps for the development of Nanotechnology. This dissertation reports our original findings in four significant areas: i, a room-temperature synthesis of ferroelectric barium titanate with size control using bolaamphiphile self-assemblies donut as templates; ii, a fabrication STO, BTO nanocrystals and BST nano-solid-solutions of high-quality, controlled size (50–10nm) and high dielectric constant (up to 1.5x 10^4) using an open-bench reverse micelle system; iii, an interfacial polymerization-crystallization for the formation of organic polymer single crystalline nanoneedles capable of fast conductance switching; and iv, a fabrication of STO/PANI nano-composite by reverse micelle for electromechanical applications.

These investigations are based on the exploitation of surface physicochemical principles. The ferroelectric $BaTiO_3$ nanoparticles with tetragonal crystalline structure were grown under ambient conditions inside the peptide-doughnut templates with unusual internal surface properties. Monodisperse nanoparticles between 6 nm and 12 nm were obtained by controlling the pH value of the self-assembly system. The syntheses of PEROVSKITE OXIDES nanocrystals took advantages of the surface boundary of micelles to control the reaction volume and kinetics. Polythiophenes, polyaniline and polypyrrole single crystalline nanoneedles with fast conductance switch properties were synthesized using an interfacial polymerization process with attendant crystallization. The fast conductance switching behavior of these organic polymeric nanoelements is related to their single crystalline nature. A nano-composite, STO/PANI, with insulating shell and strontium titanate embedded in organic conductor core showed a very stable and strong electrorheological effect. The synergistic ER effect observed in the nanocomposites is due to the combination of atomic polarization and electronic polarization.

The advancement of these novel approaches based on surface phenomena can serve as the basis for constructing nanoelectronic elements with a broad range of functions.

This is

dedicated to

My beloved and great family

Acknowledgements

First and foremost, I'd like to give my wholehearted gratitude to my dear mentor, Prof. Nan-Loh Yang, for his inspiring guidance, unconditional devotion, and enlightening instructions in the joyful but challenging journey of my PhD study.

I also own thanks to my research committee members, Prof. David C. Locke and Steven A. Schwarz. This dissertation cannot be so fruitful without their continuous guidance and advice.

As a research collaborator, I own special thanks to Prof. Hiroshi Matsui and Mr. Nurxat Nuraje. Our collaborating has been enjoyable and fruitful.

I own thanks to my colleagues in our lab: Ms. I-Wei Chu, Dr. Lingzhi Zhang, Dr. Ning Chi…

Most of all, I own thanks to my dear family, my parents Mr. Xuewei Su and Ms. Shumin Deng, my sister Ms. Yi Su and her husband Dr. Shaoyuan Li, and my girlfriend Ms. Lin Wang for their sustained passionate support to my PhD study.

I also gratefully acknowledge the financial supports from NSF through the MRSEC for Polymers at Engineered Interfaces, New York State Office of Science Technology Academic Research, through the Center for Engineered Polymeric Materials, CePM, and CUNY-PSC awards.

Table of Contents

List of Figures

List of Tables

List of Schemes

Chapter 1

Overview of Applications of Interfacial Syntheses of Nanoelectronic Materials: High-*K* Perovskite Oxides and Electroresponsive Polymeric Systems

1.1 Introduction

The Nobel Laureate and physicist educator, Richard P. Feynman foresaw the power of *Nanotechnology* in his now famous lecture ***"There's Plenty of Room at the Bottom…"***[1] on Dec. 29, 1959, at the annual meeting of the American Physical Society. In this landmark scientific lecture, he expounded on his visions in several important scientific fields, in which little had been explored at that time, but are now key scientific and technological areas. His question of ***"Why cannot we write the entire 24 volumes of the Encyclopedia Britanica on the head of a pin?"*** is now answered by the state-of-the-art technology named "Nanolithography";[2] His prediction of ***"Better electron microscopes"*** was fulfilled by the scientific finding of "Scanning Tunneling Microscope" which can visualize structures in atomic resolution (Nobel Prize in Physics, Gerd Binnig and Heinrich Rohrer, 1986)…[3] However, many profound and intriguing issues stemming from these questions are still under investigation by modern scientists. For example, Bio-mimetics and -mineralization is now a fundamental interdisciplinary topic.[4] The subject of ***"Rearranging the atoms"***,

i.e. the "bottom-up" approach, still remains as a prominent subject in Nanotechnology.[5]

Among these unsolved and unexplored fields, *Nanoelectronics* are a preeminent subject, presenting many scientific and technological challenges and offering potentials for great advancement for the next generation semiconductor industry.[6] While *Nanotechnology* generally refers to a practical technology manipulating objects less than 100nm in dimension, *Nanoelectronics* is defined as the utilization of nanotechnology on nano-devices and their elements, in which quantum phenomena play an important role. An example is the *quantum metal wires*.[7] Metal wires are classified into two distinctive types: classic wires and quantum wires. In a classical wire, the conductance behavior obeys Ohmic relationship because the length of the metal wire is much longer than the electron mean free path, and the diameter of the wire is much wider than the electron *de Broglie* wavelength. When the diameter of a metal wire is comparable to the electron wavelength, quantized conductance is observed; when the length of the metal wire is shorter than the electron mean free path, a ballistic conductance is observed. At room temperature, the electron wavelength is in angstrom level and the mean free path is a few tens of nanometers in a typical metal. Modern techniques have been applied to obtain quantum wires and the advancement of these nano-elements holds immense promise for the next generation of electronics.

In addition to electronic conductors, there are many candidates for different functions in nanoelectronics to be explored, including quantum dots, ferroelectrics, dielectrics, conjugated organic nanostructures. Although these candidates possess

promising potentials for future applications, their investigation is still in the infancy stage. From this viewpoint, the development of new methodologies for the preparation of novel nanostructures is of critical importance for Nanoelectronics. This dissertation reports findings including novel nanoscience methodologies mediated by interfaces for the preparation of ferroelectric and high-*K* dielectric mixed-metal oxides, electroactive polymers and their composites in nanometer scale. In addition, novel ferroelectric, dielectric, conductance and electrorheological properties of the studied nanostructures will also be examined in this dissertation. The following sections in this chapter will introduce the subjects of perovskite oxides, organic conjugated polymers and their composites in nanometer scale.

1.2 Syntheses of Perovskite Oxides in Nanometer Scale*

1.2.1 Perovskite Oxides and Ferroelectrics

Ferroelectric materials exhibit spontaneous dipole moment; their orientations can be switched by the application of an external electrical field, i.e., the *Coercive Field*. In a typical ferroelectric perovskite oxide, a phase transition from cubic phase at a higher temperature to a tetragonal phase at a lower temperature is usually observed. This transition point is called Curie temperature, T_c. **Scheme 1.1** shows the lattice units of barium titanate, one of the most widely studied ferroelectric perovskite oxides, in both cubic (paraelectric) and tetragonal (ferroelectric) phases. The cubic phase, **Scheme 1.1 (a)**, exhibits an induced polarization, which returns to zero when the external field is removed; while the tetragonal phases retain a spontaneous

* Par of this section has been published in Ref. 21.

polarization. The two variants, **Scheme 1.1 (b, c)**, have a 180° difference in direction due to the off-center titanium ion.

Because of the distinctive physics of ferroelectric perovskite oxides, they have been attracting extensive research interests in the fields of high-*K* materials,[8] electromechanic transducers,[9] and ferroelectric random access memories (FeRAM).[10]

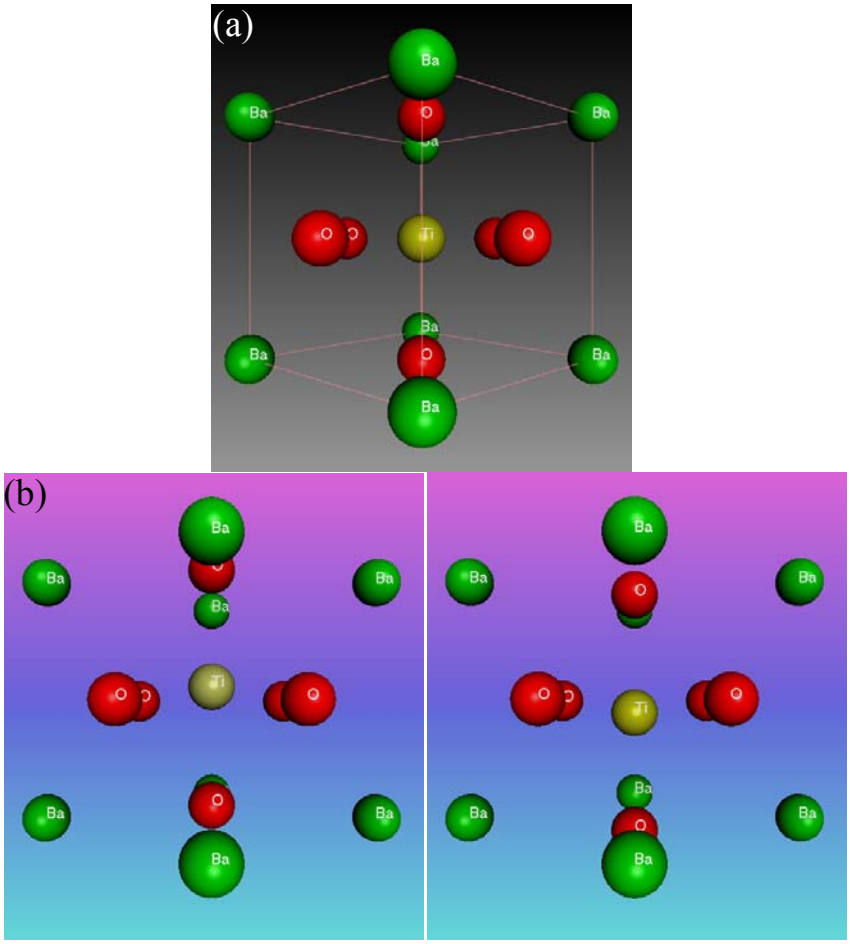

Scheme 1.1 Lattice units of barium titanate in both cubic, paraelectric **(a)**, and tetragonal, ferroelectric **(b, c),** phases. The two polarization variants, **(b)** and **(c)** have 180° difference in polarization direction due to the off-center of the Ti^{4+}. **(b)** is polarization down and **(c),** polarization up.

1.2.2 Barium Titanate, Strontium Titanate and Their Solid Solutions in Nanometer Scale

Barium titanate ($BaTiO_3$, BTO) and strontium titanate ($SrTiO_3$, STO) are among the most widely studied ferroelectric perovskite oxides. The T_c of BTO is ~400 K; and ~105K for STO. Thus, at room temperature, BTO is ferroelectric and STO is paraelectric. Barium-strontium titanate ($Ba_xSr_{1-x}TiO_3$, BST) refers to a series of solid solutions of BTO and STO. The ferroelectric properties of BSTs can be optimized by adjusting the molar ratio, x. With the current rapid advances in nanoscience, BTO, STO and BST crystals in nanometer scale with high quality and low defect are highly desirable systems for fundamental as well as technological investigations.

Although the ferroelectric polymorph of BTO is thermodynamically stable at room temperature, most of the previous synthetic procedures for the preparation of BTO crystals included high temperature (~1000^{o}C) sintering followed by annealing. Recently, extensive efforts have been focused on the establishment of moderate reaction conditions, especially lowering the synthetic temperature, for high-quality nanocrystals. Reaction conditions involved for the synthetic processes and the quality of the resulting nanocrystals are of prime concerns. Temperatures involved in the synthetic procedures significantly influence the attributes of the resulting crystals, including the concerns for aggregation and thermal stress. O'Brien, Brus and Murray reported their synthesis of monodisperse nanoparticles of barium titanate,[11] which was adopted by Park, *et al.*, for the synthesis of single-crystalline perovskite nanorods, later proved to be of tetragonal polymorph.[12-14] This progress is important to the synthesis of perovskite oxides; however the reaction conditions reported were

demanding, including requiring final sintering at 700°C to obtain high-purity nanocrystals. Wong and coworkers reported a synthesis of single-crystalline perovskite nanostructures,[15-17] which involved an 820°C annealing process, yielding BTO in cubic rather than tetragonal form. In 2004, two research papers were published by the same group.[18] Nanocrystals of BTO, STO and BST with a single composition, $Ba_{0.5}Sr_{0.5}TiO_3$, were synthesized at 200°C under conditions involving inert environment and high pressure. The BTO products were confirmed to be cubic rather than tetragonal polymorph later.[19] In 2006, Wang and coworkers reported their new synthesis of complex functional-oxide, including BTO and $Ba_{0.5}Sr_{0.5}TiO_3$ by a composite-hydroxide-mediated approach at 165°C.[20] Special reaction vessel and stringent conditions were applied to obtain single-crystalline nanoparticles. From 2001 to 2006, a tendency to lower the synthetic temperature is clearly noticed. In our group, two low-temperature approaches have been developed for the syntheses of BTO, STO and BST in nanometer scale. The "Room Temperature Synthesis of Ferroelectric Barium Titanate Nanoparticles Using Peptide Nano-rings as Templates"[21] contributes to the start of a new trend for searching low-temperature approaches. Two bio-inspired room-temperature approaches were also published after the report of our finding.[22, 23] These three reports showed that tetragonal BTO can be obtained at synthetic temperatures lower than the Curie temperature (120°C) of BTO. Thus the importance of the direct formation, without annealing, of the tetragonal polymorph at synthetic temperatures below 120°C has been established. A detailed discussion in details will be presented in Chapter 2 of the dissertation.

Our second approach is focused on a large scale synthesis of BTO, STO and BST nanocrystals at 80°C. By using reverse micelles, a facile open-bench synthetic method which yields high quality BTO, STO and BST nanocrystals with various compositions was developed. The establishment of a direct path to $Ba_{0.7}Sr_{0.3}TiO_3$ (50 to 10 nm) nanocrystals with giant dielectric constant (in 10^5) represents a significant scientific and technological finding. This approach will be addressed in details in Chapter 3.

1.3 Fabrication of Single-crystalline Conducting Polymer Nanostructures by Interfacial Polymerization-Crystallization†

1.3.1 Introduction

Compared with metallic and metal oxide nanostructures, much less work has been done for conducting polymers in nanometer scale. The importance of conducting polymers has been recognized by the award of a Nobel Prize in 2000 to Hideki Shirakawa, Alan MacDiarmid and Alan Heeger.[24-28] Although the first *metallic* polyacetylene has been discovered by the laureates in 1977, early contributions[29-34] in polyene synthesis dawned the era of conducting polymers. Polyaniline (PANI), polypyrrole (PPY) and polythiophene (PT) are among the most widely studied conducting polymers because of the facile polymerization of their monomers either chemically or electrochemically. However, their insoluble and infusible nature hampered the fabrication of well-defined conducting polymer nanostructures.

† Part of this section has been published in Ref. 39.

Although the conductance behavior of conducting polymers, either in classical or in quantum mechanical electronics, follows the fundamental physics, their organic nature made them distinct from metals and metal oxides. For example, He and coworkers observed a quantized conductance switch behavior in a PANI nanowire with a length of around 1nm. This phenomenon is comparable to the ballistic conductance case observed in a *quantum metal wire* with a length smaller than the electron mean free path.[35] Although no structural evidence has been revealed in this research, the observation of quantized conductance switch was extremely interesting for both scientific and technical studies. To investigate the nature of the conductance behavior of conducting polymers in nanometer regime, well-defined structures must be fabricated.

1.3.2 Interfacial Polymerization-Crystallization

In recent years, the efforts in the fabrication of conducting polymer nanostructures include electrochemical epitaxial polymerization,[36] solution spin-coating on a functionalized surface,[37] and solid-state polymerization of monomer crystals.[38] However, single crystalline conducting polymers in nanometer scale have not been reported prior to our findings.[39] An Interfacial Polymerization-Crystallization consists of polymerization of conjugated monomers via oxidative coupling mediated by the interface of two immiscible liquids. Low concentrations of both the monomer in oil phase and the oxidizer in aqueous phase are employed to allow the process of crystallization during polymerization. This technique was first established in the syntheses of poly(3,4-ethylenedioxythiophene) (PEDOT) and poly(3-hexyl thiophene) (P3HT) nanoneedles (**Scheme 1.2**).[39] These conducting

polymer nanoneedles possess special structural and electronic properties, including single crystalline nature, fast conductance switching behavior and self-assembly to uniform sheets. Chapter 4 will address the fabrication and property studies of these polythiophene nanostructures.

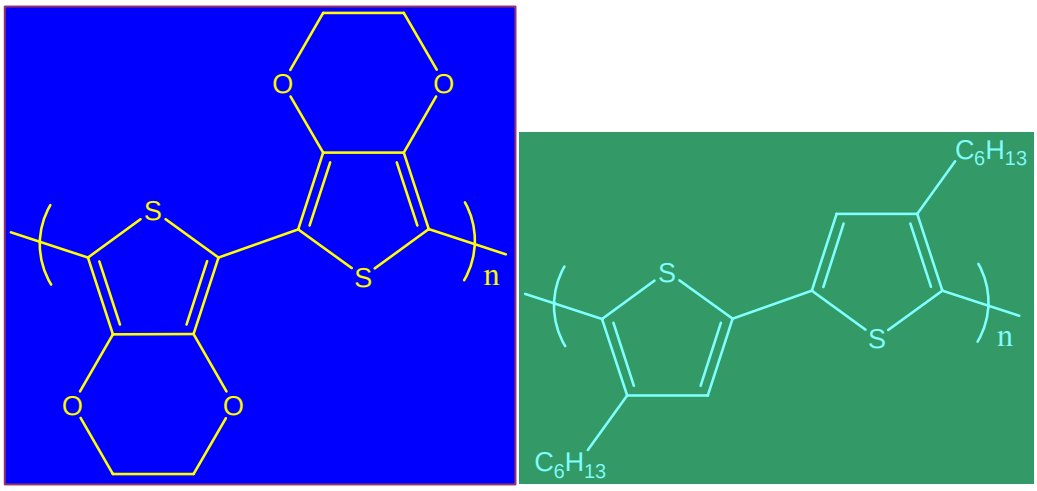

Scheme 1.2 Chemical structures of poly(3,4-ethylenedioxythiophene) (PEDOT) and poly(3-hexyl thiophene) (P3HT) in undoped form.

With further lowering of the concentration of the oxidizer solution, this technique is also effective for the production of nanoneedle structures of polypyrrole (PPY) and polyaniline (PANI) (Chapter 4).

1.4 One-pot Synthesis of Strontium Titanate/Polyaniline Nano-Composites and Their Electrorheological Effect

The importance of perovskite ferroelectric oxides and conducting polymer nanostructures has been introduced in previous sections. A novel structured strontium titanate/polyaniline (STO/PANI) nano-composite is now introduced in this section. STO is an n-type semiconductor, while PANI, a p-type.[40] Their nano-composites with

novel structures exhibit interesting properties due to the interaction between the two components. The nano-composites were prepared in a *One-pot* manner as a second step in the same reverse micelle system after the synthesis of STO. An embedded core-shell nanostructure was produced with an insulating organic shell and a conducting inorganic/organic hybrid core. **Scheme 1.3** gives the schematic structure of the stuffed sphere morphology of the nano-composite with STO nanocrystals[41] in PANI matrix (dark gray) depicting the embedded structure of the STO/PANI nano-composite as shown in the TEM morphology (to be discussed in Chapter 5). This novel structure combines atomic and electronic polarizations in one element in nanometer scale and exhibits synergistic electronic properties.

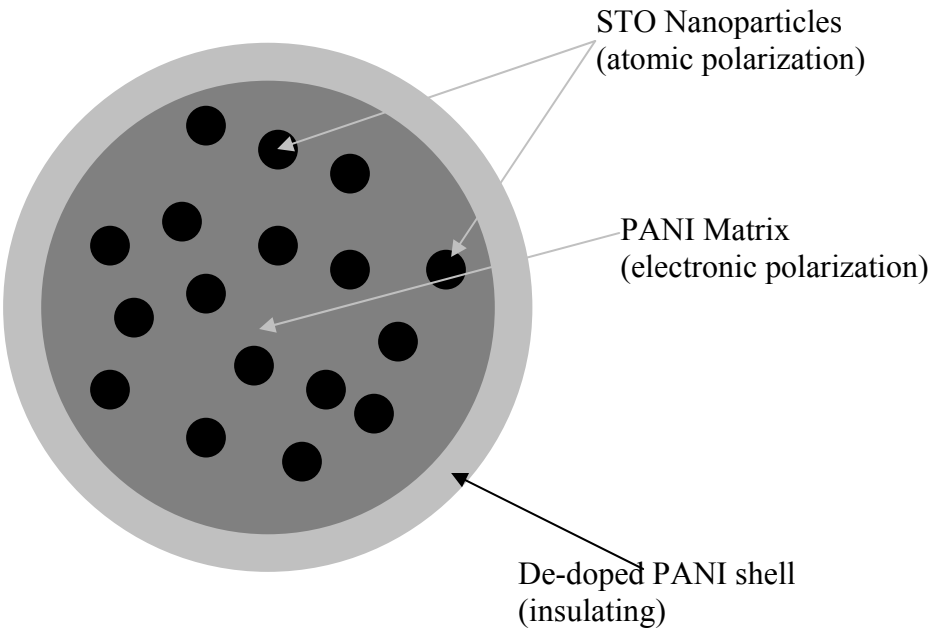

Scheme 1.3 Schematic structure of the nano-composite in one micelle.

One of the applications of these novel nanostructures is in electrorheological fluids (ERF). An ER fluid is a kind of smart material with its rheological properties

undergoing reversible changes drastically with changes of an external electric field.[42-45] Generally, an ER fluid is a suspension system consisting of fine, solid particles (ER materials) suspended in an insulating liquid medium. Although some applications have been developed, the key factor for making an effective ERF is the choice or synthesis of a preferred ER material; many materials with excellent properties have been employed. The STO/PANI nano-composites as a new ER material showed a synergistic effect and stable ER behavior. This part of the research will be discussed in Chapter 5.

Chapter 2

Fabrication of Ferroelectric Barium Titanate Nanocrystals at Room Temperature Using Peptide Nano-rings as Templates[1]

2.1 Introduction

Perovskite oxides, barium titanate, strontium titanate and their solid solutions, are of critical importance for both fundamental and technical studies in the subject of high-*K* materials. Extensive efforts have been made to develop efficient methods for the synthesis of high-quality ferroelectric perovskite nanocrystals (Chapter 1, Section 1.2). These developments were primarily based on early works in late 1940's and early 1950's. The landmark reports include a treatise in 1946 by von Hippel and coworkers illustrating the origin of a remarkable dielectric behavior and higher values of polarization than those of titanium dioxide observed in bulk titanates.[2] The then "new" mechanism, *"In the ionic crystal lattices dipole moments are created by the displacing of ions from their equilibrium positions"*, is now widely accepted as the origin of the high values of dielectric constant. In 1951, Matthias discussed, in his review paper, the relationship between the ferroelectricity and the phase transitions in perovskite type titanates.[3] In barium titanate, for example, a paraelectric cubic structure form is stable above its Curie temperature, 120^{o}C, whereas a tetragonal ferroelectric structure form takes over at the temperature range of 0 to 120^{o}C. The

tetragonal polymorph is decisively important for the spontaneous polarization by a distortion of titanium ions from the centrosymmetric to an asymmetric position within the TiO_6 octahedra.[4-8] Although a wide variety of synthetic methods have been reported for titanates,[1, 5, 7, 9-58] there are two crucial issues with regard to the development of their fabrication: (1) the size effect of titanates in the nanometer scale; and (2) synthesis conditions, especially the synthetic temperature.

The first crucial issue is the size effect of titanates in nanometer regime. High-quality titanate nanocrystals are required for the next generation of electronics and semiconducting industry. Paraelectric cubic barium titanate crystal lattice belongs to the centrosymmetric *Pm3m* space group, whereas ferroelectric tetragonal one belongs to the non-centrosymmetric *P4mm* space group (lattice units $c>a$: c = 4.036 Å; a = 3.992 Å).[27] The ratio of "*c/a*" is defined as "*Tetragonality*". For bulk ferroelectric barium titanate crystals, the tetragonality is usually measured by techniques including X-ray diffraction (XRD), neutron powder diffraction or Raman spectroscopy.[59-61] For example, in XRD, the peaks for lattice indices 200 and 002 are usually distinct with observable splitting. With decrease in the particle size, a diminishing of ferroelectricity or tetragonality has been observed in previously synthesized barium titanate nanoparticles. As shown in **Figure 2.1**, the critical size for the disappearance of ferroelectricity was around 30nm. The origin for the size effect is still not established, although two main reasons were suggested: 1) it is intrinsic nature of the nanoparticles smaller than the critical size; 2) the impurity surface ions form a local depolarization field preventing the formation of the tetragonal phase. Recently, we observed the ferroelectric tetragonal phase in barium titanate nanocrystals with

particle size as small as 6nm.[1] This finding provided the evidence that the diminishing of ferroelectricity in previous reported studies may not be inherent to the system. Special techniques, including ultraviolet Raman spectroscopy[60] and the atomic pair distribution function (PDF) technique,[61] have been developed; they could be very useful as methods to further substantiate the ferroelectricity observed in our barium titanate nanocrystals.

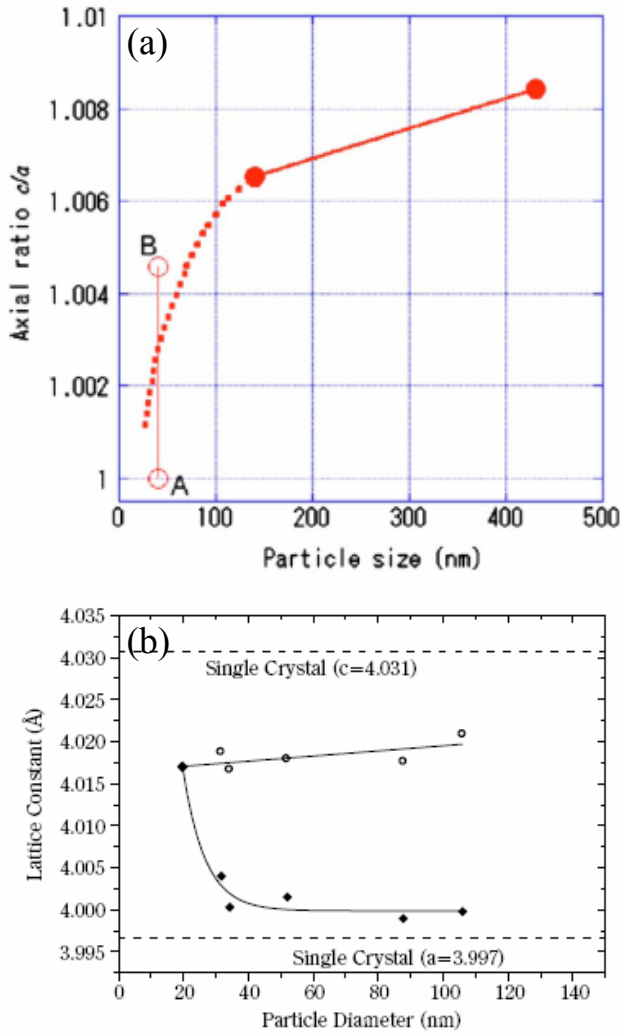

Figure 2.1 Size effects in barium titanate nanoparticles.[62, 63] Reproduced from **(a)** M. Yashima, *et al*, *J. Appl. Phys.,* 98, 014313-8 (2005); and **(b)** T. Ohno, *et al, Kona,* 22, 195-201 (2004).

Additional important issues include the synthetic temperature. Lower synthetic temperature is preferred and the final titanate product should be in tetragonal polymorph. For barium titanate, the tetragonal polymorph is thermodynamically stable at room temperature. However, the synthetic approaches at low temperature usually result in the formation of the cubic polymorph. A sintering process, at around 1000^{o}C, followed by annealing through the Curie temperature, was requisite for obtaining the tetragonal polymorph. The high-temperature sintering process not only is energy-consuming but results in agglomerations, which deteriorate the size distribution of the final products. For crystals in nanometer scale, the agglomeration is a more serious concern with regard to the particle distribution and size level. Previously, various synthetic methods have been developed, including co-precipitation,[29, 41] sintering of coordinate precursors,[35] hydrothermal and solvothermal methods,[11, 14, 24, 38, 43, 44] sol-gel process,[16, 27] liquid-solid-solution (LSS) phase transfer,[52] seed-mediated growth in aqueous system,[64] and procedures mediated by molten composite-hydroxide.[55] In co-precipitation, sintering of coordinate precursors and sol-gel processes using titanium alkoxides and barium salts, organic capping reagents were usually employed to coordinate the metal ion or stabilize the particles from agglomeration. Hydrothermal and solvothermal methods involved high-pressure approaches by using titanium alkoxide or oxide gels as the precursor and barium salt or hydroxide as the barium source.[27] The procedures mediated by molten composite-hydroxide avoided the use of organic capping reagents and were based on a reaction between a metallic salt and a metallic oxide in a solution of molten mixed potassium hydroxide and sodium hydroxide eutectic at ~200 ^{o}C.[55]

In addition to the efforts of synthesizing titanates by using traditional chemical methods, biomimetic methods provided an environmentally benign alternative.[1, 57, 58] In 2006, we reported our "Room Temperature Synthesis of Ferroelectric Barium Titanate Nanoparticles Using Peptide Nano-rings as Templates". Later in that year, a vapor-diffusion sol-gel route,[58] and a fungus-mediated approach[57] were also reported as room-temperature syntheses of barium titanate under biomimetic or bioinspired conditions.

2.2 Experimentals

2.2.1 Synthesis of Bolaamphiphilic Peptides[74]

The scheme of the synthesis of bolaamphiphilic peptides followed previous peptide synthetic approaches.[65-75] Bolaamphiphiles refer to a series of amphiphilic species with an alkyl chain at the middle of the compound and two hydrophilic end groups (**Scheme 2.1**).

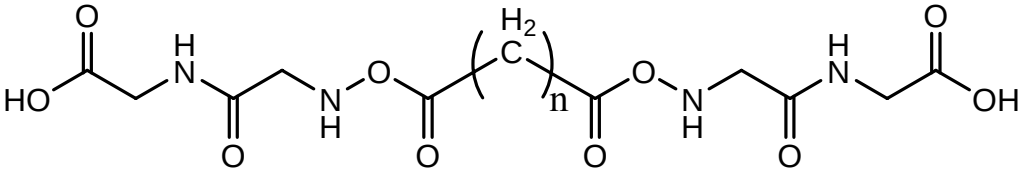

Glycylglycine bolaamphiphiles

Scheme 2.1 Chemical structure of the bolaamphiphilic peptide.

By using Bis(*N*-alpha-amido-glycylglycine)heptane-1,7-dicarboxylate as a example, the synthetic route is shown in **Scheme 2.2**. Typically, in N, N-dimethylformamide (DMF) were dissolved the dicarboxylic acid and 1-hydroxybenzotriazole (HOBt). To this solution, a chloroform solution containing N-

Ethyl-N′-(3-dimethylaminopropyl)carbodiimide hydrochloride (EDAC) was added at -5^{o}C with stirring and the mixture was stirred for 1 hour at that temperature. To the resulting solution, a methanol solution containing glycylglycine benzyl ester hydrochloride, and then triethylamine were successively added. The mixture was stirred for 24 hours while gradually increasing the temperature to room temperature. The solvent was then removed in vacuo to obtain a white precipitate. The precipitate was washed on a filter paper successively with a 10%wt aqueous citric acid solution, water, a 4%wt aqueous sodium hydrogen carbonate solution and water and then crystallized from DMF to obtain N, N'-bis(glycylglycine benzyl ester)heptane-1,7-dicarboxyamide. This dicarboxyamide was dissolved in DMF in a water bath at 50^{o}C, to which a 0.1N NaOH solution was added. The precipitate was recrystallized from DMF to obtain Bis(*N*-alpha-amido-glycylglycine)heptane-1,7-dicarboxylate (C7) as a white solid.

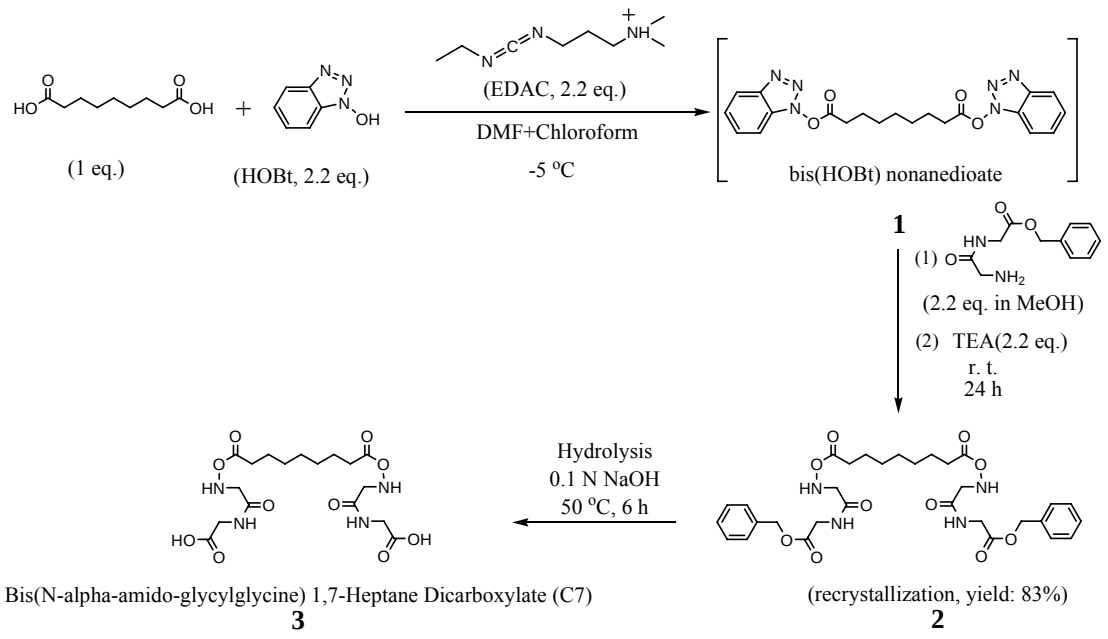

Scheme 2.2 Synthesis of Bis(*N*-alpha-amido-glycylglycine)heptane-1,7-dicarboxylate.[74]

2.2.2 Nano-ring Self-assembly by C7 and A Bimetallic Precursor

Bis(*N*-alpha-amido-glycylglycine)heptane-1,7-dicarboxylate, C7, and bimetallic precursor, barium titanium ethyl hexano-isopropoxide, $BaTi(O_2CC_7H_{15})[OCH(CH_3)_2]_5$, were used as monomers to self-assemble nano-rings. In the peptide monomer solutions (10mL) at different pH values by using citric acid/NaOH (10mM) as the buffer solutions were added 20μL of $BaTi(O_2CC_7H_{15})[OCH(CH_3)_2]_5$ (13%wt in isopropyl alcohol, Alfa Aesar). Ring-shaped self-assemblies appeared after 1–4 days in the dark. This solution containing the nano-ring-$BaTiO_3$ complexes was washed with deionized water and centrifuged at 14.5k rpm. After this process was repeated twice, the solution was then irradiated by long-wave UV light (355 nm) for 10 hours to remove the peptide templates. The final

product was then washed and centrifuged to purify the tetragonal $BaTiO_3$ nanocrystals.

2.2.3 Morphological and Structural Studies of The Nano-ring Self-assembly and The Final Barium Titanate Nanocrystals

The nano-rings and the extracted $BaTiO_3$ nanoparticles were imaged by AFM (Nanoscope III, Vecco, Inc.) on freshly cleaved mica surfaces. These samples were also dried on carbon-coated copper grids at room temperature and studied by TEM and electron diffraction (JOEL 1200 EX) at an acceleration voltage of 100 kV. X-ray diffraction was measured using a Philips PW3040. A confocal Raman microscope (LabRam, Jobin Yvon/Horiba) was used to obtain Raman spectra and two-dimensional Raman images. The 632.8nm line of an air-cooled He/Ne laser was injected into an integrated Olympus BX 40 microscope and focused to a spot size of approximately 0.7μm by an 80× long-working-distance objective.

2.2.4 Ferroelectric Polarization Study by Electrostatic Force Microscope (EFM)

EFM images of the $BaTiO_3$ nanoparticles were recorded by the same atomic force microscope with a NanoScope Extender (Vecco, Inc) on Au substrates.

2.3 Results and Discussions

Our novel method by using ring-shaped peptide assemblies as templates for the one-step biomimetic synthesis of ferroelectric $BaTiO_3$ nanoparticles in a tetragonal structure at room temperature represents a great contribution to both ferroelectric

oxide synthesis and biomineralization.[1, 57, 58] Biological and biomimetic systems produce remarkable structures of crystals controlled by the chemical structure, the morphology, and the shape of the biological templates. For example, sea urchin larvae grow single-crystalline calcite in a curved compartment,[72] and our approach mimics those systems by growing the unusual structures of the $BaTiO_3$ crystals on curved and confined peptide assemblies. To the best of our knowledge, this is the first report on the growth of ferroelectric $BaTiO_3$ nanoparticles at room temperature.

Peptide templates are used to hydrolyze $BaTi(O_2CC_7H_{15})[OCH(CH_3)_2]_5$ inside the cavities in order to produce the tetragonal $BaTiO_3$ nanoparticles at room temperature. Previously, it has been found that ring-shaped peptide assemblies could template Au-nanoparticle formation inside the peptide rings.[76, 77] While the size of the Au nanoparticles can be controlled by the cavity size, they grow with or without the peptide nano-rings. However, the new discovery reported here is that the peptide nano-rings have the biomimetic function of crystallizing nanometer-scale crystals that have never been grown under ambient conditions. In other words, tetragonal $BaTiO_3$ nanoparticles can only grow in the peptide nano-rings at room temperature. When the peptide monomer solutions are added to a precursor, $BaTi(O_2CC_7H_{15})[OCH(CH_3)_2]_5$,[27] ring-shaped self-assemblies appear after several days in the dark. During this process, the peptide nano-ring templates are self-assembled simultaneously as the precursors are hydrolyzed in the cavities (**Figure 2.2**). The peptide nano-ring structure has previously been investigated.[76]

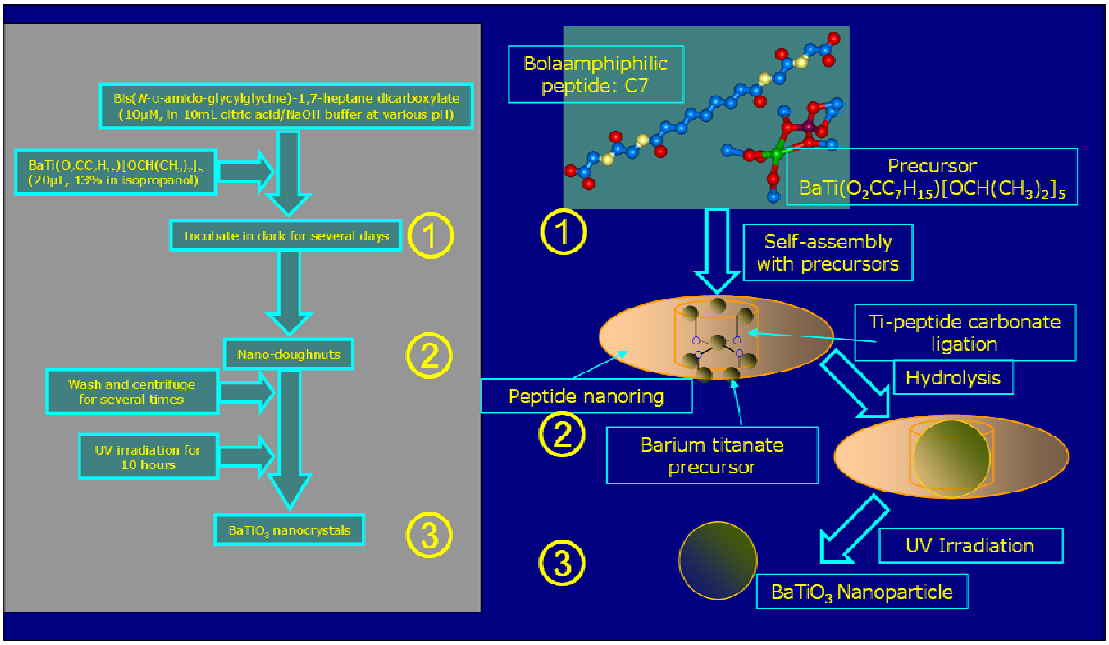

Figure 2.2 Schematic fabrication of $BaTiO_3$ nanoparticle by bolaamphiphilic peptide C7 and bimetallic precursor.

Figure 2.3 shows the topological and phase images of $BaTiO_3$ nanoparticles inside the peptide nano-rings in a pH 4.4 solution determined by atomic force microscopy (AFM). In this AFM phase image (**Figure 2.3 (b)**), the harder barium titanate nanoparticles appear in a brighter contrast at the centers of the peptide nano-rings, which appear as softer assemblies in a darker contrast. The peptide nano-rings are monodisperse with a size of 49 ± 11 nm, as determined by AFM and transmission electron microscopy (TEM). This phase contrast is consistent with that of Au nanocrystals grown inside the peptide nano-rings imaged previously.[76] A comparison of AFM and TEM was shown in **Figure 2.4**.

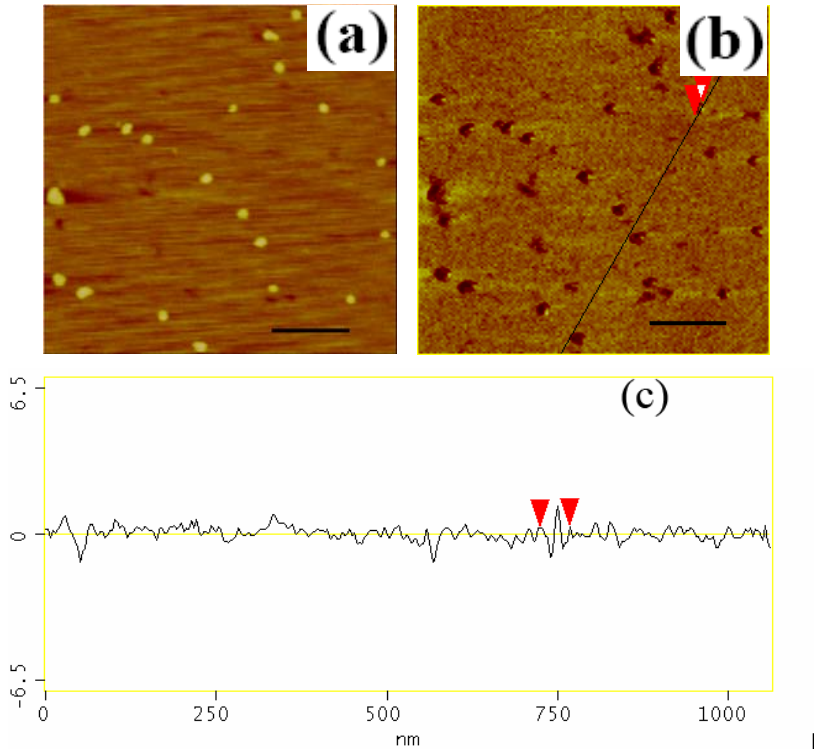

Figure 2.3 AFM topographic **(a)**, phase **(b)** images and **(c)** the section analysis of the nano-doughnuts. Scale bar=200nm.

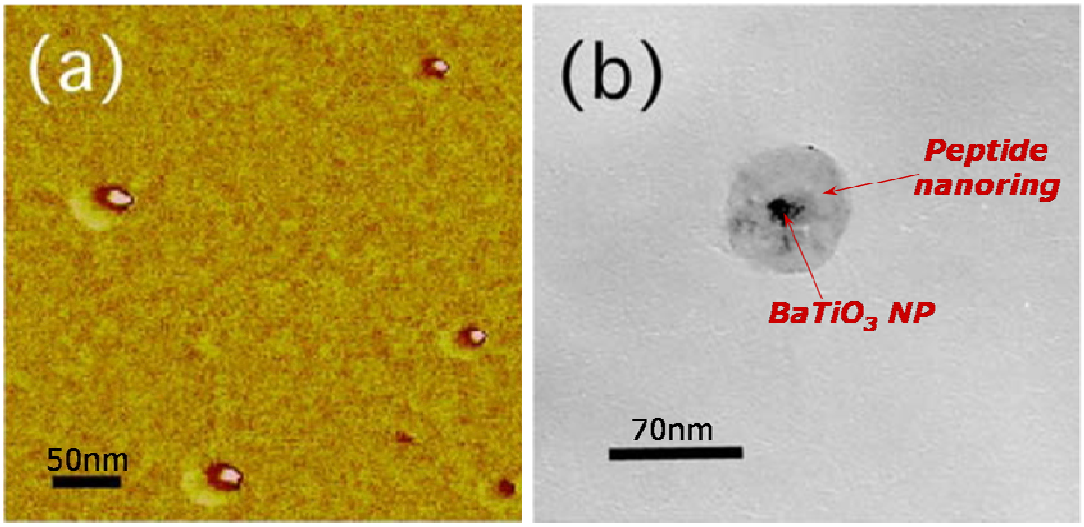

Figure 2.4 (a) Atomic force microscopy (AFM) phase image of barium titanate nanoparticles inside peptide nano-ring templates. Scale bar = 50 nm. **(b)** TEM image of a barium titanate nanoparticle inside the peptide nano-ring template. Scale bar 70 nm.

After the removal of the peptide from the nano-doughnuts assembly with UV irradiation for 10 hours, released barium titanate nanocrystals were observed as shown in **Figure 2.5**. The topological AFM images show monodisperse $BaTiO_3$ nanocrystals in the diameter of 12 ± 2 nm. To study the influences of solution pH value on the particle size and distribution of both nano-rings assemblies and final nanoparticles, AFM were employed and the morphological images and particle size histograms at different pH values are shown in **Figure 2.6**. It was observed that both the size of the nano-rings assemblies and that of the final nanopartilces have a tendency to decrease with the increase of pH value from 4.4 to 10. The diameter of the nano-rings assembly is 49 ± 11nm at pH=4.4 (**Figure2.6 (a)**); 42 ± 10nm at pH=6.0 (**Figure2.6 (c)**); 33 ± 9nm at pH=8.0 (**Figure2.6 (e)**); and 23 ± 3nm at pH=10 (**Figure2.6 (g)**), whereas the diameter of the final nanoparticles is 12 ± 2nm at pH=4.4 (**Figure2.6 (b)**); 9.5 ± 1.5nm at pH=6.0 (**Figure2.6 (d)**); 8.0 ± 1.5nm at pH=8.0 (**Figure2.6 (f)**); and 6.0 ± 1nm at pH=10 (**Figure2.6 (h)**). The sample at pH=12 showed no observable nano-rings assemblies and the final particle size was too small to be detected by AFM.

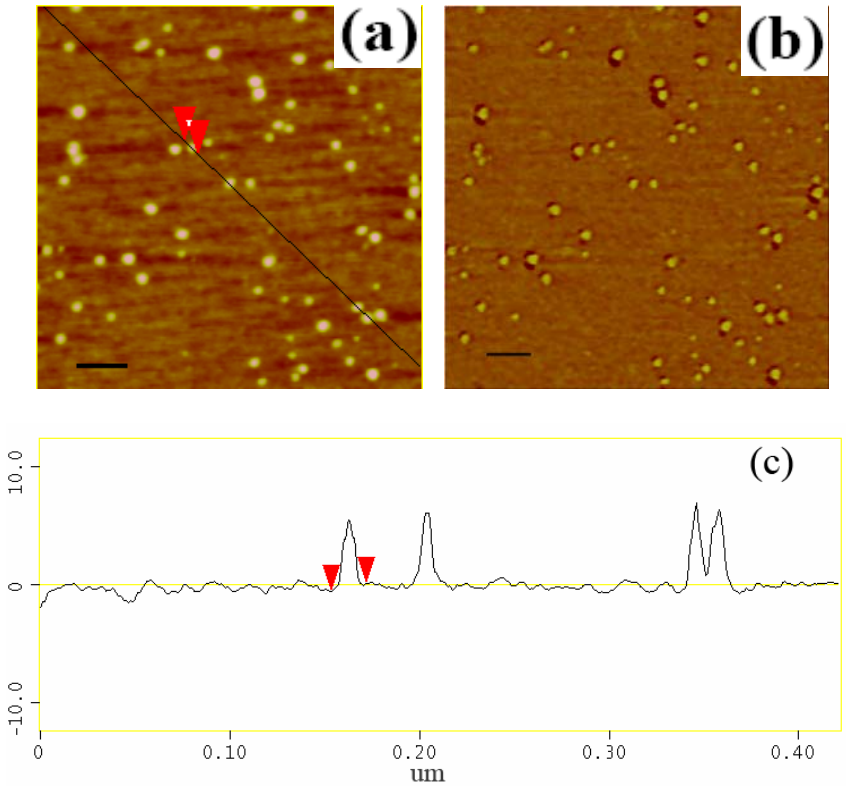

Figure 2.5 AFM images of released barium titanate nanocrystals in **(a)** height mode **(b)** phase mode **(c)** section analysis.

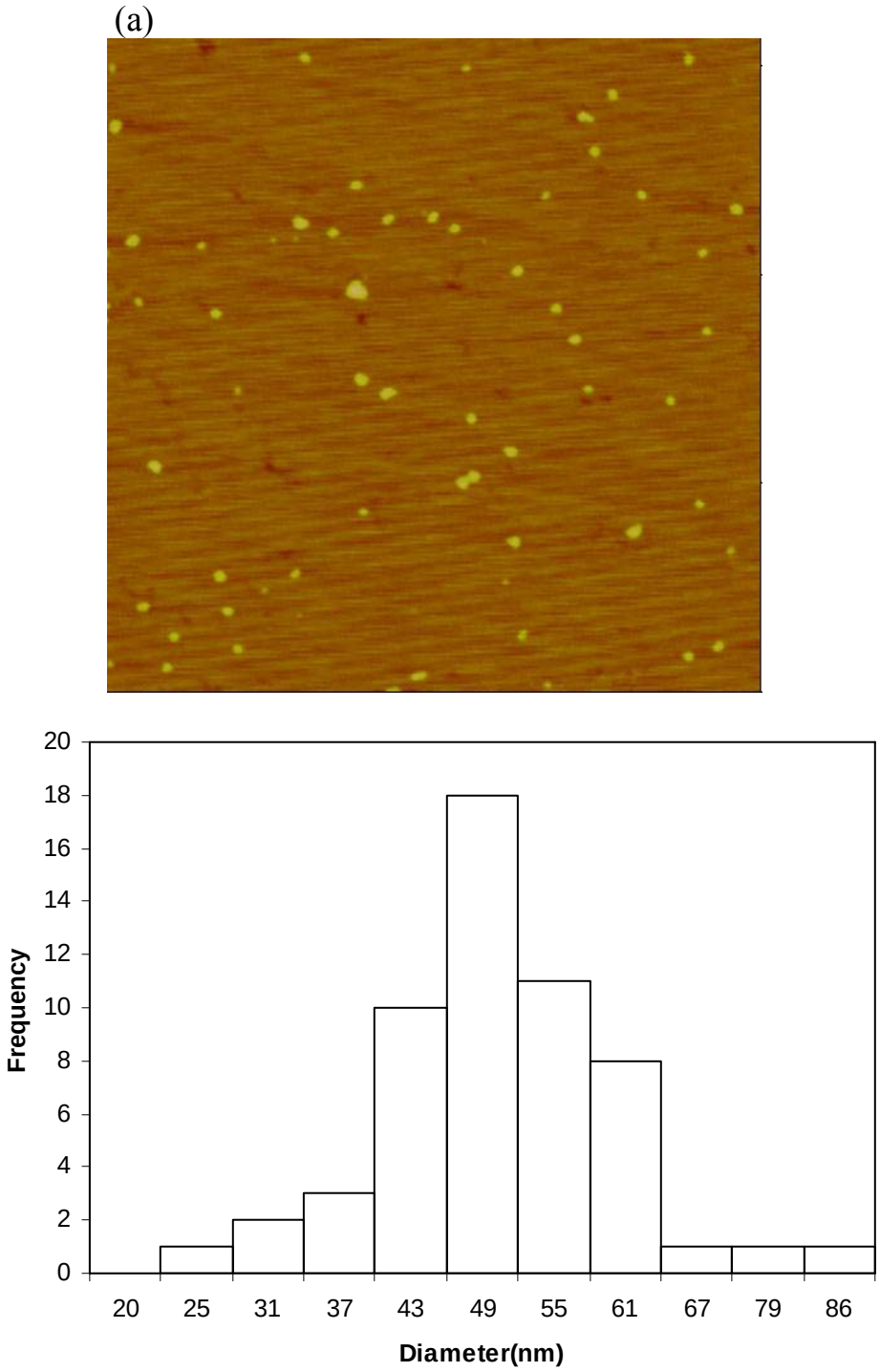

Figure 2.6 (a) AFM height image (up) and histogram of the diameter (down) of the nano-rings assemblies at pH=4.4.

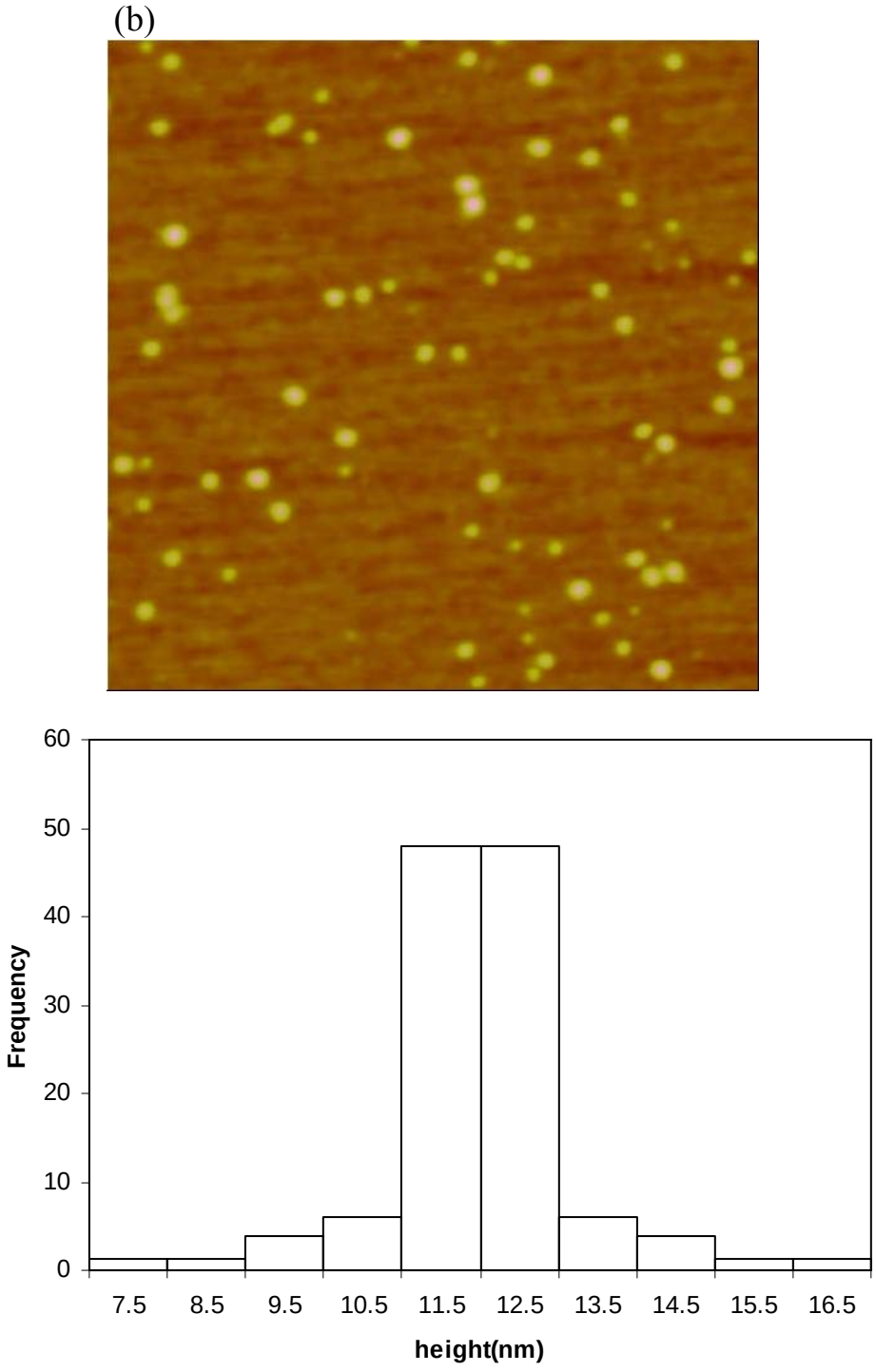

Figure 2.6 (b) AFM height image (up) and histogram of the diameter (down) of the final nanoparticles at pH=4.4.

(c)

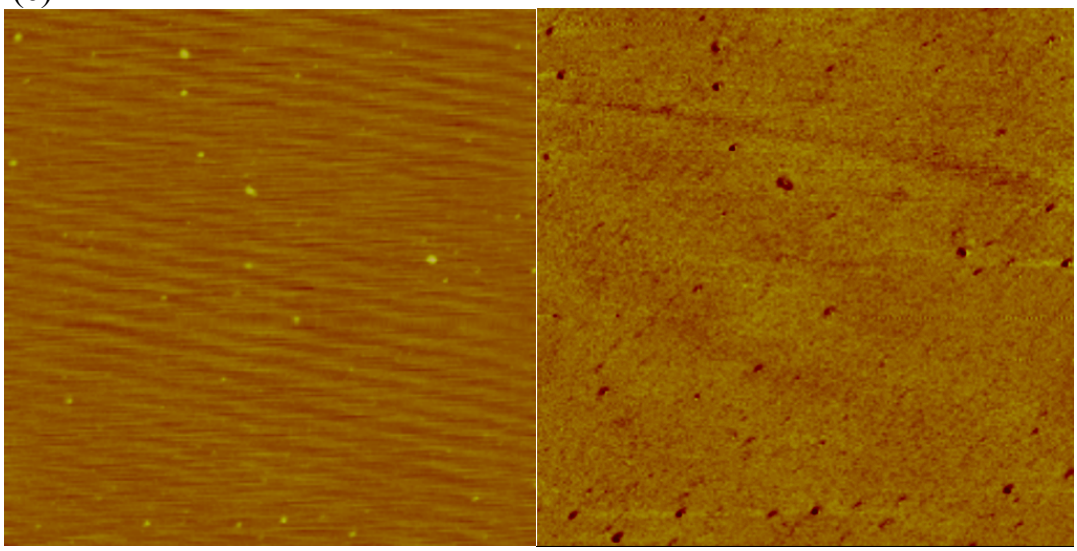

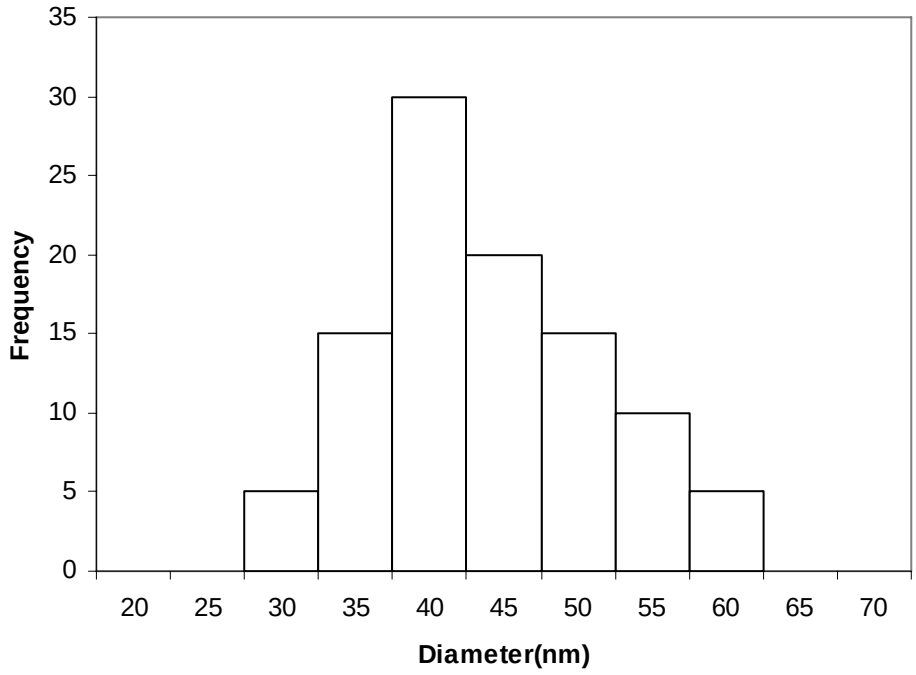

Figure 2.6 (c) AFM height image (upper left), phase image (upper right) and histogram of the diameter (down) of the nano-rings assemblies at pH=6.0.

(d)

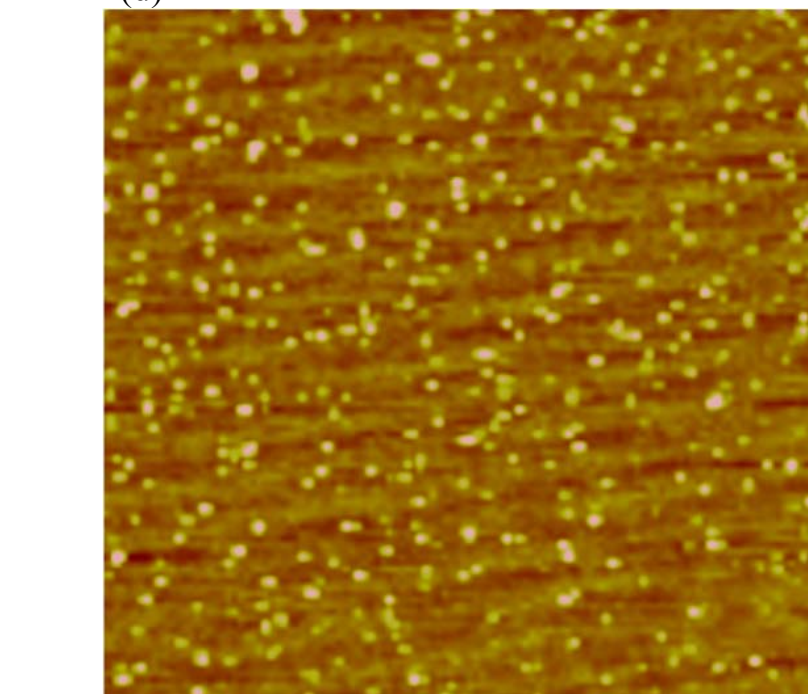

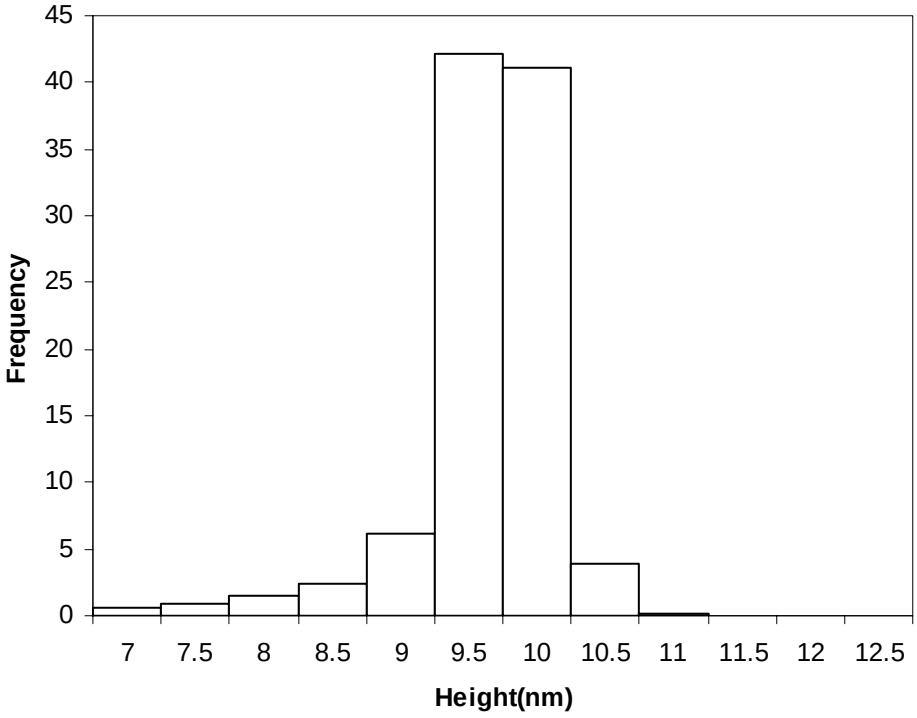

Figure 2.6 (d) AFM height image (up) and histogram of the diameter (down) of the final nanoparticles at pH=6.0.

(e)

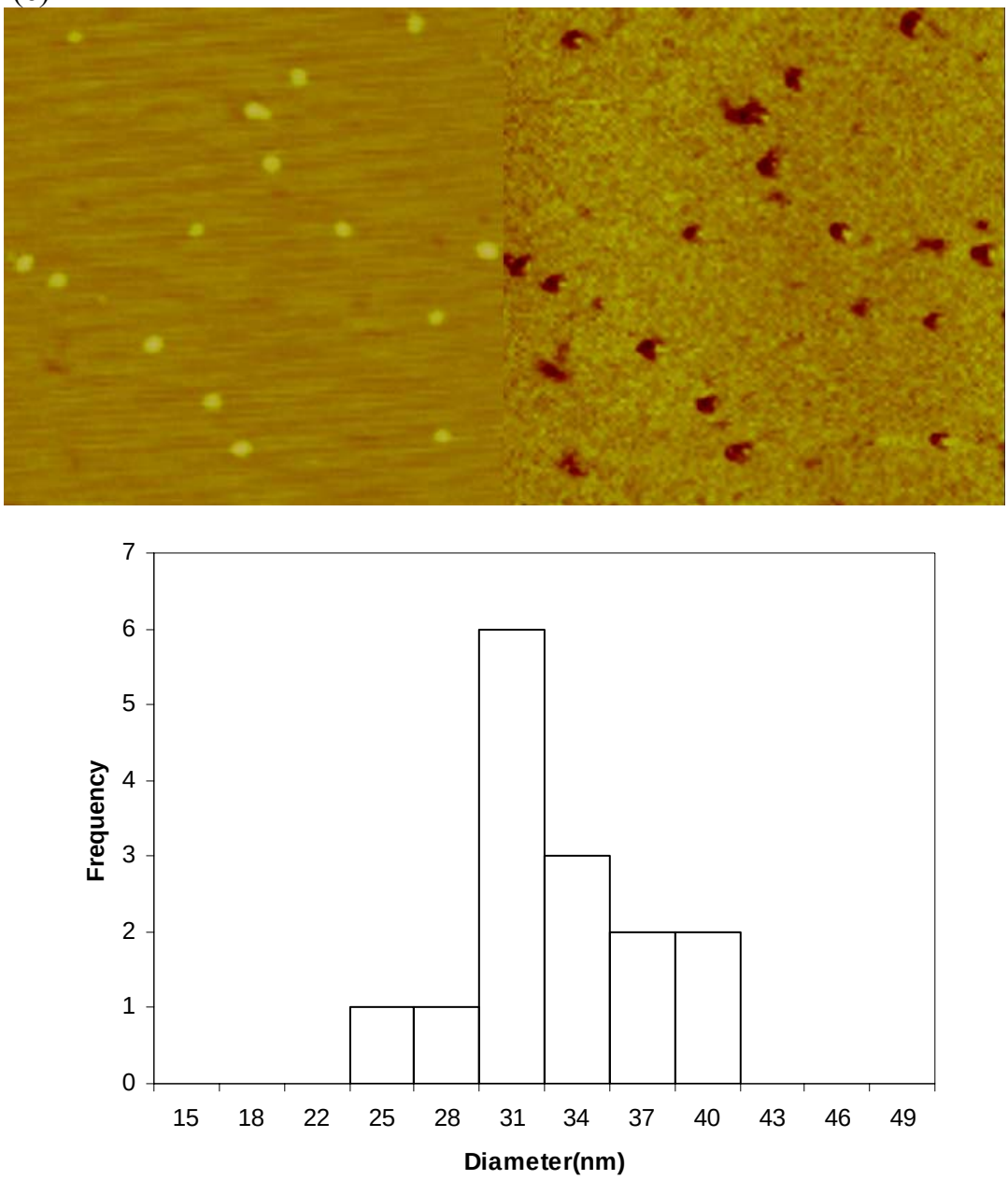

Figure 2.6 (e) AFM height image (upper left), phase image (upper right) and histogram of the diameter (down) of the nano-rings assemblies at pH=8.0.

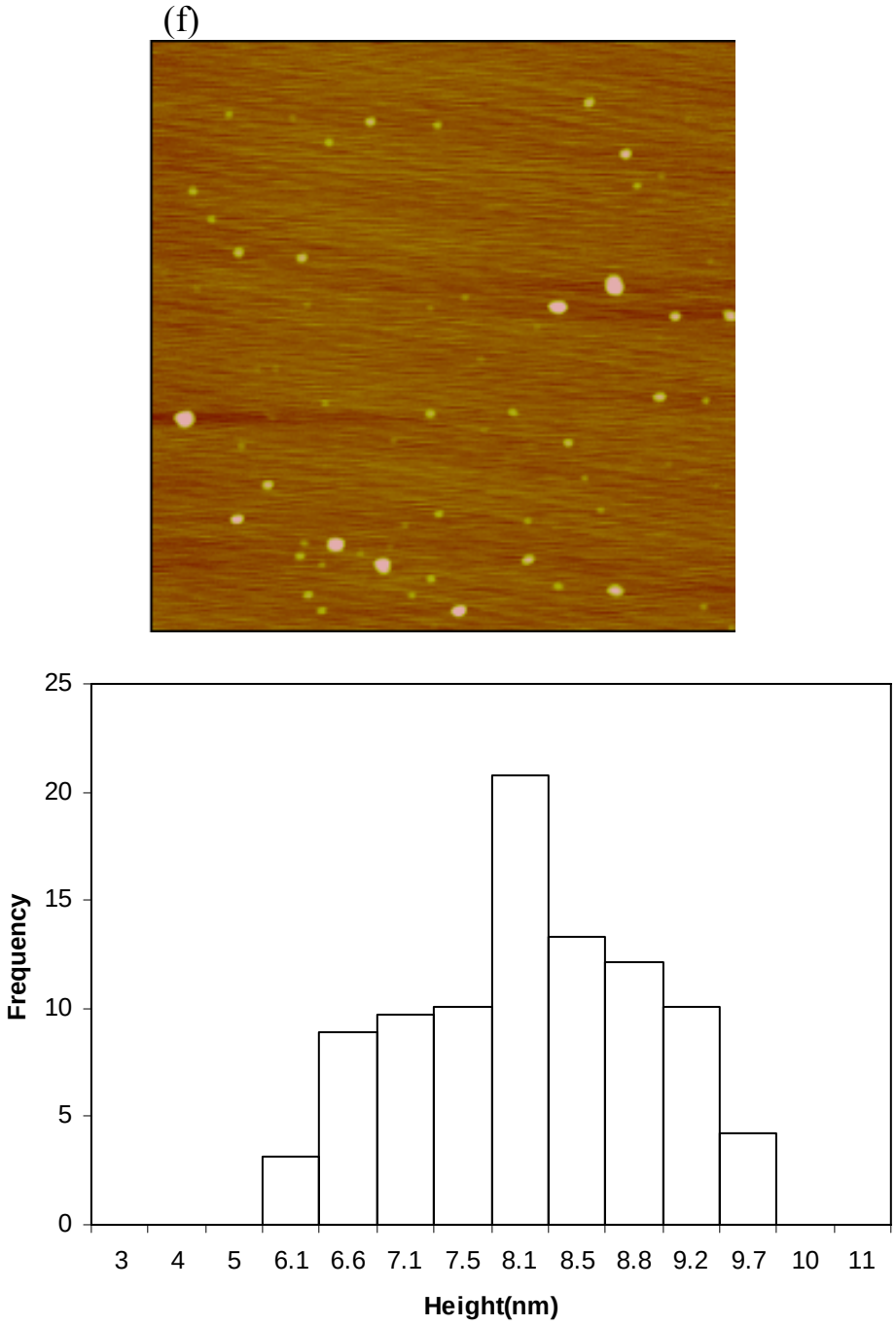

Figure 2.6 (f) AFM height image (up) and histogram of the diameter (down) of the final nanoparticles at pH=8.0.

(g)

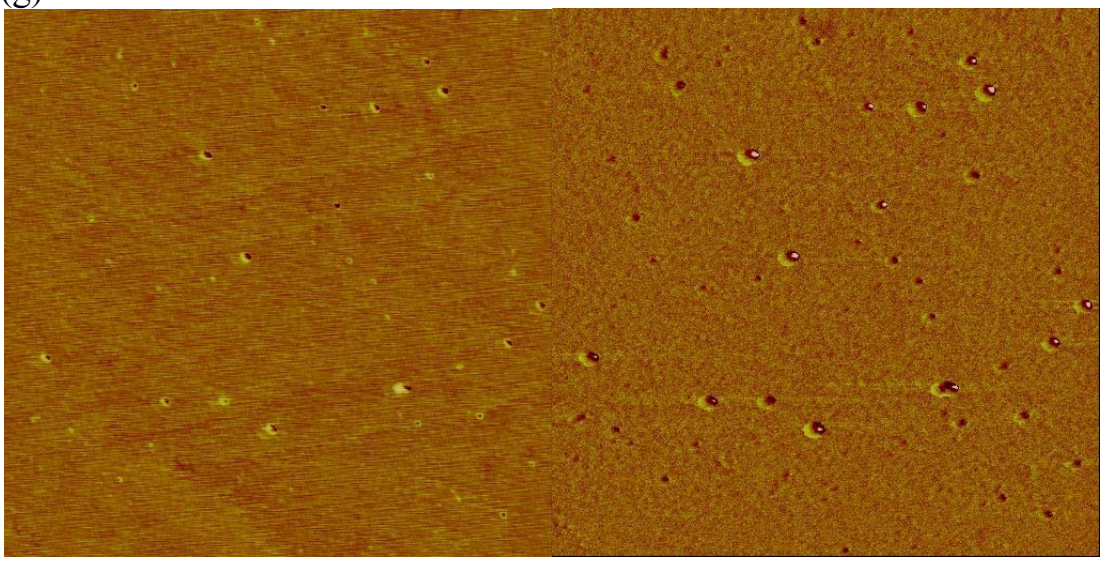

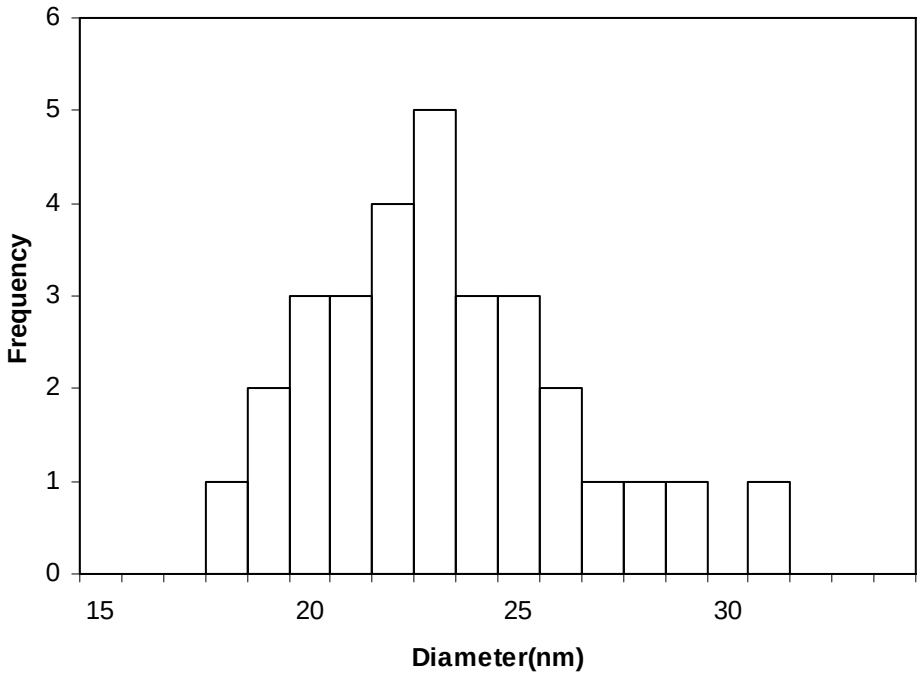

Figure 2.6 (g) AFM height image (upper left), phase image (upper right) and histogram of the diameter (down) of the nano-rings assemblies at pH=10.

(h)

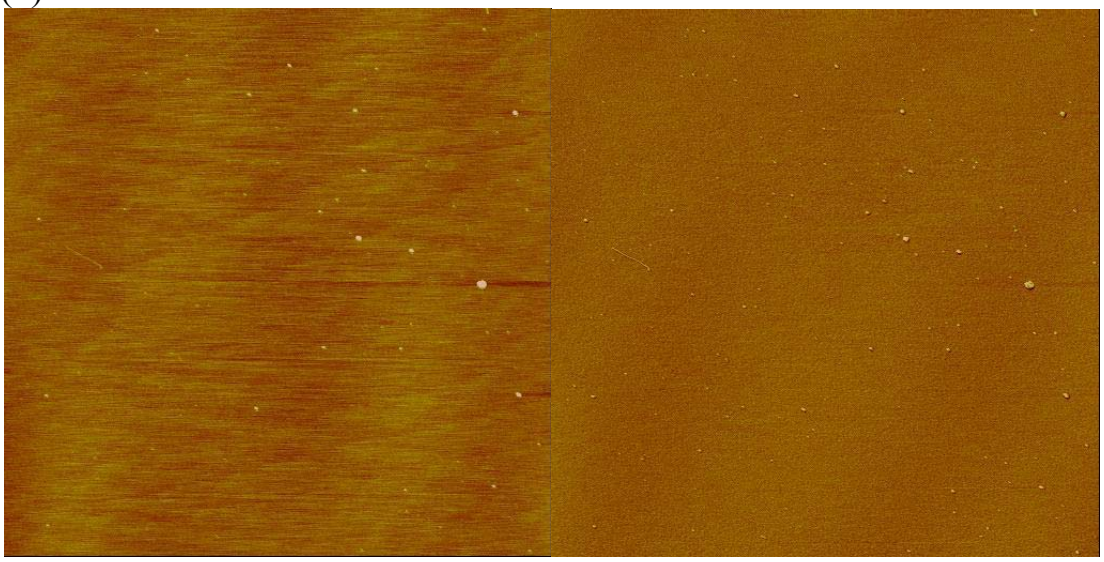

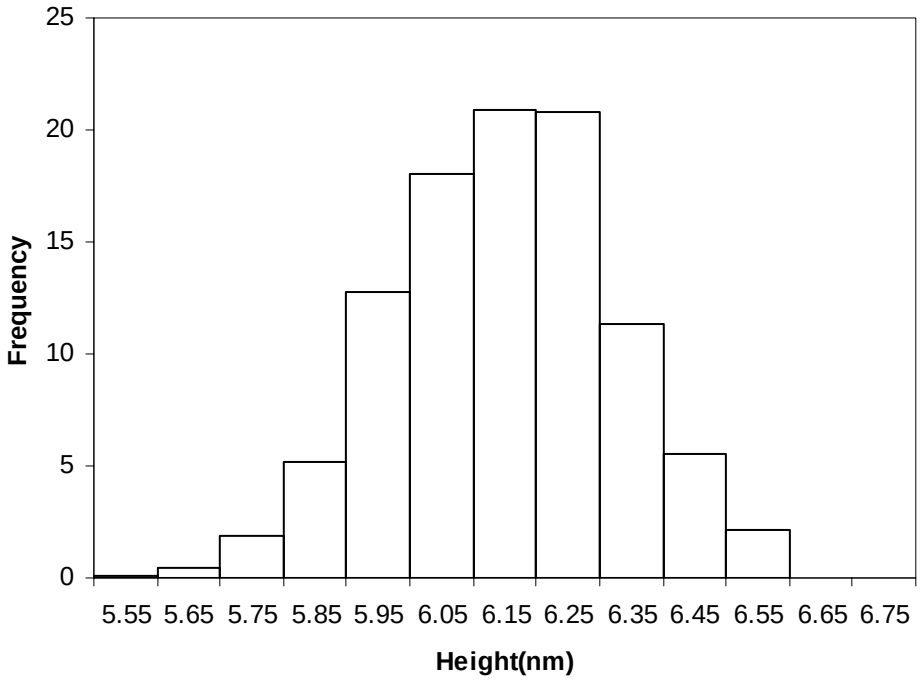

Figure 2.6 (h) AFM height image (up) and histogram of the diameter (down) of the final nanoparticles at pH=10.

The sizes and distributions for the nano-rings assemblies and the final barium titanate nanoparticles at different pH values are abbreviated in **Figure 2.7**.

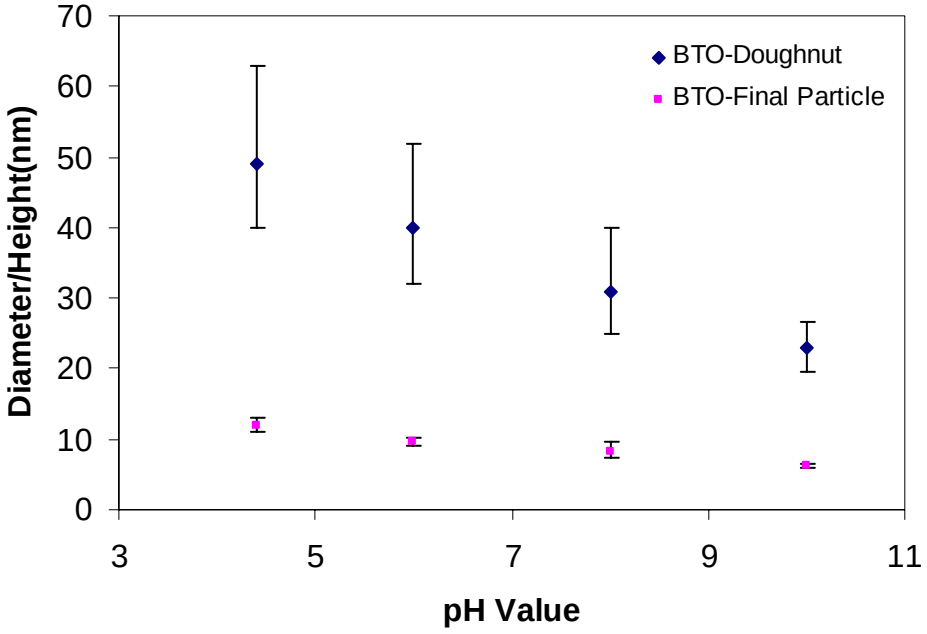

Figure 2.7 Sizes and distributions for the nano-rings assemblies and the final barium titanate nanoparticles at different pH values.

Raman spectrum of the doughnut-$BaTiO_3$ complexes revealed the Ti-carboxylate ligation with their vibrations at 1582, 1362, 1060, and 767 cm^{-1}, as marked in **Figure 2.8**.[78] This chelate structure is consistent with the one between the barium titanate precursors and hydroxylated block copolymer surfaces.[26]

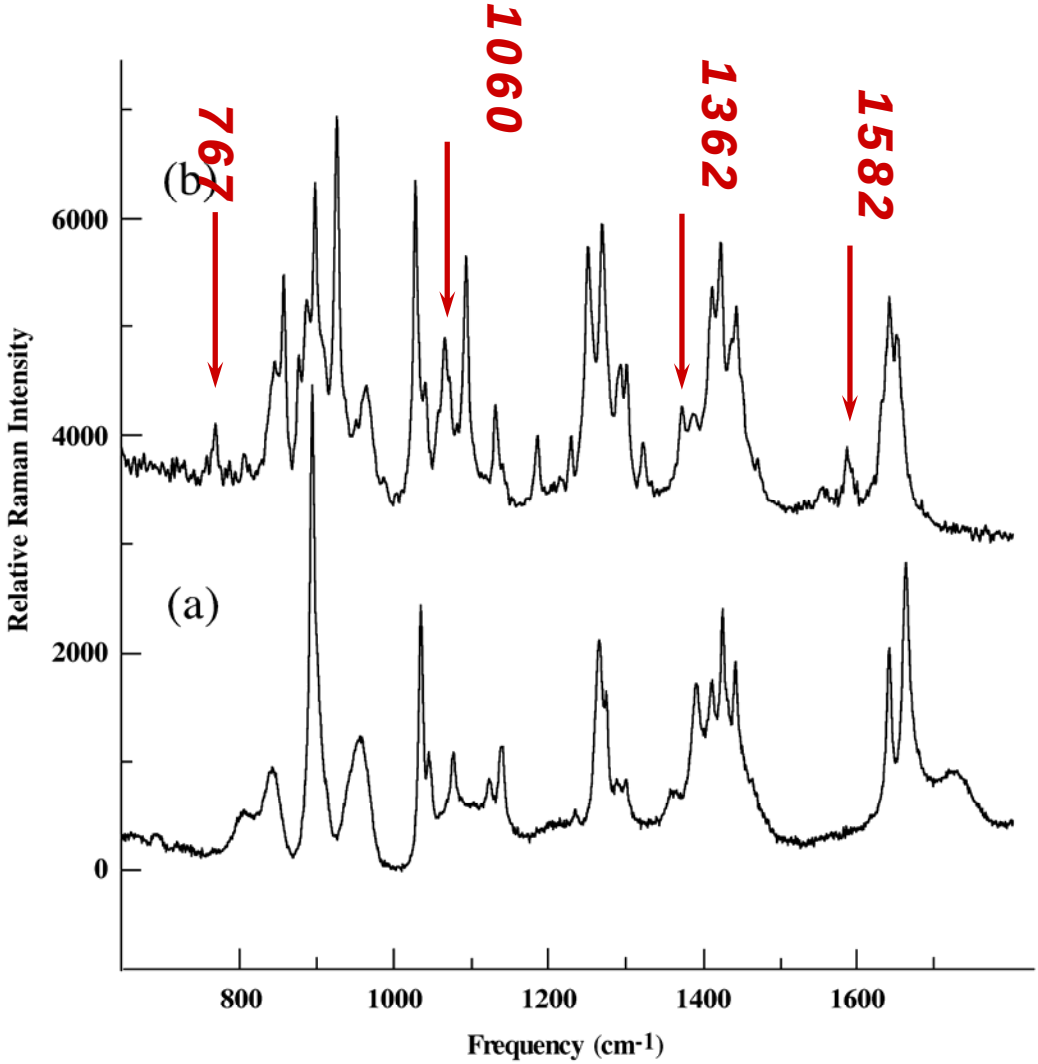

Figure 2.8 Raman spectra of **(a)** nanotubes self-assembled from the peptide monomers without the barium titanate salts **(b)** nano-doughnuts self-assembled from the peptide monomers in the presence of the barium titanate salts.

When the peptide nano-doughnuts with the $BaTiO_3$ nanoparticles were irradiated by UV light (355 nm) for 10 hours in solution, the peptide template shells

were removed as shown in **Figure 2.2**. Previously, Au nanoparticles were also grown in the peptide nano-doughnuts self-assembled from the peptide monomers and Au ions, and long UV irradiation destroyed the doughnut templates due to the reduction of Au ions that chelate carboxylates of the peptide monomers to form the nano-doughnut structure.[76] It is likely that the similar reduction mechanism destroys the nano-doughnut templates for $BaTiO_3$ nanoparticles because the UV irradiation rendered the Ti ions ineffective and can no longer function as a glue to sustain the doughnut structure via the Ti ion-peptide chelation. The AFM image in **Figure 2.6 (b)** shows monodisperse $BaTiO_3$ nanoparticles in the diameter of 12 nm ± 1 nm from a solution at pH=4.4 after UV irradiation to the doughnut-particle complexes for 10 hours. The contrast of nanoparticles in the AFM phase image in **Figure 2.6 (b)** is consistent with the one in the center of nano-doughnuts in **Figure 2.6 (a)**, which suggests that the nanoparticles were released from the nano-doughnuts.

XRD and electron diffraction were employed to investigate the crystalline structure of the final barium titanate nanoparticles. As shown in **Figure 2.9 (a)**, the characteristic peaks, (100), (110), (111), (200), (210), and (211) of $BaTiO_3$ are readily observed. The magnified X-ray diffraction in the inset of **Figure 2.9 (a)** resolves characteristic (002) and (200) peaks of tetragonal $BaTiO_3$ crystals, indicating a ferroelectric tetragonal polymorph was successfully obtained by this biomimetic approach. As reviewed in the first chapter and the introduction section of this chapter, this finding was significant for both fundamental and technical studies. In previous syntheses of barium titanate, the impurity ions on the surface of the final nanoparticles may form a depolarization field to suppress the growth of the

ferroelectric tetragonal structure. In this study, the use of nano-rings assemblies formed a "*protection*" to the attack of the impurity ions at the equatorial directions. The results from this study provide important evidence to show that the so-called "*size effect*" we discussed in the introduction section of this chapter is likely due to the impurity ions on the surface of the nanoparticles, but not an intrinsic nature of smaller sized barium titanate nanoparticles. In the all growth conditions, the resulting $BaTiO_3$ nanoparticles were observed to be very monodisperse and the sizes of $BaTiO_3$ nanoparticles could be changed from 12 nm to 6 nm, as shown in **Figure 2.7**. The advancement of this understanding will contribute deeply to the scientific community for the design of new electronic elements and devices based on nanocrystals as small as 6nm in diameter. The electron diffraction of the resulting $BaTiO_3$ nanoparticles, **Figure 2.9 (b)**, indicates that those nanoparticles are highly crystalline.

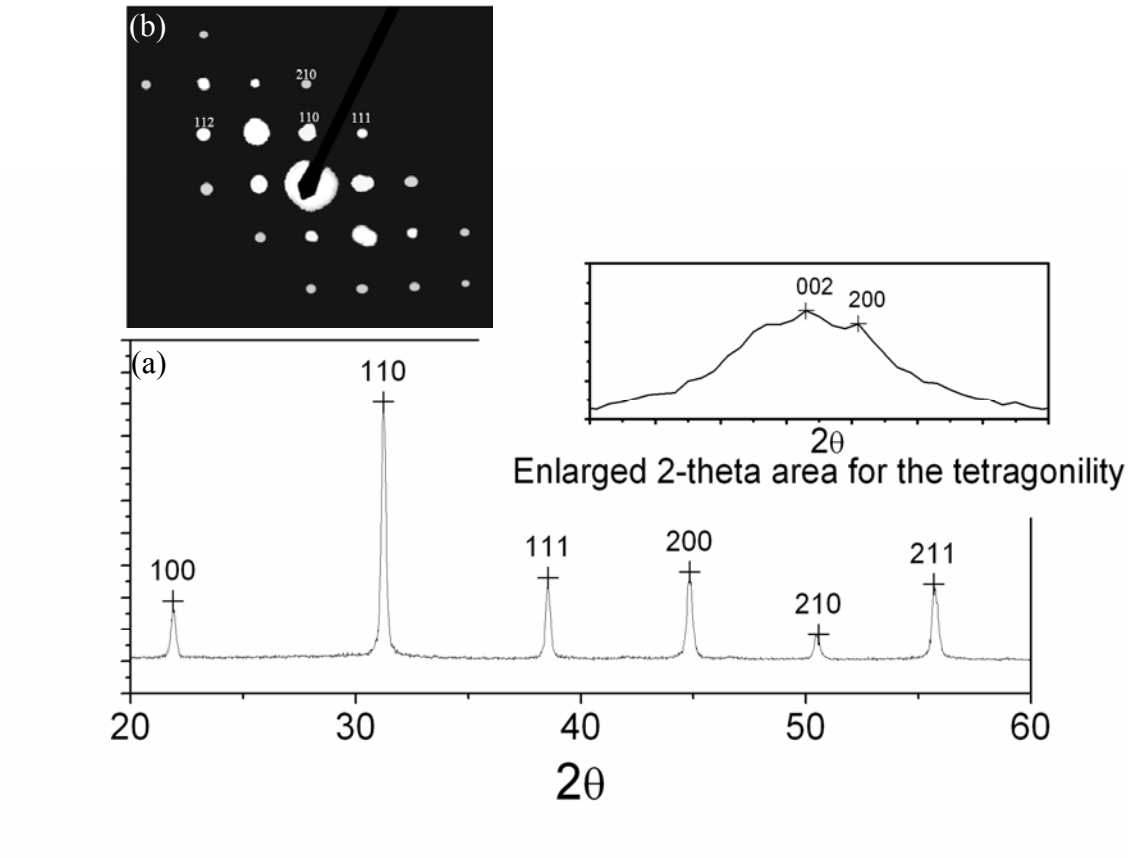

Figure 2.9 (a) X-ray diffraction pattern of barium titanate nanocrystals, from the solution at pH=10, with the enlarged 2-theta area for the assignment of tetragonality; **(b)** Electron diffraction pattern of the same nanocrystals with lattice indices assignments.

Unlike conventional synthetic methods, this technology does not require any nanocrystal surfactants and stabilizers, which enables the production of bare nanocrystals in ultrahigh purity. This process can satisfy the critical requirements for the development of future electronic nano-devices.

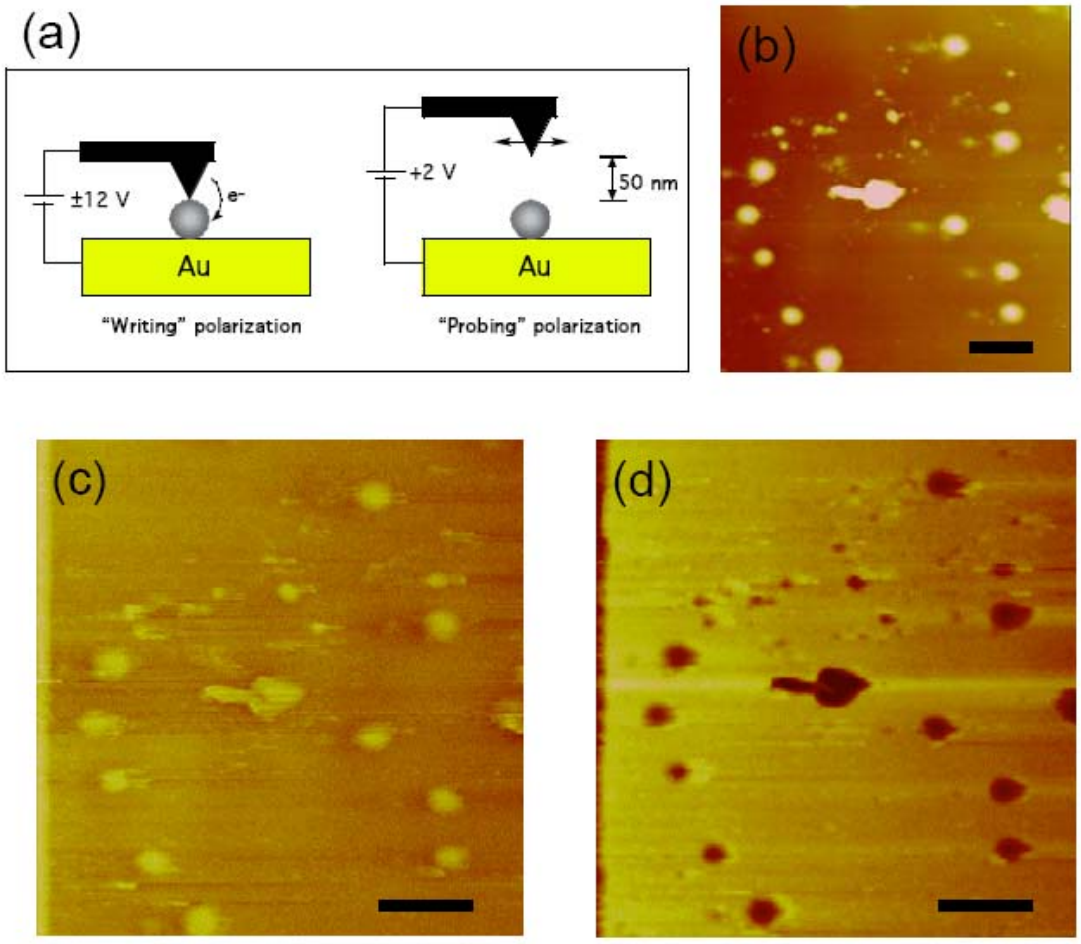

Figure 2.10 (a) The schematic representation of manipulating and probing electric polarization of $BaTiO_3$ nanoparticles with EFM; **(b)** Topological AFM image of barium titanate nanoparticles. Scale bar = 30 nm; **(c)** EFM images of barium titanate nanoparticles with V_{probe} = +2 V after V_{write} = +12 V was applied on the nanoparticles across a conductive AFM tip and a gold substrate. Scale = 30 nm; **(d)** EFM images of barium titanate nanoparticles V_{probe} = +2 V after V_{write} = -12 V, was applied on the nanoparticles across a conductive AFM tip and a gold substrate. Scale = 30 nm.

To test the nano-scale ferroelectric property of tetragonal $BaTiO_3$ nanoparticles, we applied electrostatic force microscopy (EFM) to image and manipulate the ferroelectric polarization of these nanoparticles. The procedure and results are summarized in **Figure 2.10**. At the first step, the electric polarization of $BaTiO_3$ nanoparticles was manipulated by applying a voltage, V_{write}, to the conductive AFM tip that gently contacted on the nanoparticles.[34, 40, 79-82] After the local electric polarization was written on the nanoparticles, the resulting polarization was probed using EFM with a lower voltage, V_{probe}, by measuring the shift in the resonance frequency of the AFM tip.[34, 40] As shown in **Figure 2.10 (a)**, in the probing process, the AFM tip was lifted at the constant distance above the nanoparticles in order to avoid the interference between the manipulated polarization and V_{probe}.[83] The lifted distance at 40 nm enabled us to image only the contribution from the surface charges associated with the local electric polarization of $BaTiO_3$ nanoparticles. After the V_{write} was applied at +12 V to the $BaTiO_3$ nanoparticles with the average diameter of 12 nm (**Figure 2.10 (b)),** the EFM image of those nanoparticles with V_{probe} = +2V in **Figure 2.10 (c)** showed brighter contrast of the nanoparticles as compared to the background due to the repulsive electrostatic interaction between the tip and the nanoparticle.[34, 40] After the V_{write} was applied at -12 V on the same $BaTiO_3$ nanoparticles, the EFM image of those nanoparticles with V_{probe} = +2V in **Figure 2.10 (d)** showed the darker contrast on the nanoparticles as compared to the background due to the attractive electrostatic interaction. It should be noted that the control experiments scanning the manipulated nanoparticles with V_{probe} = -2 V showed reversed EFM images, which confirmed that the probe voltage did not interfere significantly with the written

polarization. These EFM images indicate that the $BaTiO_3$ nanoparticles synthesized in the peptide nano-doughnuts at room temperature possess the ferroelectric property by reorienting the spontaneous electric polarization with the external electric fields.

2.4 Conclusions

In conclusion, ferroelectric $BaTiO_3$ nanoparticles with tetragonal crystalline structure were prepared through hydrolysis of precursors inside the peptide-doughnut templates under ambient conditions. Because the cavity sizes of nano-doughnuts vary as a function of pH, the diameters of monodisperse $BaTiO_3$ nanoparticles obtained could be controlled between 6 nm and 12 nm. The resulting $BaTiO_3$ nanoparticles possess ferroelectric property by reorienting their spontaneous electric polarization under the influence of external electric fields. This unusual crystallization of tetragonal $BaTiO_3$ nanoparticles at room temperature is likely induced by the surface structure of peptide templates and the high surface tension in the nano-scale peptide cavities. This synthetic method involving peptide nano-doughnuts can have broad impact in the growth of various important crystal polymorphs that do not grow under ambient conditions.

Chapter 3

An Open-Bench Method for the Preparation of $BaTiO_3$, $SrTiO_3$ and $Ba_xSr_{1-x}TiO_3$ nanocrystals at 80°C

3.1 Introduction

The remarkable physicochemical properties of $BaTiO_3$ (BTO), $SrTiO_3$ (STO) and $Ba_xSr_{1-x}TiO_3$ (BST), have been attracting a long sustained scientific and technological investigations.[1-3] Such perovskite mixed-metal oxide crystals on the nanometer scale, of high quality and without a history of thermal stress, are highly desirable as fundamental elements for nano-systems involving nano-capacitor and ferroelectrics such as in Ferroelectric random access memories (FeRAM).[4, 5] We present here the *first* synthesis of $Ba_{0.7}Sr_{0.3}TiO_3$ *nano*crystals, in the size range of 50nm to 10nm with achievable giant dielectric constants (1.4 $x10^5$ at room temperature), using a facile synthetic route involving an open-bench system at 80°C. This synthesis is based on results from our preparation of nanocrystals of BTO, STO and BST with various compositions.

BTO and STO are among the most studied perovskite ferroelectrics. In the past, most synthetic procedures for the preparation of perovskite crystals included high temperature (~1000°C) sintering followed by annealing. Recently, extensive efforts have been focused on the establishment of moderate reaction conditions, especially

lowering the synthetic temperature for high-quality nanocrystals.[5-18] Various methods for the synthesis of perovskite nanocrystals have been developed, including co-precipitation,[19, 20] sintering of organometallic precursors,[21] hydrothermal and solvothermal methods,[11-13, 22-24] sol-gel process,[6, 25] and procedures mediated by molten composite-hydoxide.[18] Recent interests in nanoscience led to extensive efforts focusing on obtaining BTO and STO nanocrystals based on the understanding gained from bulk crystals.[4, 26] The synthesis of BST nanocrystals with systematic composition variation has not been reported.

There are special issues in preparing ferroelectric nanocrystals due to their very high surface to volume ratio. The impurity ions on the surface of the nanostructures may form a depolarization field preventing the tetragonal phase to grow.[4, 15, 27, 28] The tetragonal polymorph was usually obtained upon cooling the products to room temperature after a ~1000^{o}C sintering. Although approaches with a trend towards low-temperature synthesis of perovskite nanocrystals have been developed,[12, 13, 18] most of the synthetic temperatures were higher than the Curie temperature (~120^{o}C) of BTO. In Chapter Two, our recent room temperature synthesis of ferroelectric nanocrystals with diameters from 6 to 12nm using a bolaamphiphilic peptide ring as the template was discussed.[15] The peptide ring in the equatorial direction prevented the approach of impurity ions to the particle surface from the lateral direction providing an asymmetric environment conducive to the growth of the tetragonal polymorph. A fungus-mediated biological route toward the synthesis of tetragonal barium titanate nanoparticles of sub-10nm dimensions under ambient conditions was also reported.[16] Most recently, a *bio-inspired* process has been applied for the room-temperature synthesis of BTO from a

bimetallic alkoxide precursor.[17] Nonaqueous approaches have also been developed to synthesize nanocrystalline BTO, STO, and $Ba_{0.5}Sr_{0.5}TiO_3$ mixed-metal oxide using elemental alkaline earth metals as starting materials.[12, 13] The resulting BTO and BST nanocrystals were found to be of cubic polymorph.[29] Based on a reaction between a metallic salt and a metallic oxide, nanometer-sized BTO and $Ba_{0.5}Sr_{0.5}TiO_3$ have also been synthesized in a solution of composite-hydroxide eutectic at ~200^{o}C.[18] Our reverse micelle route performed on a bench top at 80^{o}C gives high-quality nanocrystalline BSTs with variable compositions leading directly to nanocrystals with giant dielectric constants. This finding is significant in providing, through a readily accessible synthetic route, novel particles with size down to the 10nm level for nanoelectronics.

BTO/STO artificial superlattices in thin films have been fabricated by pulsed laser deposition (PLD) on many substrates.[30] PLD method can fabricate of BTO/STO superlattice with stacking periodicity varying from 1:1 to 125:125. Using X-ray diffraction (XRD), the BTO/STO superlattics showed both BTO and STO characteristic peaks, while BST solid solutions from solvothermal method,[12] and our present system only showed characteristic peaks for the BST nanocrystals, indicating the atomic mixing nature of the Ba^{2+} and Sr^{2+} sites.

Reverse micelles as efficient nanoreactors have been applied to the syntheses of nanocrystals.[31] In our syntheses, titanium tetrachloride, strontium chloride and barium chloride aqueous solutions were used as starting materials without organic components to obtain high-quality, homogeneous, stoichiometric BST nanocrystals. The system consisted of a combination of four components of the reverse micelles: cyclohexane

(oil phase), aqueous solution of the metal chlorides, triton X-100 (emulsifier) and n-butanol (co-emulsifier). The system remained stable and transparent up to the point of extensive condensation of hydroxy precursors. The nonionic surfactant allows the optimization of pH for the formation of mixed-metal oxides without altering the micelle structure significantly. The optimum OH^-/Ti^{4+} molar ratio was estblished to be 2 (see Section 3.2, Experimentals). The use of only inorganic substances in reverse micelles is of importance for the following reasons: (1) the impurity ions can be readily removed from the final products by washing with water; (2) total inorganic starting materials are ideal for the aqueous phase in the reverse micelle so that all the reactions are confined inside the nanoreactors; (3) the reaction temperature of 80^oC, is much lower than that of reported synthetic procedures for BST; (4) the same micelle system can be used to make nanocomposites of BST with polyelectrolytes or conducting polymers by emulsion polymerizations in a one-pot method.[32]

3.2 Experimentals

All chemicals were purchased from Aldrich. In a typical synthesis, 6.39g of hydrochloric acid (37%) solution containing 47% of $TiCl_4$ (99.9%) and 15mL deionized (DI) water were mixed and used as the aqueous phase, and cyclohexane (99%, 23g) as the oil continuous phase. Triton X-100 (laboratory grade, 25g) and n-butanol (99.4%, 28g) were selected as the emulsifier and co-emulsifier respectively. The chemicals were then transferred to a 500ml flask equipped with a stirrer, a thermometer, a dropping funnel and a reflux condenser. With stirring, a 40% NaOH (97%) solution was added dropwise into the flask until pH=7. A stoichiometric amount of $SrCl_2 \cdot 6H_2O$, 99%, (or

$BaCl_2 \cdot 2H_2O$, 99%) was dissolved in DI water (25ml) and then added to the flask dropwise under continuous stirring. Additional 40% NaOH aqueous solution was then added dropwise into the colloid system until OH^-/Ti^{4+}=2/1. This reaction system was then kept at 78-80^oC for 3 hours prior to centrifugation at 4000rpm for 15min. The resulting sediment was redispersed in DI water using an ultrasonic bath. This centrifugation-redispersion cycle was repeated at least three times to remove emulsifiers and other ionic impurities. The final particles were dried in vaccuo at 80^oC over night. In the preparation of BST of different sizes, the amount of oil phase, emulsifier and co-emulsifier were kept constant, and all the aqueous contents were varied by a factor of either 0.5 or 0.25. The dried BST powders were characterized by X-ray diffraction (XRD, Philips PW3040) for crystalline phase determination. Transmission electron microscope (TEM, JOEL 1200 EX) and electron diffraction at an acceleration voltage of 100 kV were used to characterize the morphologies and crystalline structures of BST solid solutions. EDS studies were conducted on a LEO 1530 electron microscope combined with an Inca EDS Microanalysis Systems (Oxford Instruments). The dielectric constant measurements were conducted on a Novocontrol BDS 80 high-resolution broadband dielectric spectrometer with a sample holder cell (diameter: 19.21mm; thickness: 0.27mm).

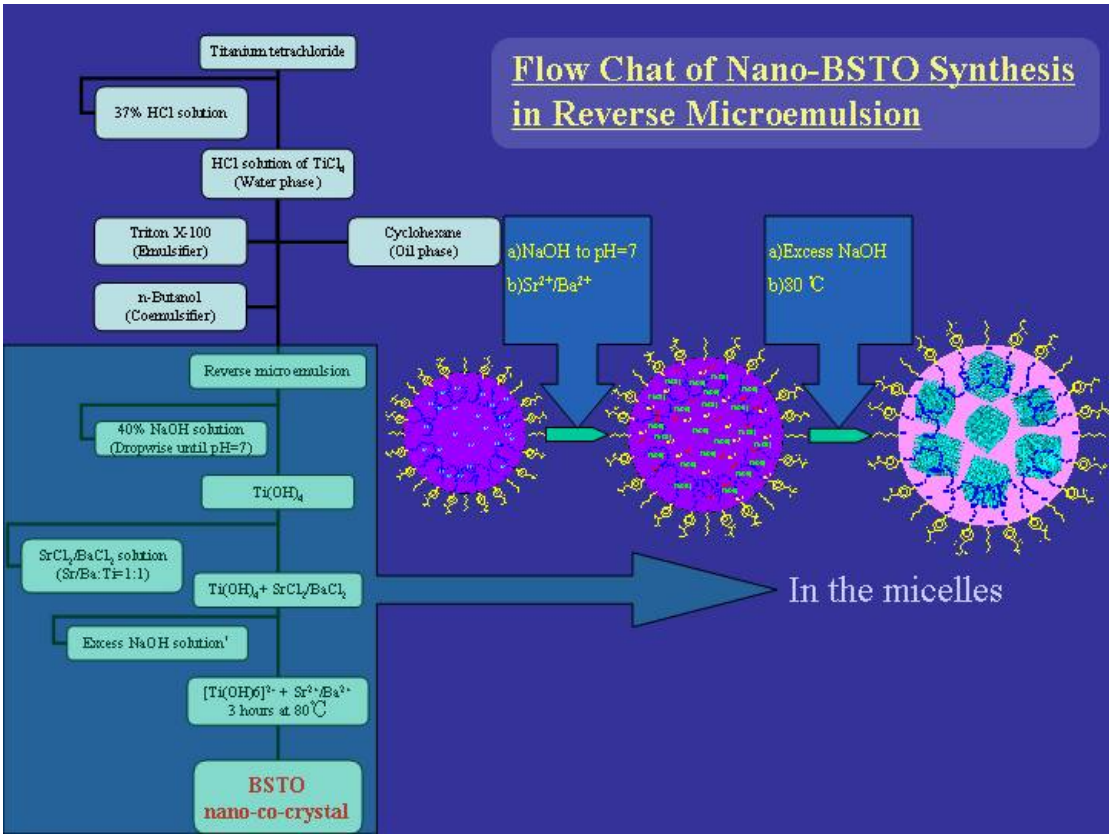

Scheme 3.1 Synthetic flow chart for nano-BST by reverse micelles.

3.3 Results and Discussions

The nanocrystals synthesized using our open-bench method are of high quality based on data from XRD, Fourier transform infrared (FTIR) spectroscopy, energy dispersive X-ray spectrometry (EDS) and TEM. **Figure 3.1** shows the XRD pattern of BTO nanocrystals, no characteristic peaks from $BaCO_3$ or TiO_2 impurities were observed.

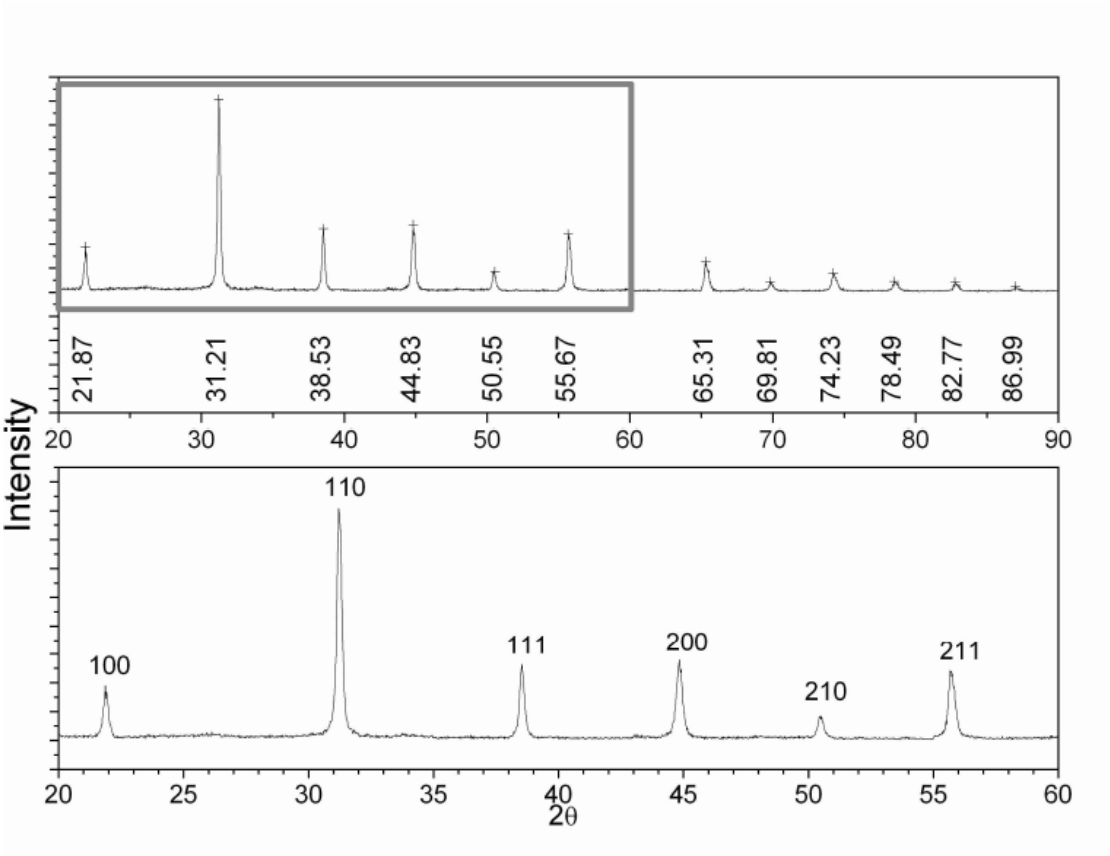

Figure 3.1 XRD patterns of BTO nanocrystals.

The BTO lattice parameters are in agreement with the reported data (JCPDS No. 31-174). The quality of the products from our synthetic and purification procedure was further established by FTIR and EDS. These analytical data (**Figure 3.2** and **3.3**) from

our nanocrystals serve as examples of the high quality achievable by our reverse micelle synthetic procedure. For example, in the spectrum of STO (**Figure 3.2**), there are no observable vibrational peaks from organic impurities. The absorption at 534 cm^{-1} indicates the formation of Ti-O octahedra and the broad peak at 3358 cm^{-1} reflects the absorption from surface hydroxyl groups. In the EDS analysis of BTO (**Figure 3.3**), no detectable Cl or Na peaks were observed, indicating that Cl^- and Na^+ ions were efficiently removed from the final products by thorough washing.

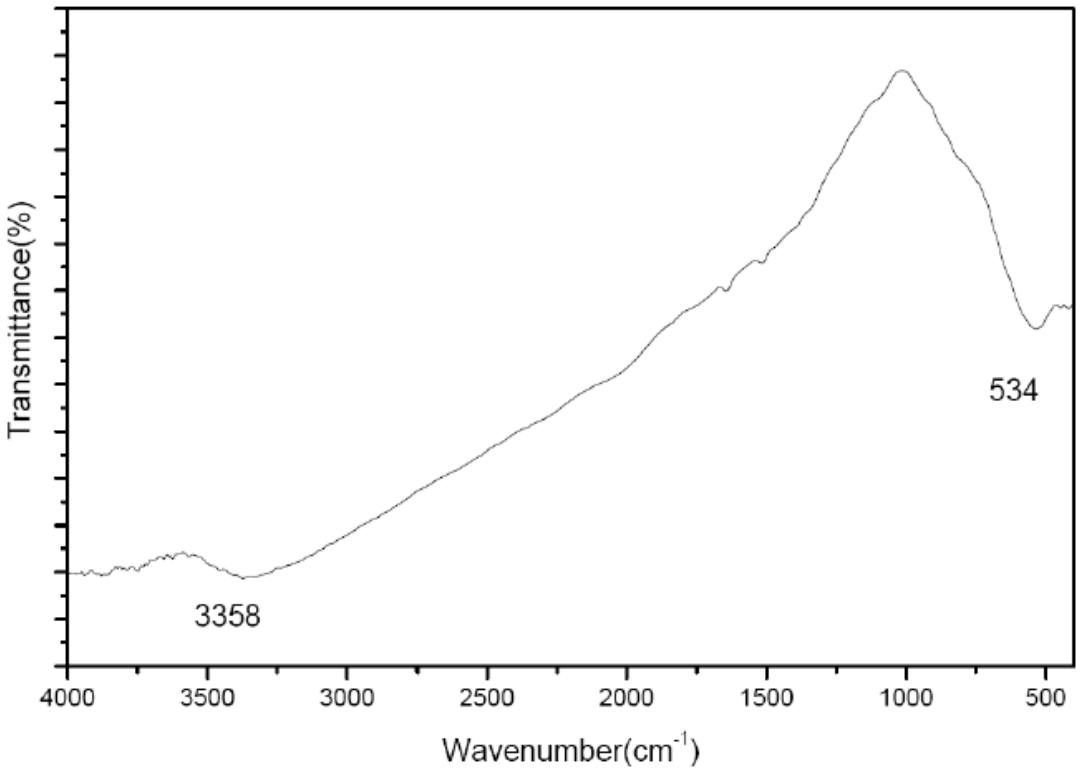

Figure 3.2 FTIR spectrum of STO nanocrystals.

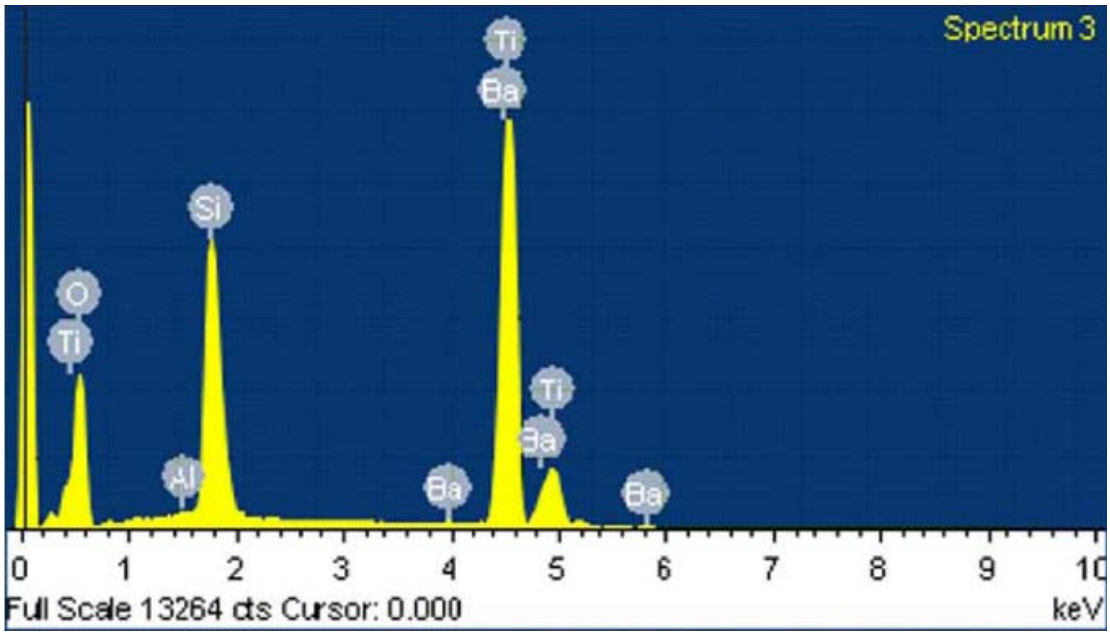

Figure 3.3 EDS spectrum for BTO nanocrystals. Si signal is from the silicon wafer supporting substrate.

The manipulation of the Ba^{2+}/Sr^{2+} molar ratio in the BST nanocrystals was demonstrated by the synthesis of a series of BST nanoparticles with the molar fractions of Ba^{2+} varied in the steps of 0.1. The XRD of $Ba_xSr_{1-x}TiO_3$, **Figure 3.4 (a)**, with the full range of compositions show a single 200/002 peak for each composition, indicating the formation of true solid solution with atomic mixing of Ba^{2+} and Sr^{2+} rather than superlattice which would show separate BTO and STO peaks.[30] With the change in the composition of BST, the trend of 2θ for the 200/002 peak and the variation in dielectric constant are depicted in **Figure 3.4 (b)**. The 2θ value decreased from 46.74 to 44.83 with increasing Ba^{2+} molar fraction, indicating the lattice unit expanded from 3.904 to 4.039Å. The decrease of 2θ values for the series of BST nanocrystals shows three distinct regions in **Figure 3.4 (b)**. The highest rate of lattice expansion with increase in

Ba^{2+} takes place in the range of x=0.3 to 0.7. This is the first systematic investigation of BST with methodical composition variation.

As expected, the change of the features of XRD is most pronounced in the range of near equal Ba^{2+} and Sr^{2+} compositions (x=0.4 to 0.6). In this region, the 111 peaks show much greater variation than the 200 peaks; the former plane is defined by periodicity involving less atomic positions than the latter, thus more sensitve to changes in Ba^{2+}/Sr^{2+} composition ratios. At x=0.5, the XRD data showed a decrease in crystallinity with further deterioration at x=0.6. There is a conspicuous return to the previous level for high-quality crystals at x=0.7. From x=0.7 to pure BTO, a gradual change toward BTO peak positions for both 111 and 200 peaks was observed. As shown in Figure 2b, the room temperature static dielectric constant has a marked jump at x=0.7 to a high level of $1.4x10^5$. This maximum was observed previously for bulk crystals,[33-35] and in agreement with molecular dynamic calculation.[36] The giant dielectric constant observed indicates the tetragonal polymorph of the nanocrystal. In the low size range of 50 to 10nm, XRD data can not be used to rule out the presence of cubic polymorph.[37]

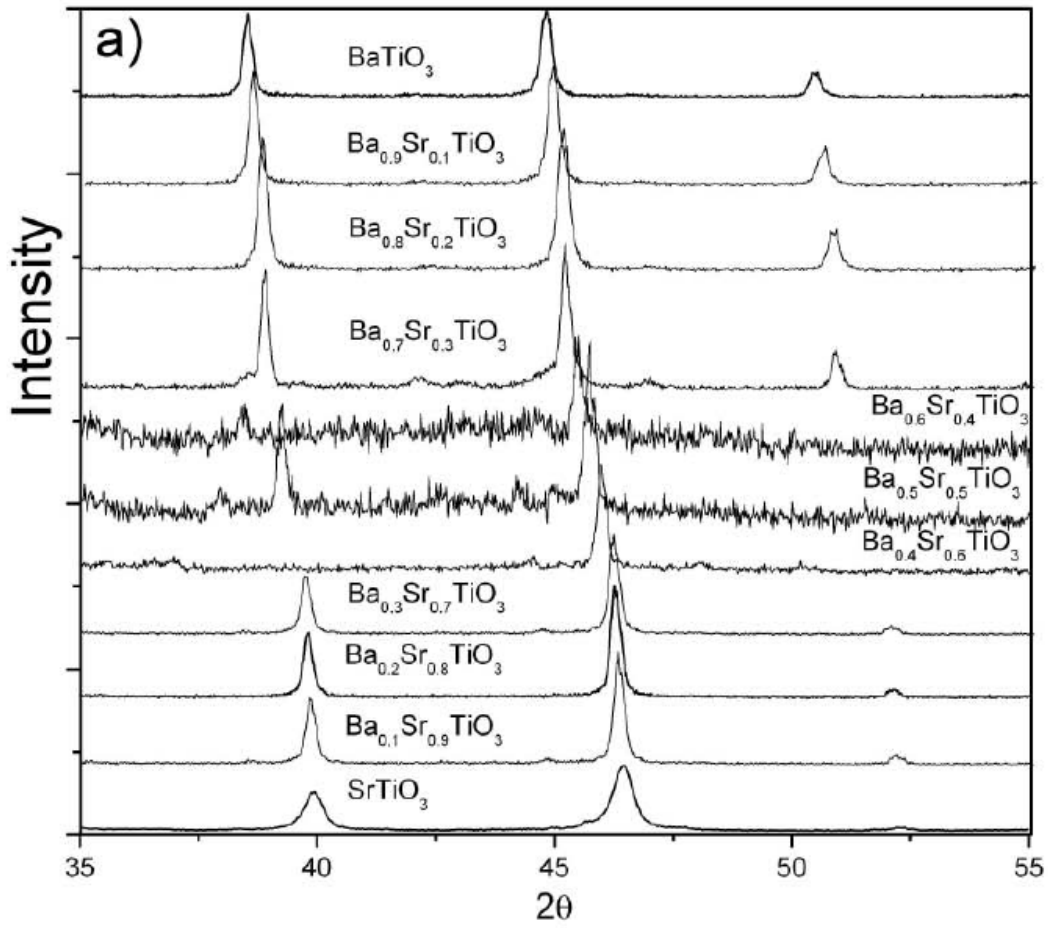
a)
BaTiO3
Ba0.9Sr0.1TiO3
Ba0.8Sr0.2TiO3
Ba0.7Sr0.3TiO3
Ba0.6Sr0.4TiO3
Ba0.5Sr0.5TiO3
Ba0.4Sr0.6TiO3
Ba0.3Sr0.7TiO3
Ba0.2Sr0.8TiO3
Ba0.1Sr0.9TiO3
SrTiO3
Intensity
35
40
45
50
55
2θ

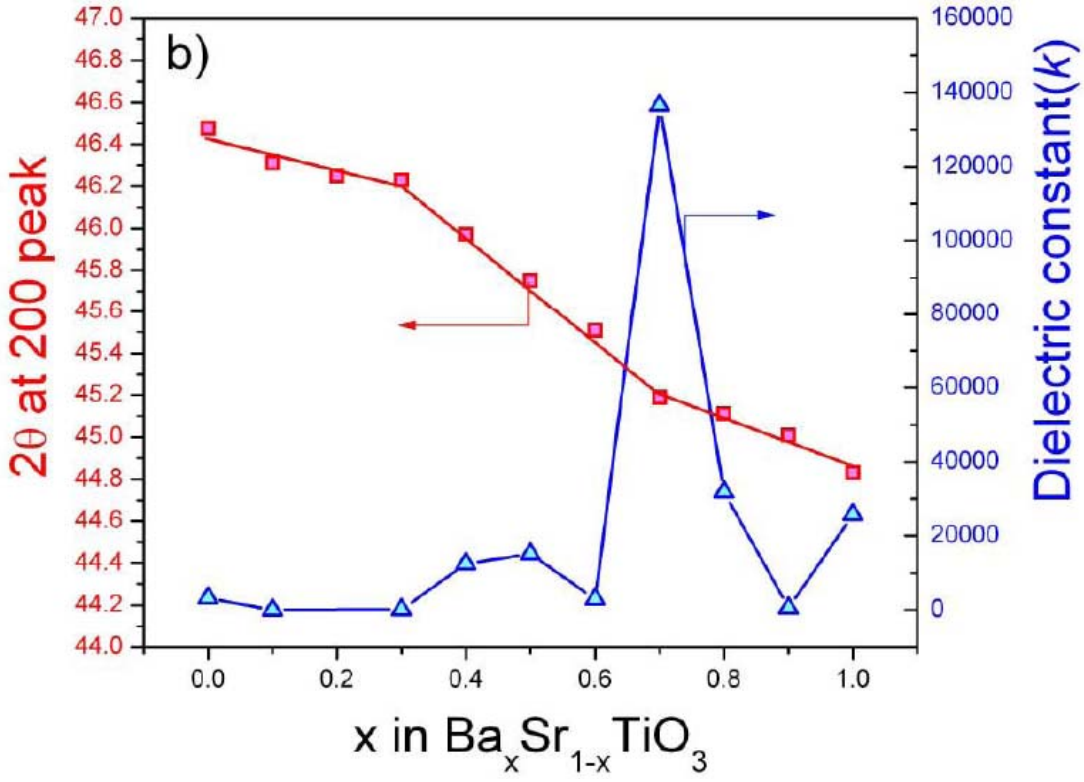

Figure 3.4 XRD and dielectric results for BTO, STO and BST nanocrystals. **(a)** The XRD patterns for BST nanocrystals. **(b)** The shifting of 2θ value at 200/002 peaks and the static dielectric constants for BST with increasing of Ba^{2+} molar fraction. ■-2θ values in XRD; Δ-static dielectric constant values.

The TEM images and electron diffraction patterns of BTO, STO, and $Ba_{0.7}Sr_{0.3}TiO_3$ nanocrystals are shown in **Figure 3.5**. The BTO nanocrystals have an average size of 80nm in **Figure 3.5 (a)** and **(e)**. Thus, bypassing the final high temperature sintering process avoided the formation of agglomerates. The electron diffraction pattern, **Figure 3.5 (d)** also indicates that the synthesis gave directly high-quality nanocrystals. Both the shape in TEM and the spot matrix in the electron diffraction pattern support the preparation of single-crystalline BTO nanoparticles at a

temperature as low as 80^{o}C. **Figure 3.5 (b)** and **(g)** show the TEM of STO nanocrystals as non-agglomerated nanocubes with an average size of 70nm. The electron diffraction pattern with lattice indices in **Figure 3.5 (f)** shows the single crystalline nature of STO nanocrystals. Unlike STO and BTO, the $Ba_{0.7}Sr_{0.3}TiO_3$ nanocrystals show rather uniform nanospheres in the TEM image, **Figure 3.5 (c)** and **(i)**, with an average diameter of 50nm. The electron diffraction patterns, **Figure 3.5 (d)**, **(f)**, and **(h)**, are in agreement with XRD results.

The preparation of $Ba_{0.7}Sr_{0.3}TiO_3$ nanocrystals with giant dielectic constant was extended to still lower size ranges, 20 to 10 nm, based on fine tuning the size of the aqueous micelles through changing the surfactant to water ratio. Particles in this low size range can have potential application to FeRAM. Keeping the oil phase, emulsifier and co-emulsifier amounts constant, and changing the amount of the aqueous contents by ½ and ¼ led to uniform BST nanoparticles of smaller sizes: 15-20nm in diameter from the system the ½, **Figure 3.6 (a)** and **(b**), and 5-10nm in diameter from the ¼, **Figure 3.6 (c)** and **(d**).

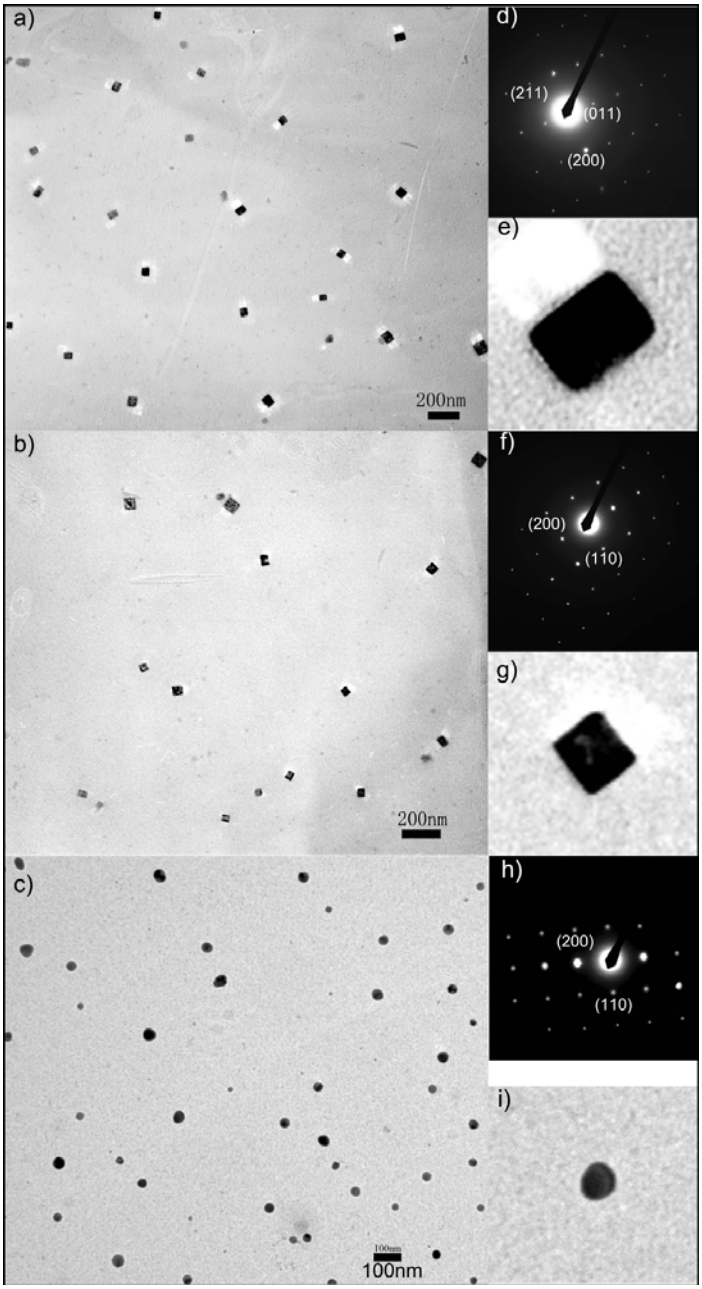

Figure 3.5 TEM images and electron diffraction of BTO, STO and $Ba_{0.7}Sr_{0.3}TiO_3$: **(a-c)** TEM images of BTO, STO, and $Ba_{0.7}Sr_{0.3}TiO_3$, respectively. **(d, f** and **h)** the electron diffraction patterns of BTO, STO, and $Ba_{0.7}Sr_{0.3}TiO_3$, respectively. **(e, g** and **i)** TEM images of BTO, STO and $Ba_{0.7}Sr_{0.3}TiO_3$ in high magnification, respectively.

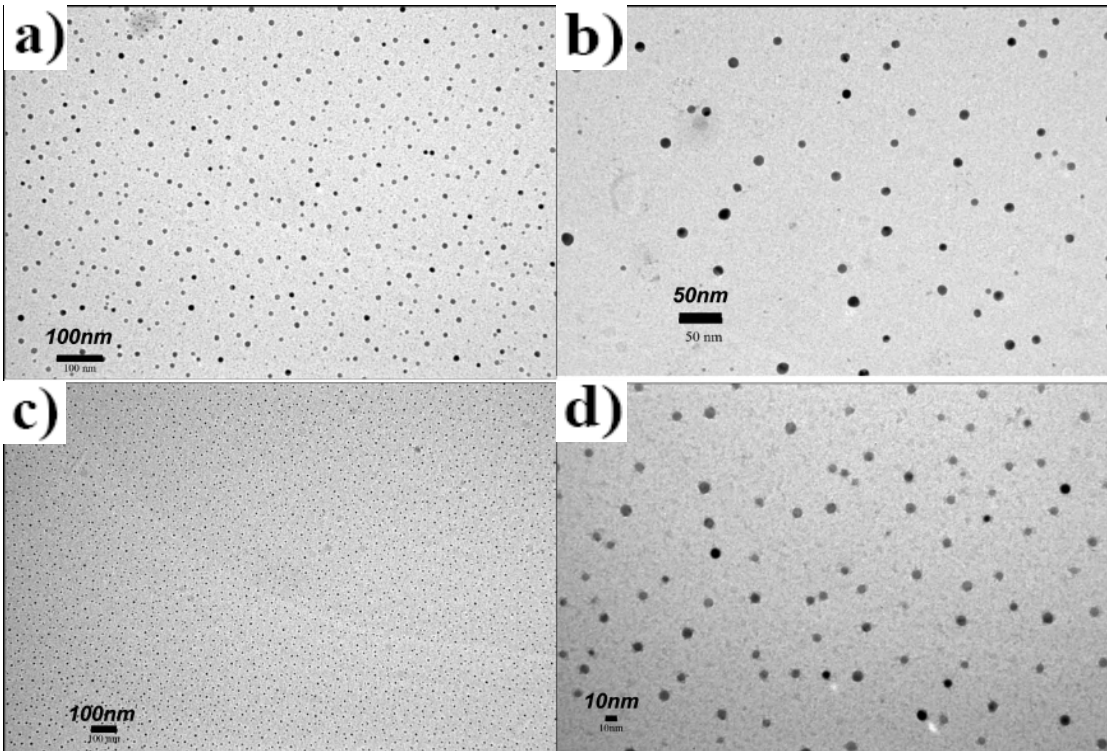

Figure 3.6 TEM images of $Ba_{0.7}Sr_{0.3}TiO_3$ nanoparticles from different synthetic conditions: **(a, b)** the amount of all aqueous contents equals to 0.5 of the original amount; **(c, d)** the amount of the aqueous contents equals to 0.25 of the original amount.

3.4 Conclusions

In summary, an efficient open-bench method has been discovered for the synthesis of high-quality STO, BTO nanocrystals and BST nano-solid-solutions with variable compositions and size range. The 80^{o}C temperature of the synthetic process represents nanocrystal formation below the Curie temperature of BTO. This open-bench process allows the direct, facile preparation of BST single-nano-crystals with giant static dielectric constant without a history of thermal stress. The optimized reverse micelle method led to high-quality nanocrystals as supported by XRD, electron diffraction, TEM, FTIR and EDS data. The shifting of 2θ value at 200/002 peak reflects the increasing of the lattice unit dimension with increasing Ba^{2+} molar fraction as expected. Synthesized BTO and STO are single crystals of cubic shape, while the $Ba_{0.7}Sr_{0.3}TiO_3$ nanocrystals of spherical shape. The size of the BST nanoparticles can be readily tuned from ~50nm to ~10nm using our reverse micelle approach. These findings can have significant impact for the development of FeRAM application. This simple open-bench method represents a significant contribution to the perovskite nanocrystal synthetic methodology. This new procedure does not require demanding conditions such as high temperature, high pressure, and inert environment and only involves handling of common components.

Chapter 4

Single Crystalline Organic Nanoneedles with Fast Conductance Switching Properties from An Interfacial Polymerization-Crystallization of Conjugated Monomers[1]

4.1 Introduction

Nanometer-scale science has been one of the most exciting areas of recent investigations. The focus of activities has been on both fundamental as well as technological significance. New physical phenomena and revolutionary nanoelectronic devices based on discoveries of novel nanomaterials can be anticipated. Organic conjugated systems have been applied successfully to electronics based on their versatile electronic properties and adaptability to a broad range of processing methods.[2-15] However, the development of *polymer electronics in the nanometer scale* can only be considered in an embryonic stage. We report here the first synthesis of polythiophene nanoneedles with fast field-induced conductance switching properties in a single nanocrystalline element.

Most bulk conducting polymer systems studied consist of regions of inhomogeneity. The investigation of the processes in the nano-domain representing pure crystals is critical in ascertaining the inherent electronic properties of polymer nano-elements. Single *nano*crystals of conducting polymer have not been reported, although needle-shaped bulk crystals of quaterphenyl cation radical salt were previously studied,[16, 17] and highly ordered polymer structures were prepared by

methods including electrochemical epitaxial polymerization,[11] solution spin-coating on functionalized surface,[18] and solid-state polymerization of monomer crystals.[19] To date, polythiophenes together with polyanilines and polypyrroles represent the most important group of conducting polymers.[20] Applying an interfacial polymerization-crystallization process, we have prepared single crystals of poly(3, 4-ethylenedioxythiophene) (PEDOT) in a nanoneedle form. The aqueous/organic interfacial system used was composed of 3, 4-ethylenedioxythiophene (EDOT) in an organic solvent and an oxidant, ferric chloride ($FeCl_3$), in DI water. The use of ferric chloride as oxidant in the precipitation polymerization of thiophenes has been documented.[21-23] In such cases, polymer chains are generally formed first, followed by precipitation formation of crystals. Our system represents the first use of ferric chloride in the interfacial polymerization of thiophenes. This polymerization proceeds with an attendant crystal growth, thus higher order of crystal packing can be expected.

Higher order in conducting polymer crystals is essential for the applications in nanoelectronics. The advancement of the interfacial polymerization-crystallization technique to a broader variety of monomers, including aniline and pyrrole, can establish the finding as a general route for the fabrication of conducting polymer nano-elements. **Scheme 4.1** gives the chemical structures polyaniline (PANI) and polypyrrole (PPY) in undoped forms. Highly ordered PANI and PPY nanoneedles were also prepared by applying the similar synthetic technique. Thus, the interfacial polymerization-crystallization process can serve as a route for the fabrication of a broad range of conjugated electroactive polymers.

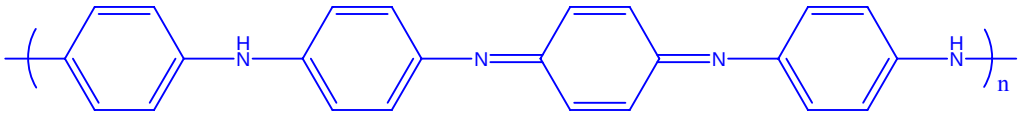

Polyaniline

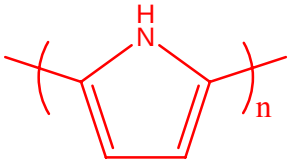

Polypyrrole

Scheme 4.1 Chemical structure of polyaniline and polypyrrole.

4.2 Single Crystalline Organic Nanoneedles with Fast Conductance Switching Properties from An Interfacial Polymerization-Crystallization of Thiophenes

4.2.1 Experimentals

4.2.1.1 Interfacial Polymerization

All reagents for synthetic procedures were purchased from Aldrich Chemical Co. and used without further purification. In the interfacial synthesis, EDOT or 3-hexylthiophene (3HT) (1mg/mL) was dissolved in dichloromethane (DCM), pentane or n-butanol, and ferric chloride (1mg/mL) in DI water. The interfacial polymerization was conducted in a 20-mL vial containing 5mL monomer solution and 5mL $FeCl_3$ solution. The water layers were collected after 48 hours.

4.2.1.2 Purifications

Five drops of concentrated HCl solution (37%) were added into the collected suspension. The nanoneedle suspension was then centrifuged and re-suspended three times followed by a final dialysis process for 10 hours using a dialysis tubing (D9277, Sigma-Aldrich) in ultrapure water (resistivity: 18.2 MΩ cm, total organic carbon levels: 10 ppb).

4.2.1.3 Characterization by TEM, Electron Diffraction, HRTEM, SEM/EDS, EPR, and STM/STS

After the purification, the aqueous suspension was 10-fold diluted for the transmittance electron microscopy (TEM), electron diffraction, high-resolution TEM (HRTEM), Energy dispersive X-ray spectroscopy (EDS), electron paramagnetic resonance (EPR) and scanning tunnelling microscopy/spectroscopy (STM/STS) characterizations. TEM and electron diffraction were conducted on a JEOL 1200 EX microscope. HRTEM was conducted on a Tecnai G2 F20 cryoelectron microscope. EDS studies were conducted on an Amray 1910 microscope combined with a Noran system SIX X-ray microanalysis system (Thermo Electron Corporation). EPR spectrum was recorded on a Bruker EPR ESP 380E spectrometer. STM/STS studies were conducted on a PicoSPM II system (Molecular Imaging). For the STM/STS sample preparation, the diluted nanoneedle suspension was spin-coated onto an Au-111 surface (purchased from Molecular Imaging), which was freshly annealed by the provider and used immediately after delivery. Ir/Pt STM tips were purchased from Molecular Imaging and used for all the STM/STS measurement.

4.2.1.4 Self-assembly of the Nanoneedles

The purified PEDOT nanoneedle suspension was first dried under ambient conditions for 10 days and then dried in vacuo at room temperature. Dark green PEDOT powders was collected and examined by SEM/EDS for the morphological and chemical composition study of the self-assemblies from PEDOT nanoneedles.

4.2.2 Results and Discussions

In a typical synthesis, EDOT, or 3HT, dissolved in dichloromethane (DCM, 5mL, 1mg/mL) served as the lower organic layer and $FeCl_3$ dissolved in DI water (5mL, 1mg/mL) as the upper layer. Pentane or n-butanol was also used for the interfacial polymerization. In these cases, the organic layer containing monomers was the upper layer and the aqueous layer the lower layer (**Scheme 4.2**). The growth direction was the reverse of the gravitational direction. After 2 days, the aqueous layer was then carefully collected for purification. To prevent the hydrolysis of $FeCl_3$, 5 drops of concentrated HCl solution (37%) were added into the collected suspension. The nanoneedle suspension was then centrifuged and re-suspended three times followed by a final dialysis process for 10 hours using a dialysis tubing (D9277, Sigma-Aldrich) in ultrapure water (resistivity: 18.2 MΩ cm, total organic carbon levels: 10 ppb). The oxidative coupling polymerization of EDOT involving an aqueous/organic interface was facilitated by $FeCl_3$,[24] representing a system of *crystallization during polymerization* in the nano-regime (**Scheme 4.3**). This oxidative coupling of EDOT was much slower than the fabrication of polyaniline (PANI) nanofibers from a similar process.[25] The PEDOT nanoneedle samples were

usually collected after 48 hours while the formation of PANI nanofibers using persulfate as the oxidant required at most 10 minutes. Unlike the usual solution polymerization followed by a formation of insoluble crystals, this slow coupling polymerization involved an interface mediating the formation of superior crystal packing in the product. The nanocrystals are composed of PEDOT from an ensemble of degrees of polymerization, as expected from their needle shape, with inner chains longer than the outer ones. Based on the 50 nm needle length, longest possible chain would have 126 thiophene rings. There may be more than one chain tip-to-tip. Due to the very limited solubility of the crystals, the polymer size distribution can not be directly measured at this time.

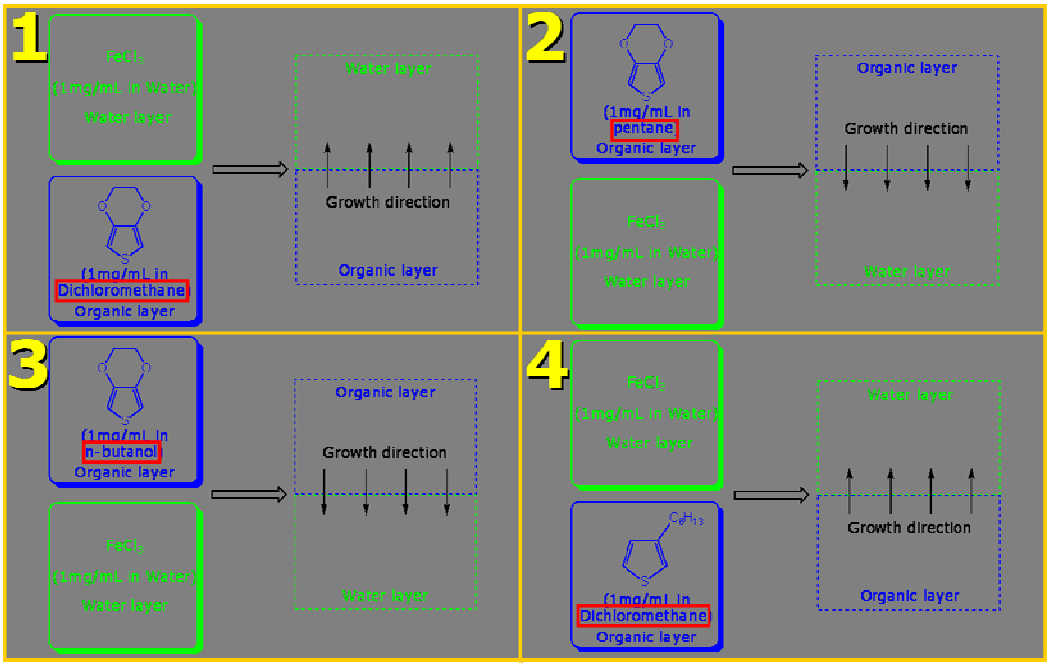

Scheme 4.2 Experimental design for the interfacial polymerizations of EDOT or 3-hexylthiophene (3HT) from different systems with the variation of the oil phase, DCM, pentane or n-butanol.

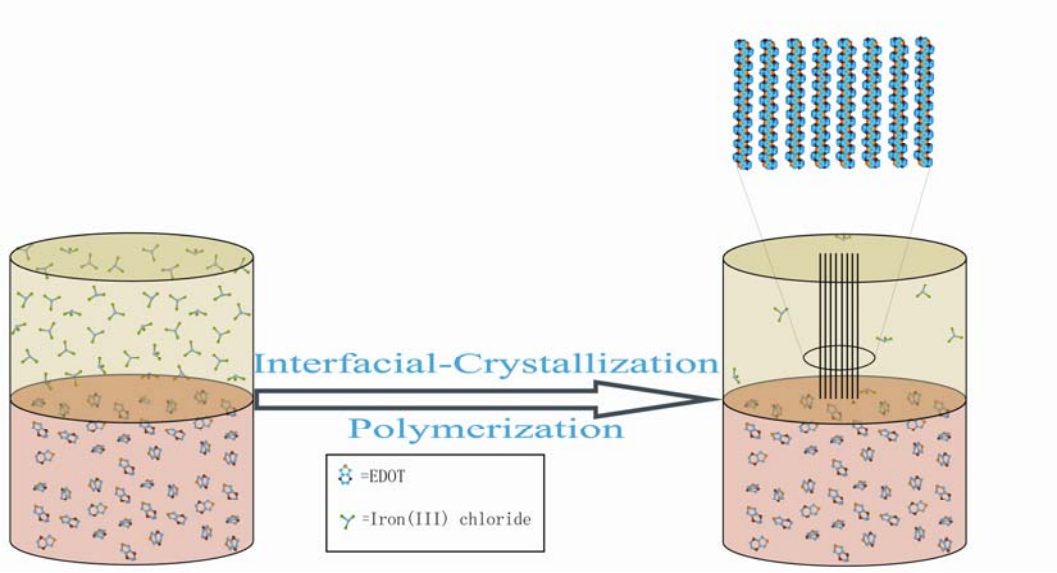

Scheme 4.3 Synthetic scheme of the interfacial polymerization-crystallization of EDOT mediated by ferric chloride from the water/DCM system.

Conducting polymer samples are considered, in general, as inhomogeneous systems with isolated crystalline domains.[26, 27] The structural order in polythiophene and its derivatives could be very complicated.[27-31] To obtain a highly crystalline conducting polymer sample, special techniques need to be applied. For example, highly crystalline polythiophene can be obtained by a coupling reaction of pre-organized monomer crystals[19]. The PEDOT products from our system show clearly nanoneedle structures having a width of about 15nm and a length of about 50nm with pointed tips (**Figure 4.1 (a, b)**: transmission electron microscopic, TEM, images, JEOL 1200 EX microscope). To our best knowledge, this is the first reported needle-shaped conducting polymer *nano*crystalline structure. The initial formation of PEDOT nanoneedles was most likely from the interface with subsequent migration to the aqueous phase as polymer nanoneedles grow. To establish the general

applicability of this interfacial system, pentane instead of DCM was also used as the organic layer for EDOT monomers. The organic pentane layer then served as the upper layer and the migration direction of nanoneedles was in the gravitational direction. The TEM images (**Figure 4.2**) show a similar nanoneedle structure. But the tips of the nanoneedles are not as sharp as those from DCM. By using n-butanol (**Figure 4.3**) as the organic layer, the nanoneedles of PEDOT show less order than those from DCM and pentane. This phenomenon is likely due to the more polar nature of n-butanol than that of the other two organic solvents.

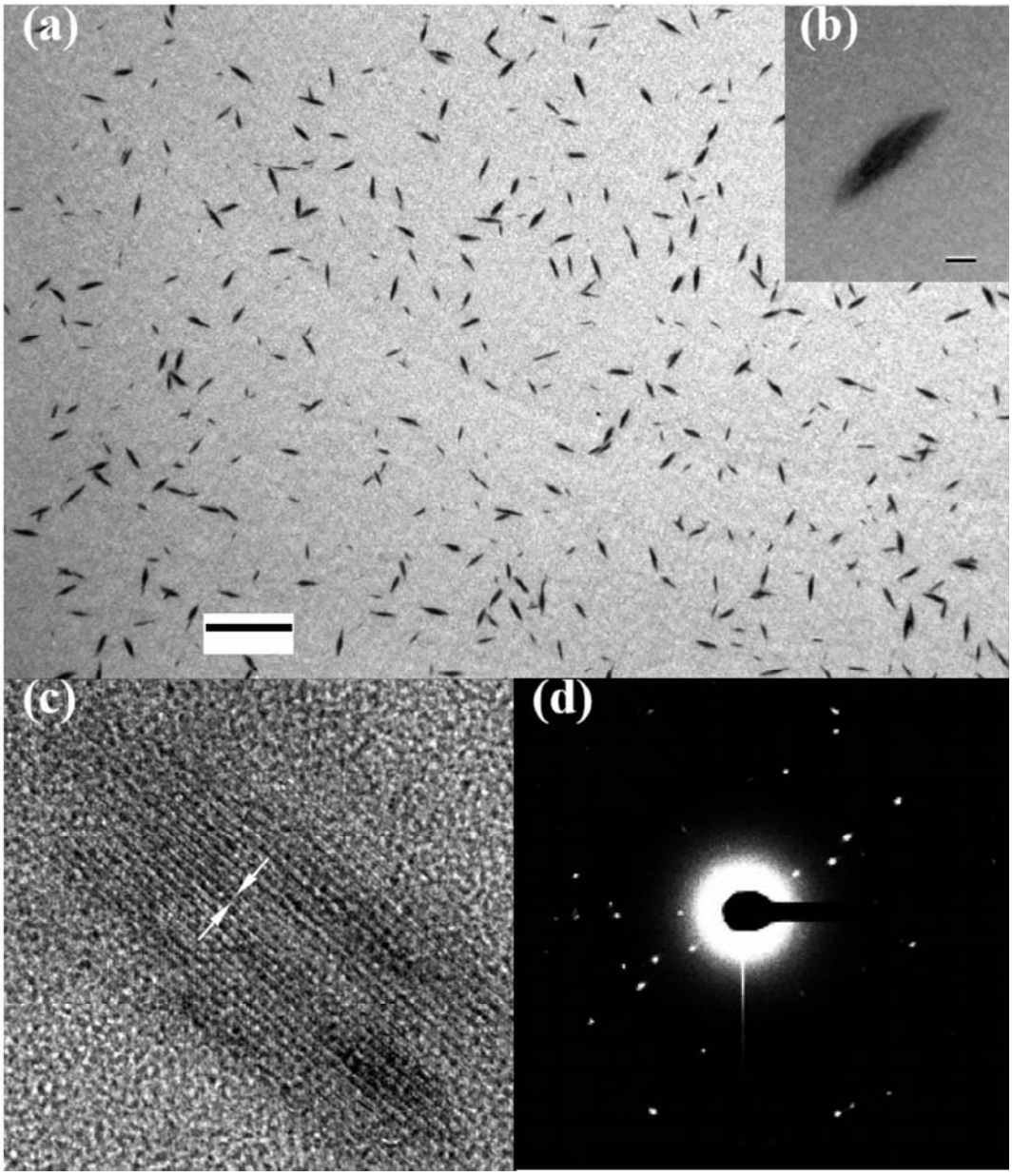

Figure 4.1 PEDOT nanocrystals. **(a)** TEM image; **(b)** Single nanoneedle image; **(c)** HRTEM; and **(d)** Electron diffraction. Scale bar=200nm in a, 20nm in **(b)** The arrows in **(c)** show the chain spacing distance of 0.6nm, which was confirmed by the electron diffraction results (*a*=0.584nm, in **Figure 4.4** and **Table 4.1**).

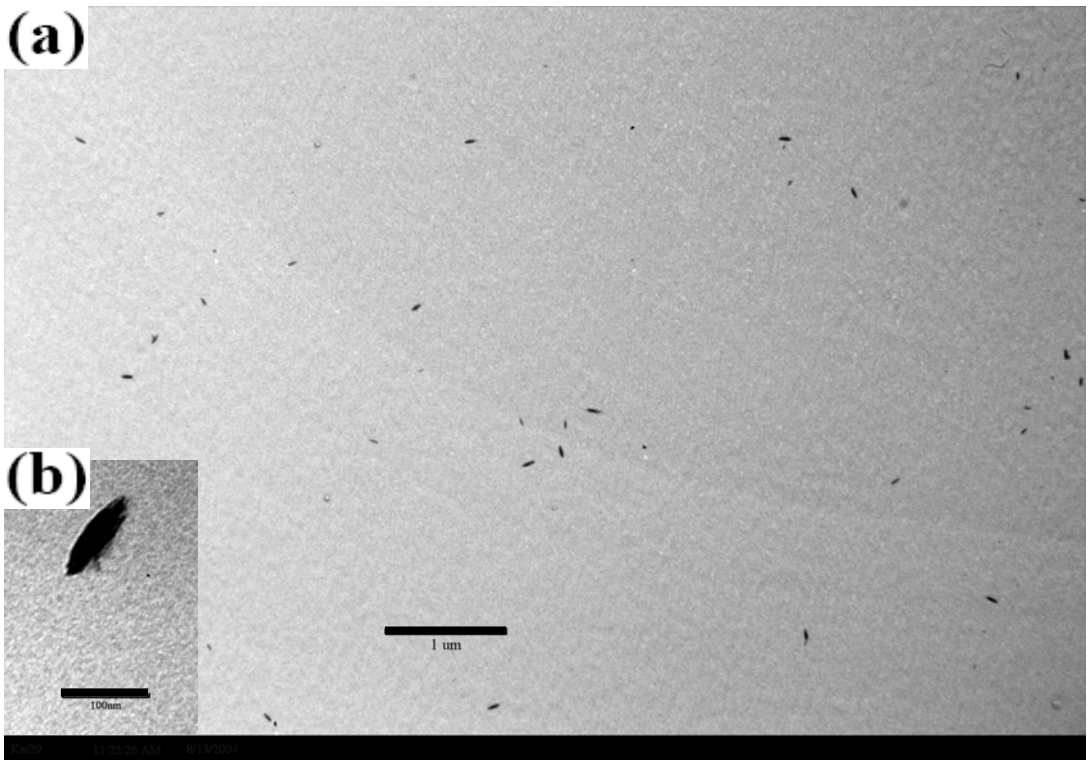

Figure 4.2 TEM images of PEDOT nanoneedles synthesized using pentane as the organic upper layer. Scale bar= **(a)**1μm, **(b)**100nm.

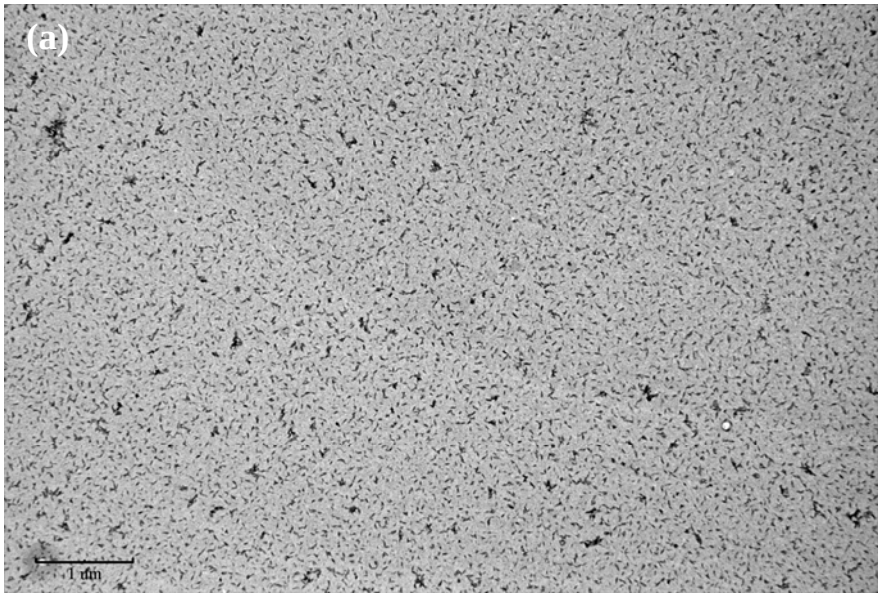

Figure 4.3 TEM images of PEDOT nanoneedles synthesized using n-butanol as the organic upper layer. Scale bar= **(a)**1μm, **(b)**100nm.

Although different lattice dimensions were obtained for PEDOT from different syntheses, the polymorphs can be assigned as an orthorhombic lattice.[30, 31] The lattice constants a, b, and c are designated as the lateral chain spacing, π-π stacking distance, and repeating unit length, respectively. High-resolution TEM (HRTEM, **Figure 4.1 (c)**) and electron diffraction (**Figure 4.1 (d)**) data (Tecnai G2 F20 cryoelectron microscope) from the same sample as used in the TEM indicate exceptionally high level of order and give further structural details of the nanoneedles. The HRTEM image (**Figure 4.1 (c)**) gives a vivid lattice structure of the nanoneedle. This lattice distance was assigned as the lateral chain spacing, *a*. The electron diffraction pattern (**Figure 4.1 (d)**) shows well-defined diffraction spots, indicating the nanoneedles as highly ordered single crystals. **Table 4.1** gives the calculated lattice distances from the electron diffraction spots. From these data, the lattice units were assigned as *a*=0.584nm (confirmed by HRTEM, **Figure 4.1 (c)**), *b*=0.494nm, and *c*=0.796nm.

The π-π stacking distance, *b*=0.494nm, is on the low end of the reported range of 0.425nm to 0.68nm.[28, 30, 31] The lateral chain spacing, *a*=0.584nm, is a very close distance when compared with the range of 1.3 to 1.5 nm reported values for PEDOT with external dopants of different sizes and concentrations.[30, 31] The contributing factors to this short π-π stacking and close lateral spacing include the expected favourable packing of the incoming monomers on the crystal template and the lack of high concentration large external dopants. Energy dispersive X-ray spectroscopy (SEM, Amray 1910, combined with a Noran system SIX, Thermo Electron Corporation, X-ray microanalysis system)(EDS) data (**Figure 4.5** and **Table 4.2**) supported a C/O/S ratio of 6/2/1 and on the average one Cl^- anion for 54 thiophene rings without observable iron. Since no external doping was applied, Cl^- anions served the role of charge compensation. The chains are likely composed of macroradical cations as well as neutral PEDOT depending on whether oxidation or deprotonation as the last step of chain growth.[24] Therefore the maximum *average* number of thiophene ring per PEDOT chain can be placed as 54, a number representing a low molecular weight polymer but larger than that of oligomers. With the present acidic environment of the polymerization system (pH = 2.45 in aqueous phase) and in the absence of proton acceptor in the media, a cation radical should represent most the charge state of the chains. Submicronic hematite needles were observed by aging $FeCl_3$ in NaH_2PO_4 buffer at 100^0C for 3 days.[32] For our organic nanoneedles, the electron paramagnetic resonance, EPR, spectrum (**Figure 4.6**) clearly shows the characteristics of PEDOT (linewidth ~3.9G, *g*-value ~2.0083) without observable hematite. The presence of hematite would be readily observable

as a very intense EPR signal at *g*-value ~2.04 with broad linewidth ~500G.[33]

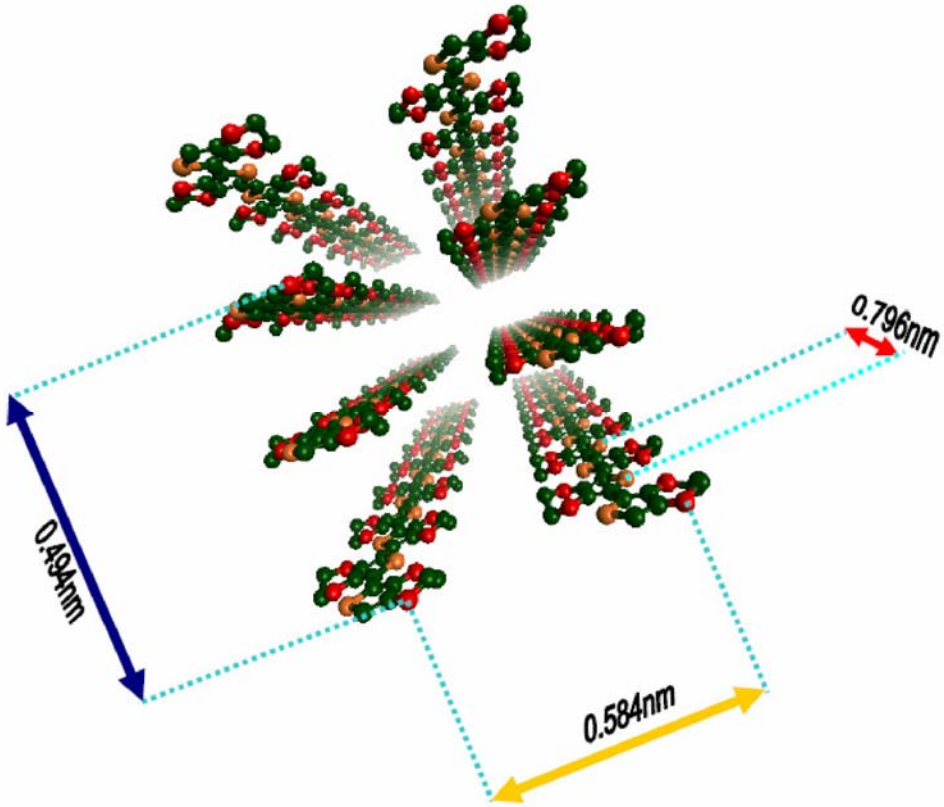

Figure 4.4 Schematic representation of chain arrangement for PEDOT nanoneedle with eight PEDOT segments, each with 15 monomer unit, representing partial chains. Not shown is one Cl^- anion, a charge compensator, for every 54 monomer units (S/Cl atomic ratio of 54 in EDS data in **Figure 4.5**). The chains are likely composed of macroradical cation as well as neutral PEDOT depending on the nature of the last step of propagation. As represented in the orthorhombic lattice units: lateral chain spacing *a*=0.584nm, π-π stacking distance *b*=0.494nm, and repeating unit distance *c*=0.796nm.

Table 4.1 Lattice assignment of diffraction pattern.

***d*(nm)**	**Indices**
0.796	001
0.584	100
0.494	010
0.427	-
0.398	002
0.344	-
0.292	200
0.265	003
0.231	020

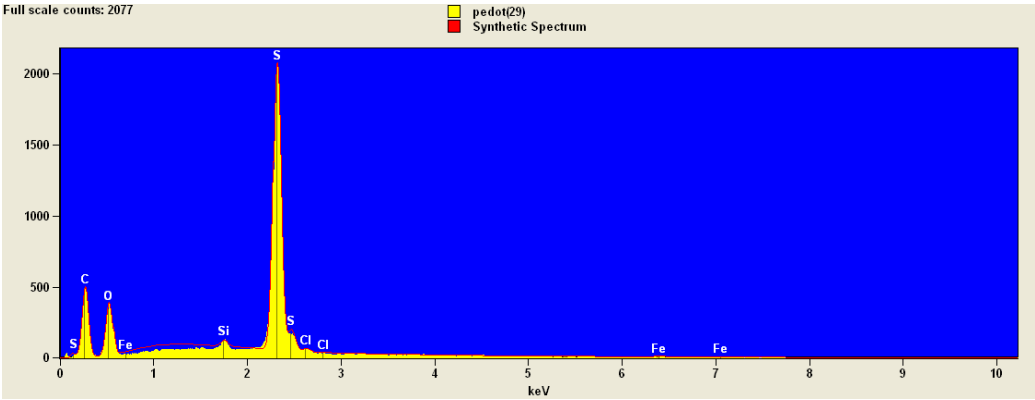

Figure 4.5 EDS spectrum for PEDOT from interfacial crystallization-polymerization. The purified PEDOT sample was deposited on a silicon wafer cleaned by using an UV-ozone cleaner followed by an ultrasonication in HPLC grade methanol. The quantitative result shows a C/O/S ratio of 66.5/21.2/11.8, supporting the theoretical atomic ratio of 6/2/1. The S/Cl atomic ratio of 54 indicates that every 54 monomer units share one Cl^- as a charge compensator.

Table 4.2 Quantitative Results.

Filter Fit Chi Squared: 1.116; Correction Method: ZAF; Acc.Voltage: 12.0 kV.

Element	*Net Counts*	*Weight %*	*Atom %*	*Compnd %*	*Norm. Compnd%*
C	4143	52.15	66.51	52.15	52.15
O	3271	22.14	21.19	22.14	22.14
Si	746	0.56	0.31	0.56	0.56
S	25291	24.64	11.77	24.64	24.64
S	0	---	---	---	---
Cl	380	0.51	0.22	0.51	0.51
Cl	0	---	---	---	---
Fe	54	---	---	---	---
Fe	0	0.00	0.00	0.00	0.00
Total		100.00	100.00	100.00	100.00

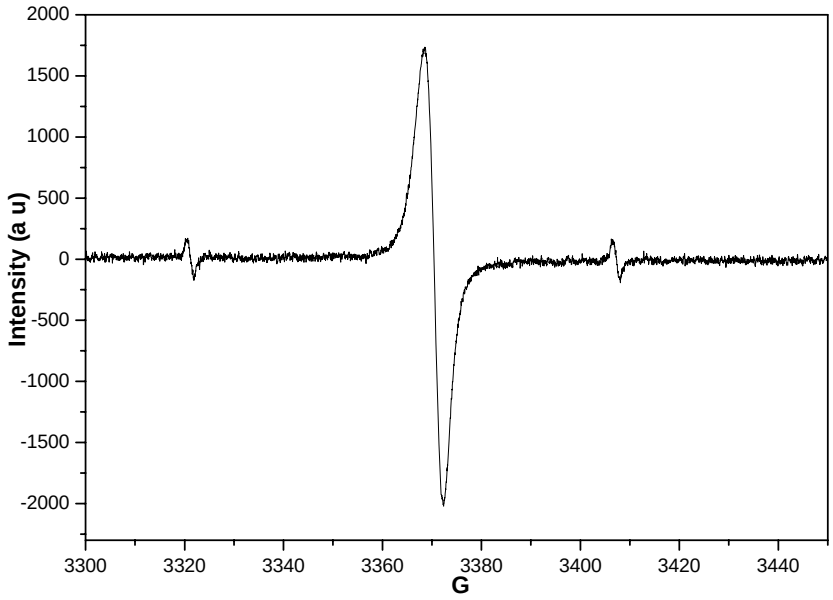

Figure 4.6 First-derivative EPR spectrum of PEDOT nanoneedle at room temperature (linewidth ~3.9G; g-value ~2.0083); with Mn^{2+} marker signals, 3rd and 4th line signals.

The analytical results from TEM, HRTEM, electron diffraction, EDS and EPR converge to support our first synthesis of single crystalline PEDOT nanoneedles with close π-π stacking and lateral separation. A schematic representation of the polymer chain arrangement with 15 monomer units per neutral segment in the nanoneedle is illustrated in **Figure 4.4**. Not shown is one Cl^- anion, a charge compensator, for every 54 monomer units (S/Cl atomic ratio = 54 from EDS data; **Figure 4.5**).

Because of their special morphology and unique crystalline structures including close π-π stacking and lateral distance, these nanoneedles showed novel electronic properties. Using scanning tunneling microscopy/spectroscopy (STM/STS), we studied their electronic conducting behaviour and discovered a field-induced conductance switching with response times in the millisecond scale.

The first reported conducting polymer switch was based on polyaniline nano-junctions electrochemically synthesized as the bridge between gold electrodes.[8] Abrupt switching behaviour was observed when the electrode gap narrowed to one nanometer. It was hypothesized that the abrupt switching is due to the formation of single crystalline domains, although the crystalline nature of the junction was not experimentally verified.

For PEDOT STM/STS studies, the purified suspension was 10-fold diluted with ultrapure water and spin-coated on a gold-111 surface. A representation of typical STM/STS results is shown in **Figure 4.7**. STM images were obtained for individual nanoneedles (**Figure 4.7 (b)**) followed by positioning the STM tip on the middle of a nanoneedle for STS at the completion of the scanning. The tunneling I-V curves, **Figure 4.7 (a)**, were recorded from -4 to 4 volts bias voltage range for both the

PEDOT needles and the gold substrate. The gold-111 surface, as a reference, showed a typical metallic tunneling I-V behaviour. Unlike the gold surface, PEDOT nanoneedles showed abrupt switching behaviours at about -3 and 3 volts. The conductance behaviour most likely involves the electron transport along the π-π stacking direction of the PEDOT nanoneedle. The plateau region from -3 to 3 volts can be assigned as *OFF* or insulating state (tunneling current < 0.04nA) of the switch. When the bias voltage increased to 3 volts, the tunneling current abruptly jumped to a saturated amplitude (tunneling current >10nA). The two regions beyond -3 and +3 volts are the *ON* or highly conducting state of the switch. The switching process was in the millisecond scale, which is comparable to that of molecular switches.[34] At low applied field (0-3 volts), the barrier was high enough to prevent the passage of tunneling current through PEDOT and the switching-off process took over. The reproducibility of the STS behaviour was established by the investigation on an ensemble of twelve individual nanoneedles (see, tunneling I-V curves, **Figure 4.8**; switch-off and switch-on bias voltages and their standard deviations, **Table 4.3**). This non-contact measurement on nanocrystals without external dopant differs inherently from the contact measurement on highly doped and charged conjugate bulk systems in that tunneling currents are being monitored in the present case.[16, 35]

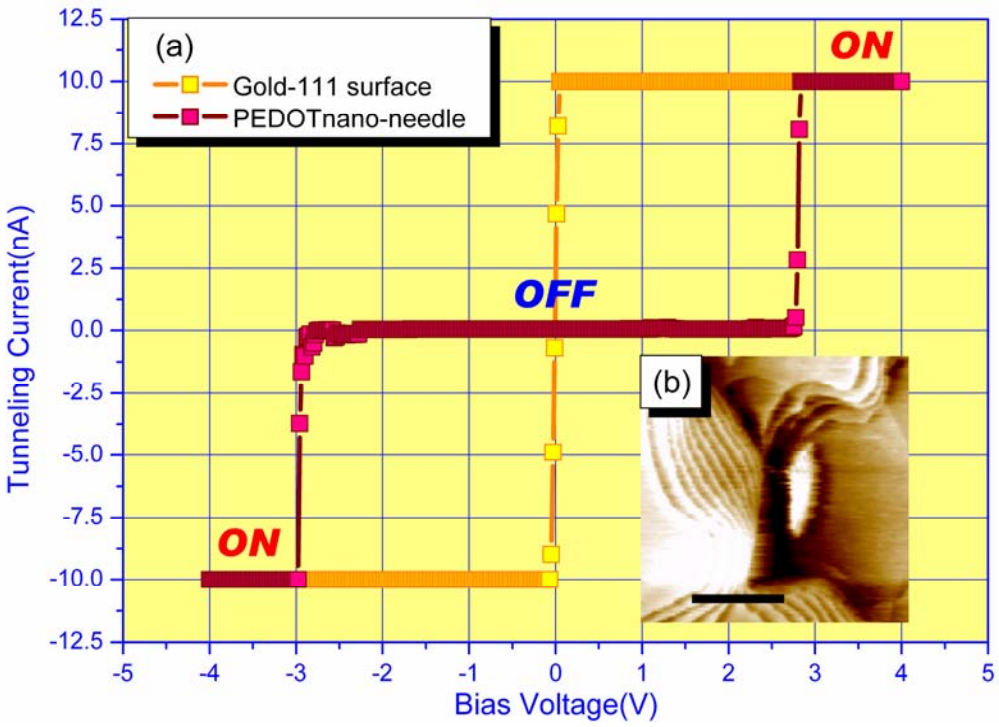

Figure 4.7 Representative switching behavior of the nanoneedle. a) The STS experiments were conducted on STM scanner (PicoSPM II, Molecular Imaging). The yellow square data points show a typical tunneling I-V curve of Gold-111. The red square data points show the tunneling I-V curve of a PEDOT nanoneedle. The plateau between -3 and +3 volts was assigned as the *OFF* (low conductance) state and the two regions beyond ±3 volts were assigned as the *ON* (high conductance) states. The sweep time for both the curves was 10 seconds. Two hundred data points were collected for each curve. The I-V measurement on a single needle can be repeated many times. The switching response was estimated to be in the millisecond time scale. STM experiments were conducted on the same instrument using a constant current (100pA) mode at a low servo level (servo gain %: I=0.3, P=0.1). b) A representative STM topological image was collected at the scanning rate of 0.5Hz, 8.5 minutes per frame. The bias voltage is 0.1 volts. The scale bar = 80nm.

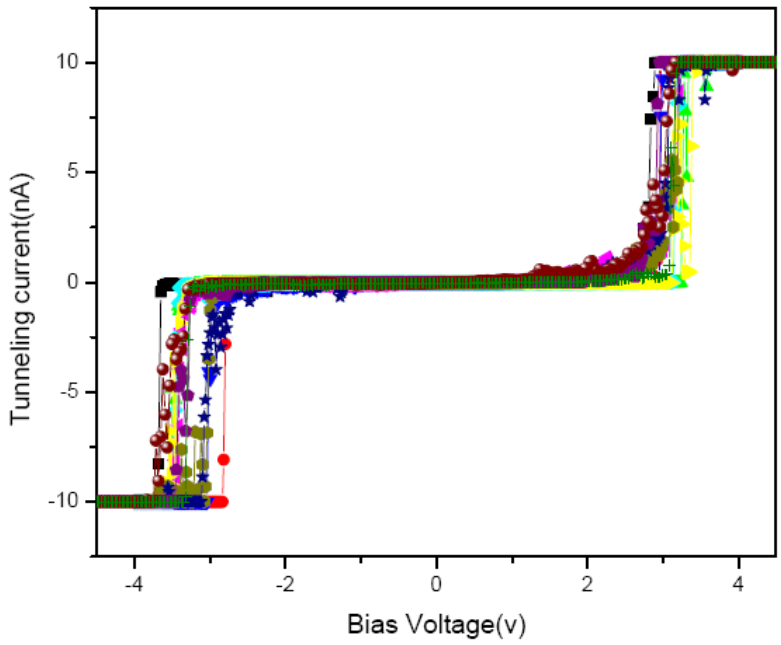

Figure 4.8 STS from twelve different nanoneedles. The Switch-on and Switch-off voltages and the standard deviations were tabulated in **Table 4.3**. Similar STS/STM results were also reproduced in DI's instrument (Veeco's Nanoscope IIIa, St. Barbara, CA). The parameters are the same as that used in MI's instrument. It should be noted that, in DI's instrument, the use of the instrument parameters stated in **Figure 4.7** is stipulated as "constant-height" mode because of the low servo gain setting.

Table 4.3 The Switch-on and Switch-off voltages and their standard deviations.

Curves	Switch-off voltage (v)	Switch-on voltage (v)
1	-3.28	3.11
2	-3.37	2.96
3	-3.34	2.86
4	-2.92	2.98
5	-3.01	3.03
6	-3.37	3.12
7	-3.32	2.94
8	-3.44	3.16
9	-2.95	2.96
10	-3.42	3.25
11	-3.66	2.77
12	-2.81	2.96
Average voltage(v)	-3.24	3.01
Standard deviation (v)	0.257	0.133

The PEDOT nanoneedles were observed to self-assemble to form organic sheets with uniform thickness. By a slow evaporation of water from the nanoneedle suspension, conducting polymer sheets with a thickness of around 15-20 μm were readily prepared. The overview SEM image (**Figure 4.9 (a)**) shows the morphology of the sheets and the thickness of the sheets are uniform as shown in a high-magnification SEM image (**Figure 4.9 (b)**).

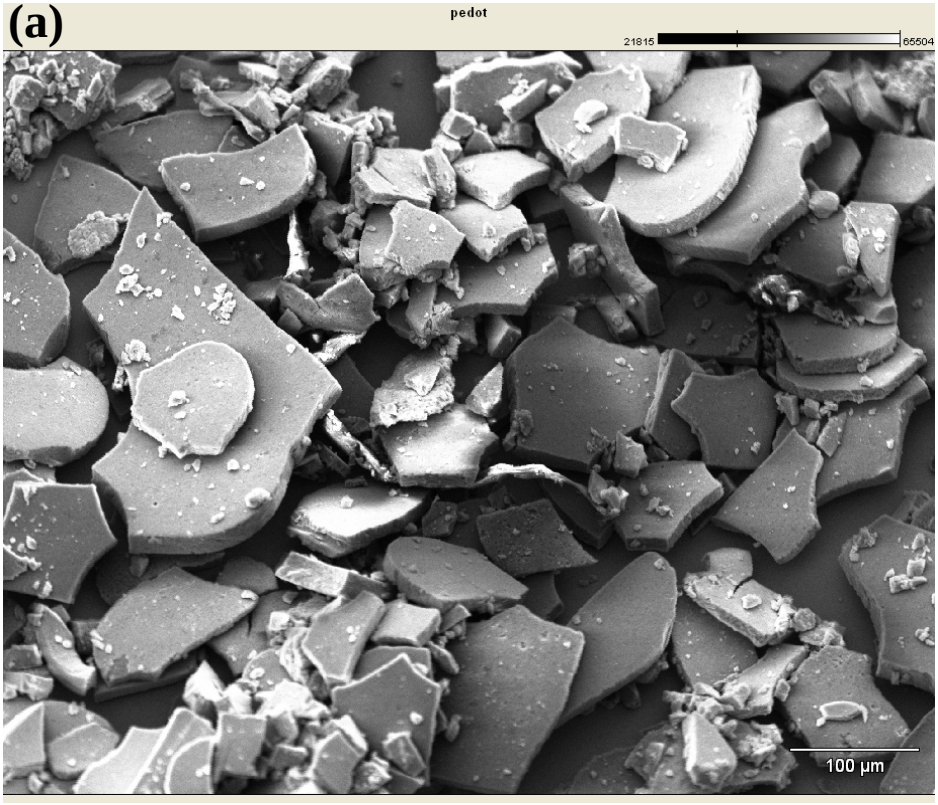
(a)
pedot
21815
65504
100 µm

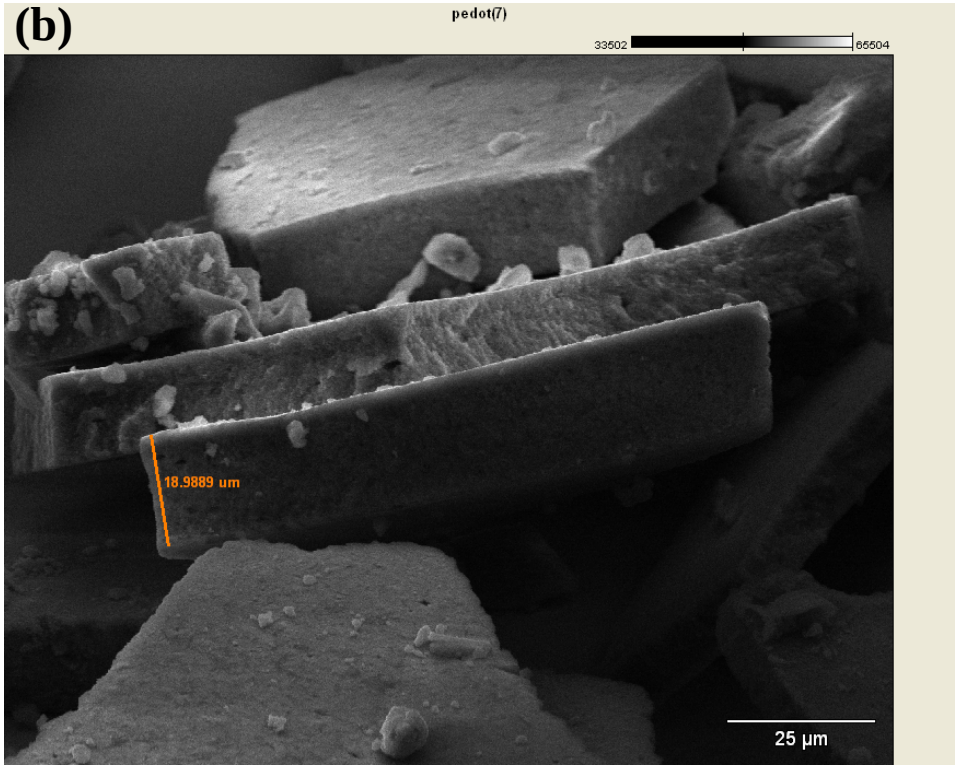
(b)
pedot(7)
33502
65504
18.9889 um
25 µm

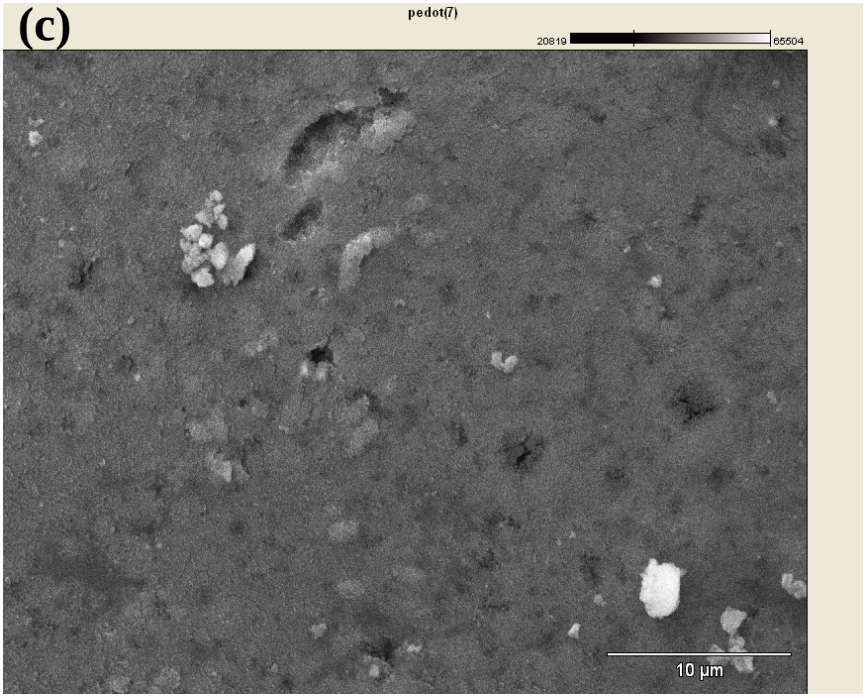

Figure 4.9 SEM images of self-assembled organic sheets from PEDOT nanoneedles. **(a)** Low-magnification image, **(b)** High-magnification image showing the thickness of the sheets, and **(c)** High-magnification image showing the flat surface of the organic sheet.

4.2.3 Conclusions

In summary, poly(3,4-ethylenedioxythiophene) (PEDOT) single crystalline nanoneedles with fast conductance switch properties were synthesized for the first time, using an interfacial polymerization process with attendant crystallization. The nanoneedles with pointed tips from this synthesis show average dimensions of 50nm length and 15nm width. Orthorhombic lattice units were assigned to the single nanocrystals with closer π-π stacking and lateral distances than most PEDOT systems. The absence of external large dopant and the crystallization during chain growth led to closely packed crystals, a condition contributing to conduction. These nanoneedles

show a novel switching behaviour with its response time in the milliseconds. PEDOT nanoneedles were also successfully obtained by using n-butanol and pentane as the organic layer for the interfacial polymerization. This interfacial route is also suitable for the fabrication of poly(3-hexylthiophene) nanoneedles. PEDOT nanoneedles can further self-assemble to organic sheet with uniformed thickness. The discovery of the new nanomaterial reported here can contribute to nanoelectronics in advancing fundamental understanding and developing novel organic nano-elements.

4.3 Application of the Interfacial Polymerization-Crystallization Process to the Syntheses of Single Crystalline Polyaniline and Polypyrrole Nanoneedles with Conductance Switch Behaviors

In Section 4.2, the first synthesis of single crystalline conducting polythiophenes (PEDOT and P3HT) with the fast conductance switching property using an interfacial polymerization-crystallization process was presented.[1] An important growth condition necessary to yield highly crystalline conducting polymers was optimal polymerization conditions accompanied by crystallization. Compared with other interfacial polymerization methods, lower concentrations of monomer and oxidant solutions were employed to further control the crystallization kinetics.[25] While other interfacial growth of conducting polymers yielded non-crystalline polymer fibers, as discussed in section 4.2, our interfacial method produced single crystalline PEDOT nanoneedles in the dimension of 15 nm x 50 nm. These nanocrystals displayed the conductance switching behavior between the insulating

and conducting states as potentials were applied, and the abrupt changes of the conductivity occurred at ±3.0V.[1]

In this section, we demonstrate the interfacial polymerization-crystallization technique can be successfully used to grow two additional important conducting polymers, polyaniline (PANI) and polypyrrole (PPY). This liquid/liquid interfacial method yielded uniform and needle-shaped conductive polymers of PANI and PPY after 48 hours and the resulting conducting polymers had the single crystalline structure with a fast conductivity switching behavior within milliseconds. This technique will provide a general route to synthesize conducting polymers via oxidative coupling processes in a single crystalline state, which is extremely difficult to achieve by other synthetic methods.

4.3.1 Experimentals

4.3.1.1 Materials and Apparatus

Pyrrole, aniline, ferric chloride, dichloromethane, and dialysis tubing were purchased from Aldrich Chemical Co.. Transmission electron microscopic (TEM) and High resolution transmission electron microscopic (HRTEM) studies were conducted on JEOL 1200 EX and Tecnai G2 F20 cryoelectron microscopes respectively; STM/STS studies followed the processes described in our previous contribution on both PicoSPM II (Agilent) and Nanoscope IIIa MultiMode (Veeco) microscopes for study and comparison.[1]

4.3.1.2 Synthesis of Nano-needle Shape Conducting Polymers

In a typical synthesis, aniline or pyrrole monomers were dissolved in dichloromethane (DCM, 5mL, 1mg/mL) to form the bottom organic layer and the oxidant, ferric chloride ($FeCl_3$), in deionized water (5mL, 0.1mg/mL) to form the upper water layer. After interfacial system was established, the aqueous layer was collected after 48 hrs. The purification processes of resulting polymer nanocrystals were described in the experimental part of Section 4.2.[1]

4.3.1.3 Ultraviolet-Visible Absorption

The purified conducting polymer nanoneedle suspensions were collected for the Ultraviolet-Visible (UV/Vis) absorption study on a Perkin Elmer Lambda 650 UV/VIS spectrometer. Equation 4.1 is employed for the energy conversion from the wavelength (nm) to the band gap (ev).

$$\text{Band gap (ev)} = 1243/\text{wavelength (nm)} \qquad (4.1)$$

4.3.2 Results and Discussions

The aqueous/organic interfacial system was composed of water and DCM. The monomers of PANI and PPY were in the organic solvent while an oxidant, ferric chloride, was in the water phase. The oxidative coupling polymerization of monomer was mediated at the aqueous/organic interface (**Scheme 4.4**). Comparing with the experimental condition to synthesize PANI fibers at the interface,[25] our coupling polymerization was controlled to be much slower by reducing the concentration of the oxidant to 0.1 mg/mL in order to obtain their single crystals. The TEM image (**Figure 4.10 (a)**) shows the nanoneedles of PANI with an average length and diameter of 63

nm and 12 nm. The average length and diameter of PPY are 70 nm and 20nm as shown in **Figure 4.11 (a)**. Single crystalline conducting polymers were first nucleated at the interface through oxidative coupling of PANI or PPY monomers from the organic layer facilitated by ferric chloride from the aqueous layer. These polymer nanocrystals were grown into the aqueous layer in the oriented direction and then they were dispersed into the aqueous layer in the nanoneedle form. The high resolution TEM images of both PANI and PPY showed resolution of their lattice fringes (**Figures 4.10 (b)** and **4.11 (b)**), and these images confirmed the single crystalline nature of the monodisperse nanoneedles.

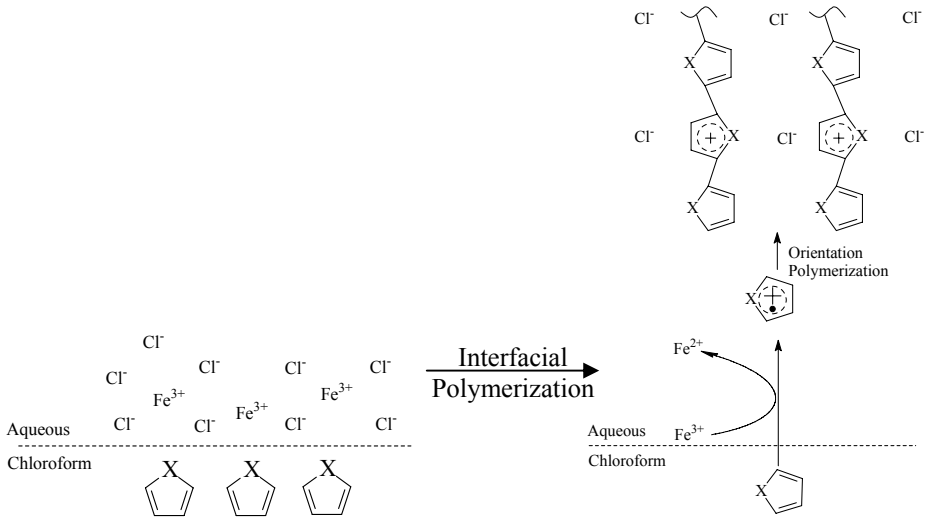

Scheme 4.4 Slow interfacial polymerization-crystallization through oil/water interface.

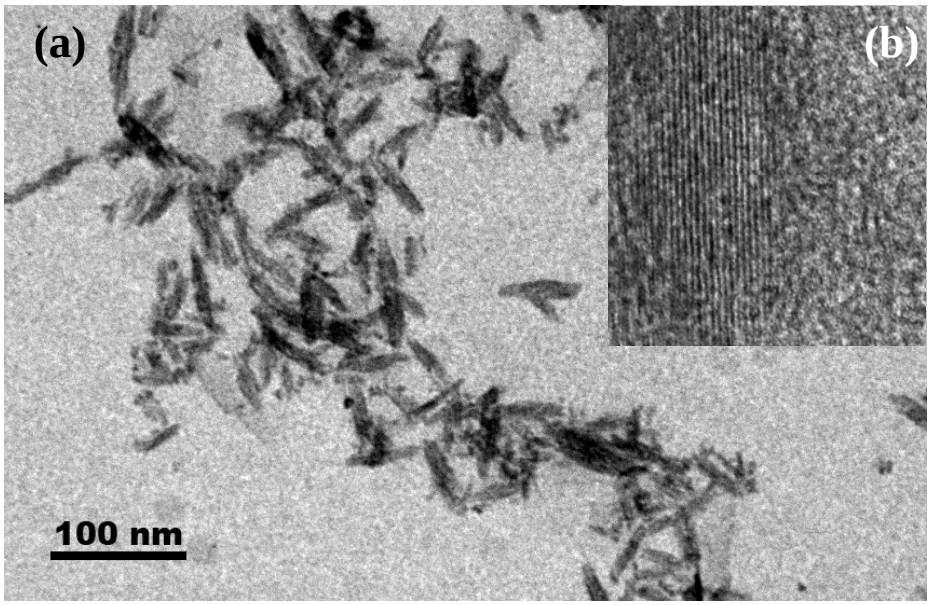

Figure 4.10 (a) TEM image of PANI nanoneedles; **(b)** HRTEM image of PANI.

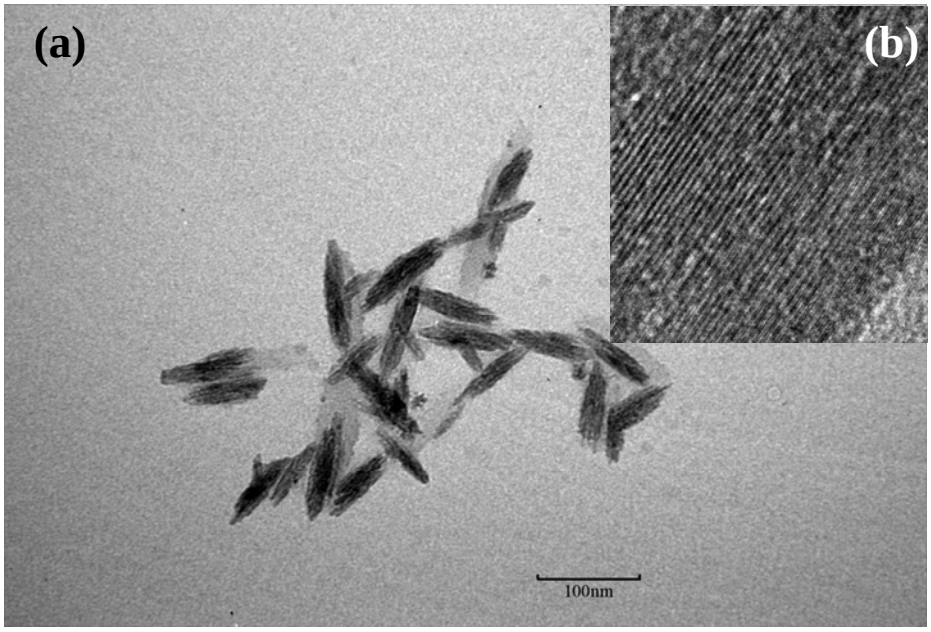

Figure 4.11 (a) TEM image of PPY nanoneedles; **(b)** HRTEM image of PPY

We hypothesize that those single crystalline conducting polymers are grown by similar interfacial polymerization-crystallization mechanism as in the polymerization

of EDOT (**Scheme 4.4**). Previously it was reported that when polymerization of PANI occurs in a two-phase matrix, these polymers grow in the non-crystalline fiber form at the interface and the polymerization terminates as polymers dispersed into aqueous phase due to hydrophilic nature of the polymer.[36] When concentrations higher than those mentioned in our experimental section were applied to polymerize PANI and PPY, the formation of amorphous nanofibers or granular particles were observed with fast growth kinetics, thus consistent with our mechanism. To grow polymers in single crystalline structure at the interface, the interfacial reaction needs to be slowed down significantly. We could achieve this condition by employing the low concentrations of the PANI/PPY monomer and the $FeCl_3$ oxidant. After attack by the oxidant, the monomers around the interfacial region were charged positively by losing electrons to Fe^{3+} ions. And then the counter ions, Cl^-, bind these positive charges and bridge the repeat units as shown in the right illustration of **Scheme 4.4**. Due to the hydrophilic nature of these primary species, the polymerization proceeds along the normal to the interface followed by further coupling reactions. In our method, those oriented polymers could be aligned between positively charged repeat units and negatively charged Cl ions during the slow interfacial reaction (**Scheme 4.4**) to form elongated needle-shaped crystals as shown in **Figures 4.10 (a)** and **4.11 (a)**. Polymerization with disordered monomer alignment is also suppressed when freshly formed nanoneedles diffuse away from the reactive interface.[36] Since fewer monomers are attacked by radical cations, the oxidative coupling reaction could be terminated in relatively short time scale, which also favors the formation of the shorter rice-shaped crystals rather than long fibers. The binding between the

monomer units and Cl^- ions was confirmed by the energy dispersive spectroscopy (EDS) (**Figure 4.12**). The ratio between the counter ion (Cl^-) and the monomer unit of PANI is 1:12 while the ratio for PPY is 1:20. The difference of the Cl^-/monomer ratio between PANI and PPY reflects the difference in their ability to accommodate positive charge, in consistence with the lower ionization potential of PANI.

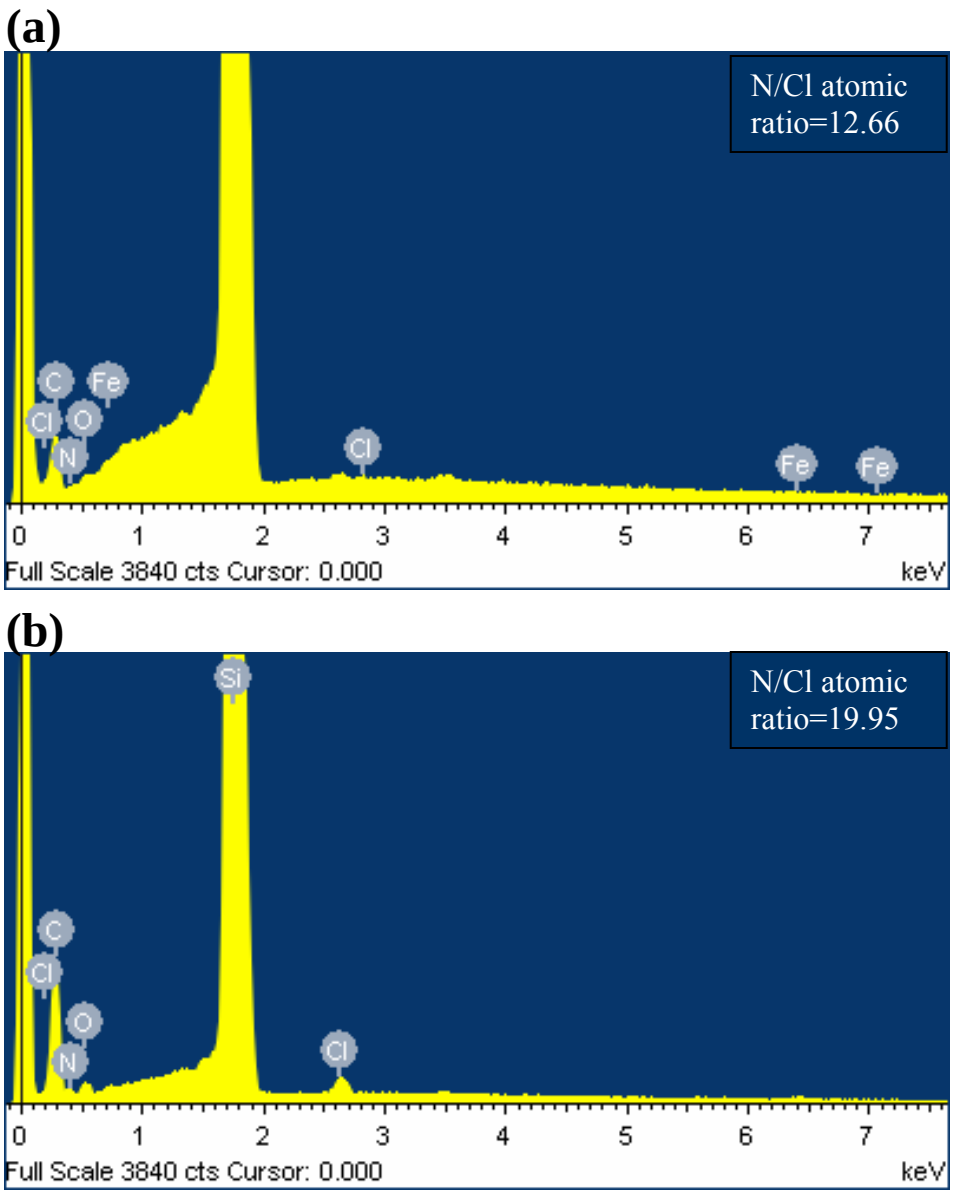

Figure 4.12 EDS spectra of polymer nanoneedles: **(a)** PANI; **(b)** PPY.

PANI and PPY nanoneedles also displayed interesting electronic properties due to their unique morphological and crystalline structure. We applied scanning tunneling spectroscopy (STS) to probe their electronic properties. In our STS studies for PANI and PPY nanoneedles, each suspension was collected from the upper aqueous layer and dialyzed for 10 hours in high-purity water (resistivity 18.2 MΩ cm, total organic carbon level 10 ppb) to remove impurities. The purified suspension was then 10-fold diluted with high-purity water and spin-coated onto a gold-111 substrate surface. The tunneling I-V curves were recorded from -6 to 6 V scale for these polymers between the STM tip and Au substrate. While the bare Au substrate showed a typical metallic tunneling I-V behavior, the abrupt switching behaviors were observed for PANI at ±3.5 V and PPY at ±4 V as shown in **Figure 4.13**. The PANI nanoneedles were insulated in the range of -3.5V ~ +3.5V, and in the case of PPY nanoneedles the "OFF" state is between -4.0 V and +4.0 V for PPY. Beyond these critical points, both PANI and PPY nanoneedles turned on the conducting state, and this switching process from the "OFF" to the "ON" states was in millisecond scale.

Since the voltage range of "OFF" state is larger in PPY than PANI in **Figure 4.13**, this comparison indicates that the band gap for PPY nanoneedles is larger than the one for PANI nanoneedles. This is consistent with UV/Vis absorption spectra of PANI and PPY, as shown in **Figure 4.14**. From those spectra, the PPY nanoneedle has the higher band gap (2.5eV) as compared to the PANI nanoneedles (2.21eV).

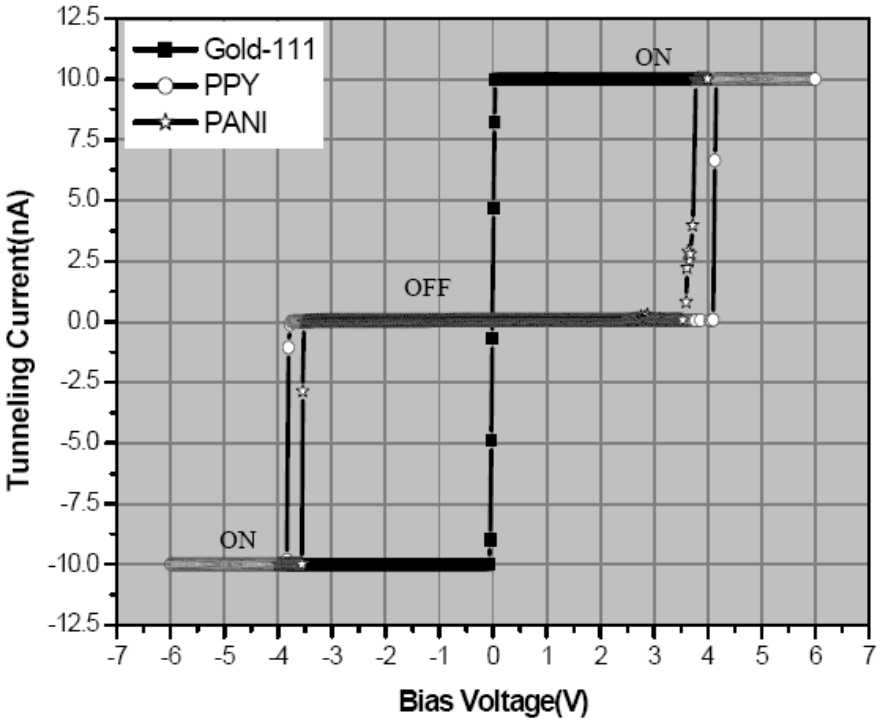

Figure 4.13 STS spectroscopy of conducting polymer nanoneedles and the gold-111 substrate surface.

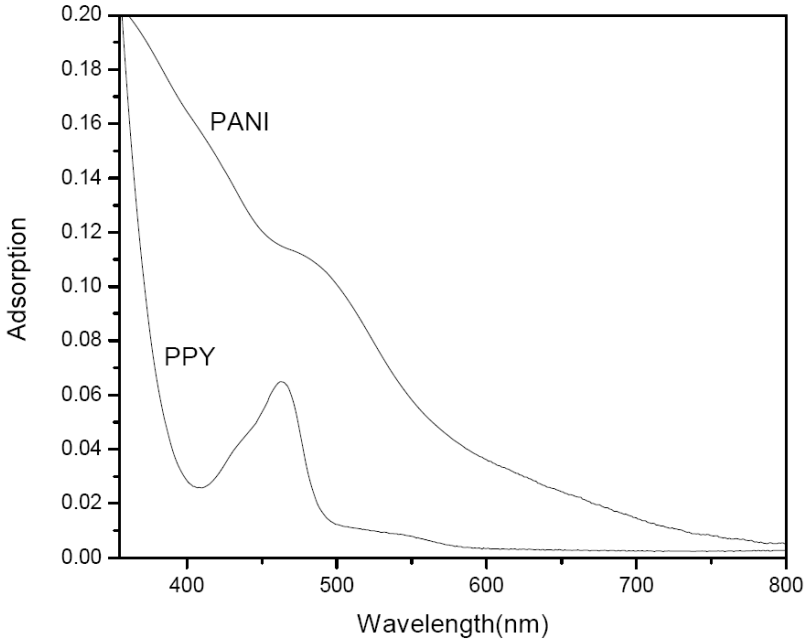

Figure 4.14 UV spectra of conducting polymer nanoneedles. Calculated bandgaps are 2.21 (PANI) and 2.50 (PPY) ev.

4.3.3 Conclusions

Single crystalline nanoneedles of PANI and PPY were synthesized using an interfacial polymerization-crystallization process. A slow crystallization kinetics at the liquid/liquid interface allowed PANI and PPY polymers to form single crystalline nanocrystals in the nanoneedle shape in the dimensions of 63 nm x 12 nm for PANI and 70nm x 20nm for PPY. The conductance switching properties of these crystalline polymers were observed in their I-V curves, and the conductance switching was fast in the time scale of milliseconds. Since this liquid/liquid interfacial synthesis method could be applied to synthesize PEDOT, PANI, and PPY conducting polymers in the single crystal state, this technique could be applied as the general fabrication process of single crystalline conducting polymers.

Chapter 5

One–Pot Synthesis of Strontium Titanate/Polyaniline Nano-composites and Their Electrorheological Effect[1]

5.1 Introduction

The field of electrorheological fluids (ERF) has a scientific and technological history lasting over a half century.[2] Their potential applications in numerous industrial areas have been extensively explored. However, a fully comprehensive theory for the subject is still being developed.[3, 4] With recent advances in nanoscience, particles on the nanometer scale for ER effect have emerged as potentially novel materials for nano-systems.[5-15] Core-shell nanospheres are of special interest. They include inorganic/organic composites with variations in core and shell materials. The recent discovery of giant electrorheological, GER, materials is based on nano-spheres with a urea shell encapsulating a barium titanyl oxalate core.[8] We report here nano-spheres with a semiconducting organic shell and a two-phase core consisting of highly polarizable strontium titanate (STO) nanoparticles embedded in conductive polyaniline (PANI). Thus, this system represents the first encapsulated ER nano-sphere with extensive interfacial interaction in the core due to atomic polarizable isolated domains embedded in an electronically polarizable continuous matrix. A diagram of the working mechanism of ER fluid is shown in **Scheme 5.1**.

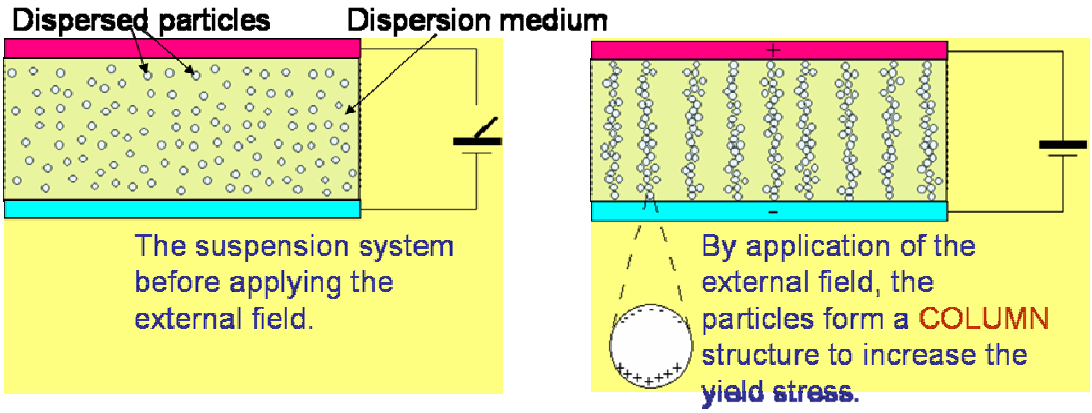

Scheme 5.1 Schematic working mechanism of ER fluids.

According to polarization theory, the ER effect, or microscopically the interaction between the dispersed particles, has an exponential relationship with the dielectric constant difference between the dispersed particle and the dispersion medium ε_p- ε_f (equation 5.1).[3, 16, 17] Thus, high-*K* inorganic ER materials have higher ER effect than organic ER materials. However, the drawbacks of inorganic materials, including high hardness and density, became an obstacle for their further applications. Electroresponsive polymers, providing electronic polarization to the ER system, possess advantages over inorganic ER materials because of their distinct properties, including fast response time, higher dispersion stability of the ERFs formulated from them, and low hardness, though their ER effect is not as high as that of high-*K* inorganic ER materials. Our design of inorganic/organic nano-composites combined the advantages from both components and an overall higher ER effect was expected. The interaction between the dispersed particles, *F*, depends on the external electrical field, E_0, to the second power and is a function of the dielectric constants of the dispersion medium (ε_f), of the dispersed particles (ε_p), and in vacuum (ε_0).[3]

$$F \propto \varepsilon_0 \varepsilon_f \left(\frac{\varepsilon_p - \varepsilon_f}{\varepsilon_p + 2\varepsilon_f} \right)^2 E_0^2 \tag{5.1}$$

, where F is the interaction between the dispersed particles, ε_f is the dielectric constant of the dispersion medium, ε_p is the dielectric constant of the dispersed particles, ε_0 is that of the vacuum, E_0 is the external electrical field.[3]

PANI, as core or shell, has been investigated for its ER effect under both DC and AC fields.[18] Both BTO and STO are of extensive interest because of their unusual dielectric properties. Most ER studies on composites have been on BTO systems. We focus on STO because its polarization can be induced and its non-polarized state is resumed on removing the applied DC field, while BTO in the tetragonal phase with an intrinsic dipole can be oriented by an applied field and the orientation remains after the removal of the external field. In addition, the PANI/STO interface can show interesting electronic properties.[19]

Our novel *One-pot* method to prepare strontium titanate/polyaniline (STO/PANI) nano-composites as ER materials does not require the usually obligatory high temperature sintering. The first step of the procedure is the synthesis of nanometer-sized STO nanocrystals using a reverse micelle method.[20] PANI was incorporated as the second component of the composite through a subsequent synthesis in the same reverse micelle system by oxidation polymerization. This efficient synthesis route ensured the two-step preparation of the final nano-composites in an *in-situ* manner and provided the entire synthesis in a micro-environment free from organic contaminants. Although various effective synthetic

routes have been developed recently, most of the methods for perovskite nanocrystals, including STO, need either high temperature,[21] high pressure,[22, 23] or inert environment.[22, 24] Most importantly, these methods are not suitable for the synthesis of STO/organic nanocomposites in an *in-situ* manner. Different from most of the previous STO synthesis, here pure nanocrystals were obtained at a reaction temperature of 80^{o}C under an open-bench condition. And the reverse micelle system can effectively be used for the synthesis of STO/PANI nanocomposite in a one-pot and *in-situ* manner. The structures and morphology of the STO nanocrystals and the STO/PANI nano-composites were characterized using XRD and TEM.

5.2 Experimentals

5.2.1 Materials

All reagents were purchased from Aldrich Chemical Co. and used without further purification.

5.2.2 Synthesis of Strontium Titanate Nanocrystals

All the syntheses were conducted at room temperature except the final oxide formation step. The crystals were prepared by a reverse micelle system using hydrochloric acid solution (47.09%) of $TiCl_4$ (6.39g) as the aqueous phase and cyclohexane (23g) as the oil continuous phase. Triton x-100 (30g) and n-butanol (28g) were selected as the emulsifier and co-emulsifier. The reactor was a 500ml flask, equipped with a stirrer, a thermometer, a dropping funnel and a reflux condenser. When the oil phase, aqueous phase, emulsifier and coemulsifier were add to the flask, a transparent reverse micelle system formed with a pale yellowish color.

With stirring, 40%NaOH aqueous solution was added dropwise into the flask until pH=7. Stoichiometric amount of $SrCl_2 \cdot 6H_2O$ was dissolved in de-ionized water (25ml) and then added into the flask dropwise under continuous stirring. 40% NaOH aqueous solution was further added dropwise into the colloidal system with a molar ratio of Ti^{4+}:Sr^{2+}:OH^- is 1:1:2. This reaction system was then heated to and kept at 78-80^oC for 3 hours prior to centrifugation at 5000rpm for 15min. The resulting sediment was redispersed in Chloroform/Methanol(1:1) using an ultrasonic bath and then centrifuged. This centrifugation-redispersion cycle was repeated 5 times in order to remove the excess emulsifier and other organic compounds. The resulting sediment was redispersed in de-ionized water to dissolve any soluble ion and then centrifuged at 5000rpm for 15min. This centrifugation-redispersion cycle was repeated 5 times. The final particles were dried at 80^oC in vacuo over night.

5.2.3 Synthesis of STO/PANI Nano-Composite by Reverse Micelles

The nano-composites were prepared in a One-pot manner as the second step in the same reverse micelle system after the synthesis of STO. Hydrochloric acid solution (2M) was then added dropwise to neutralize the water phase inside the reverse micelles. A solution of ammonium persulfate (3.52g) in 15.3mL 2M hydrochloric acid was then added into the flask. A solution of aniline (1.455g) in 7.66mL 2M hydrochloric acid was then added dropwise into the flask under cooling in an ice bath to produce the SrTiO3/PANI nano-composite. Stirring was continued for 4 hours after the addition of the aniline solution. The final colloidal system was collected and centrifuged at 4000rpm for 15min. The resulting sediment was redispersed in de-ionized water and ultrasonicated for 15min. This centrifugation-

redispersion cycle was repeated 3 times to remove the emulsifier and other soluble ions. The nano-composite appeared dark green in color. To reduce the surface doping level of the nano-composite, a de-doping process was conducted in an ammonia solution with pH=9 for 2 hours. The final products were then washed with de-dionized water until pH=7 and dried at 80^{o}C in vacuo overnight.

5.2.4 Preparation of The Electrorheological Fluids

The ER fluid was prepared by adding 30% weight of the final particles in 300cp silicone oil. The ER fluid was then ultrasonicated for 15 minutes before the ER testing.

5.2.5 Characterizations

The dried STO powders were characterized by X-ray diffraction (Philips X'pet diffractometer) for crystalline phase determination. The structure and morphology of the STO/PANI composite was studied on a TEM (Hitachi H800). A field-loaded coaxial cylinder type rheometer (HAKKE RV20 Rheometer) was used to investigate the ER effect of STO/PANI composites.

5.3 Results and Discussion

XRD of the STO nanocrystalline aggregate collected at the completion of the first step (**Figure 5.1)** shows sharp peaks with a level baseline, indicating a high order of crystallinity and purity. The lattice parameters are in complete agreement with those documented (JCPDS#35-734). Two factors can contribute to the facile low-temperature synthesis of pure STO nanocrystals: (1) only inorganic compounds in the absence of organic capping agents were used as the precursors. Although coordinated

metal precursors showed good results for the synthesis of perovskite type nanocrystals,[22, 25-27] the capping reagents may remain in the final product. The absence of organic capping agents and other impurities allow us to circumvent the process of sintering process for their removal; (2) The nature of the reverse micelle method provided a well-isolated micro-reactor for the synthesis.[20] With the protection of the emulsifier, the initial reactants remained inside and added reagents diffused into the micelle water pool to complete all reactions. This protected environment made it possible to prepare pure STO nanocrystals with high uniformity. Other perovskite type metal oxides, such as barium titanate, previously prepared involving high temperature sintering, can also be synthesized by reverse micelle methods similar to our system. **Equation 5.2** gives the reaction mechanism as a four-step process. In the reaction mechanism, the formation of $[Ti(OH)_6]^{2-}$ is very important for the formation of $SrTiO_3$ crystals. And the molar ratio of $Ti:OH^-$ is 1:2 in the second and third steps. The mechanism was established by the XRD analysis of the resulting STO nanocrystals from different $Ti:OH^-$ molar ratios (**Figure 5.2**).

$$
\begin{aligned}
&TiCl_4+HCl+5OH^- \longrightarrow Ti(OH)_4\downarrow +5Cl^-+H_2O \\
&Ti(OH)_4\cdot(H_2O)_2+OH^- \rightleftharpoons [Ti(OH)_5\cdot(H_2O)]^-+H_2O \\
&[Ti(OH)_5\cdot H_2O]^-+OH^- \longrightarrow [Ti(OH)_6]^{2-}+H_2O \\
&[Ti(OH)_6]^{2-}+Sr^{2+} \longrightarrow SrTiO_3\downarrow +3H_2O
\end{aligned}
\qquad (5.2)
$$

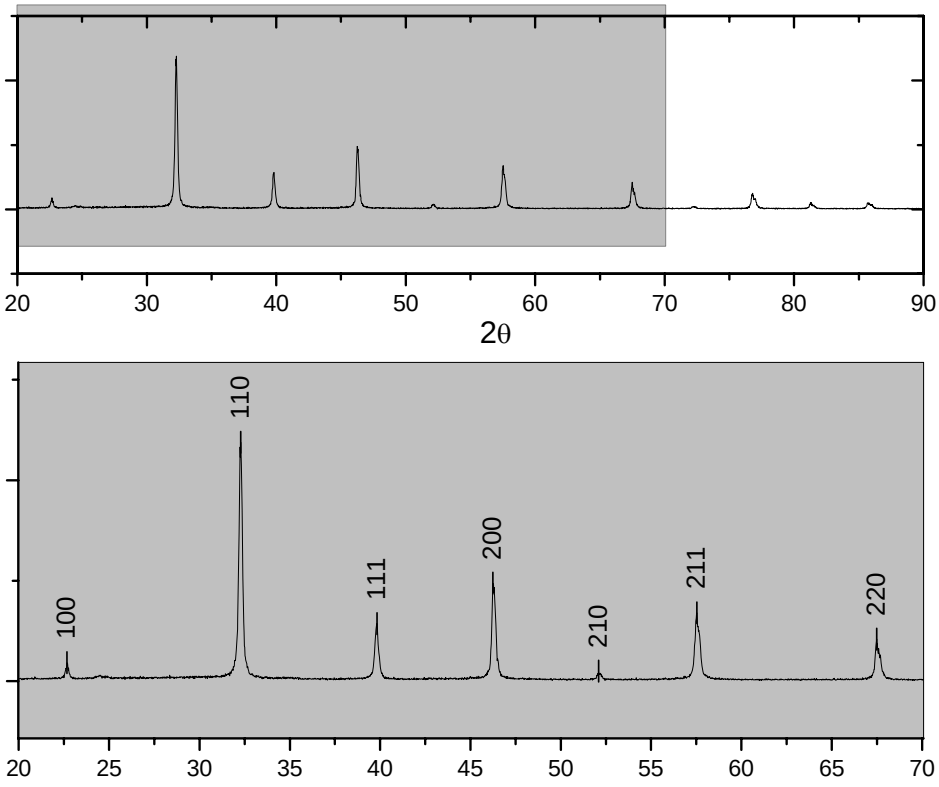

Figure 5.1 XRD pattern of $SrTiO_3$ nanocrystals.

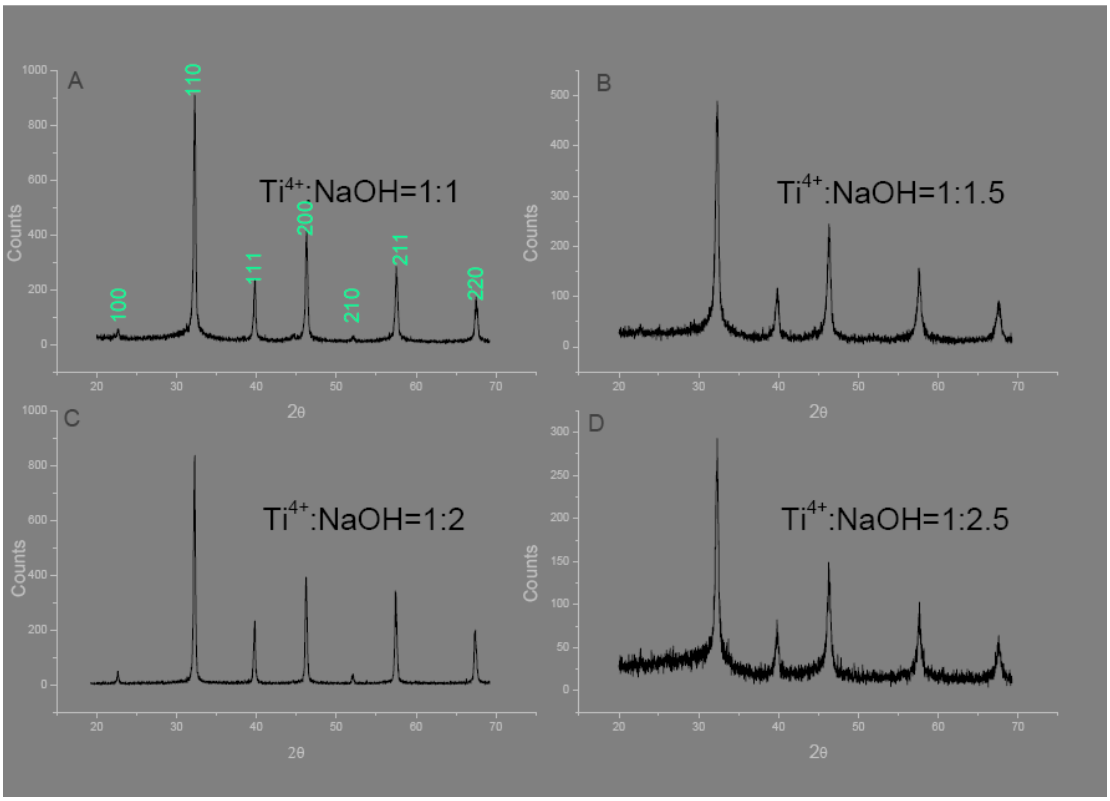

Figure 5.2 XRD analytical results for STO nanocrystals from different $Ti:OH^-$ molar ratios.

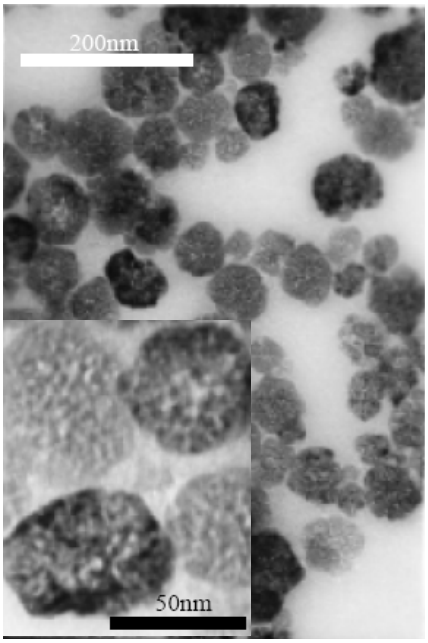

Figure 5.3 TEM images of STO/PANI nanocomposites.

The oxidation polymerization of aniline with HCl solution as both the acidic medium and the dopant followed the STO synthesis. The aniline was added to the micelle in a weight ratio of STO:aniline of 2:1. TEM (**Figure 5.3**) of the resulting composite shows an unusual morphology. The nano-composites were in spherical form smaller than 100nm with a few large ones on the order of 180nm.They are composed of 5nm STO nanocrystals embedded in PANI matrix. The size distribution of the nano-composite spheres showed excellent uniformity. The enlarged TEM picture (inset of **Figure 5.3**) shows dark nanocrystals (STO) embedded in the PANI matrix in lighter color. This stuffed sphere nanostructure for STO/PANI composite has not been reported before.

Nanocrystals of paraelectric STO are dispersed in a conductive PANI sphere with de-doped shell. The optimization of the de-doping process has been published in our previous study for PANI ER materials,[28] although it's difficult to distinguish the morphology and thickness of the de-doped PANI shell from the doped PANI core in the TEM image (**Figure 5.3**). The STO provides atomic polarization; the PANI inner matrix, electronic polarization; the low conductivity shell, protection against charge leakage. The conductance of PANI can be readily tuned for any desired local electric field. Due to their paraelectric nature, cubic STO crystals can be polarized equally in all six coordinates, rotation time for the sphere to optimize the sum of the dipole for the nano-sphere is not a significant parameter. Under the external DC electric field, the composite ER effect mainly originates from the atomic polarizations due to the off-center displacement of Ti^{4+} in strontium titanate as well as from electronic polarization from the conjugated polymer PANI. In addition, the interfacial

polarization due to the STO/PANI interface can be important because of their nanoparticle-to-matrix large contact area. As a conducting polymer, the conductance of PANI can be adjusted by the doping process. In the oxidation polymerization, PANI component was proton-doped. Using our previous results of PANI ER materials as a reference, the shell of the nano-composite sphere was de-doped by an ammonia solution at an optimum pH of 9 to give a level of low electronic conduction to prevent current leakage and yet allows for surface polarization.[29] As with ER materials, this nano-composites with STO embedded in PANI should potentially show unusual characteristics: (1) the induced dipoles have fixed position in the solid matrix of PANI, preventing the formation of dipole pairs; (2) the nano-composite, having atomic polarizable nanocrystals embedded in a matrix with electronic polarization may lead to a synergistic ER effect; (3) the composition of the nano-composite can be varied to achieve the optimal effect; (4) the surface de-doping not only prevents the current leakage between the spheres but also provides a level of interfacial polarization at the nano-sphere/dispersion medium interface. In addition, the electronic polarization of inner PANI matrix with relatively high conductance can provide additional local polarization field for the STO paraelectric nanocrystals.

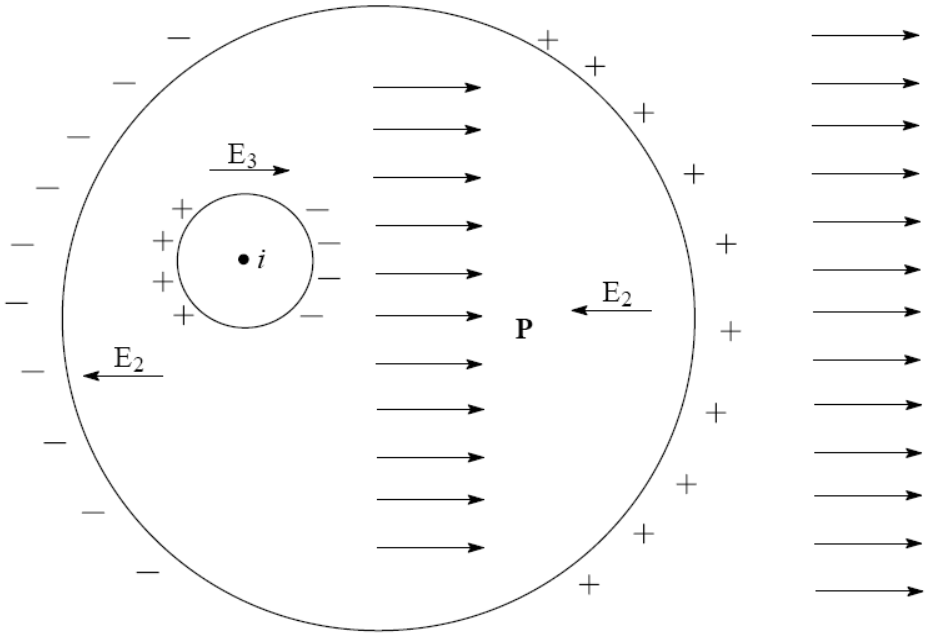

Figure 5.4 Local field model with a microscopic fictitious spherical cavity. Fields acting on a dipole consists of the external applied field, E_0, and the internal field contributed by dipoles themselves, E_1, E_2, and E_3.

Figure 5.4 shows the local field acting on a dipole. The local polarization of our core-shell nano-composites consists of an induction from both the external field and internal fields by the dipoles themselves. E_1 and E_2 are fields due to dipoles inside the fictitious cavity and surface charge induced on the surface of the specimen, respectively. Of particular interest for our system is E_3, the Lorentz Field associated with electronically polarizable PANI medium. Bulk composites of perovskite ceramic with PANI have been reported before.[11] The ER effect of the superfine powder of PANI/barium titanate composite with unknown morphology was shown to be much higher than either barium titanate (BTO) or PANI alone. Our nano-composite was then dispersed in silicone oil for ER studies. A very strong and stable ER effect was observed for the ER fluid by a DC field-loaded coaxial cylinder type rheometer.

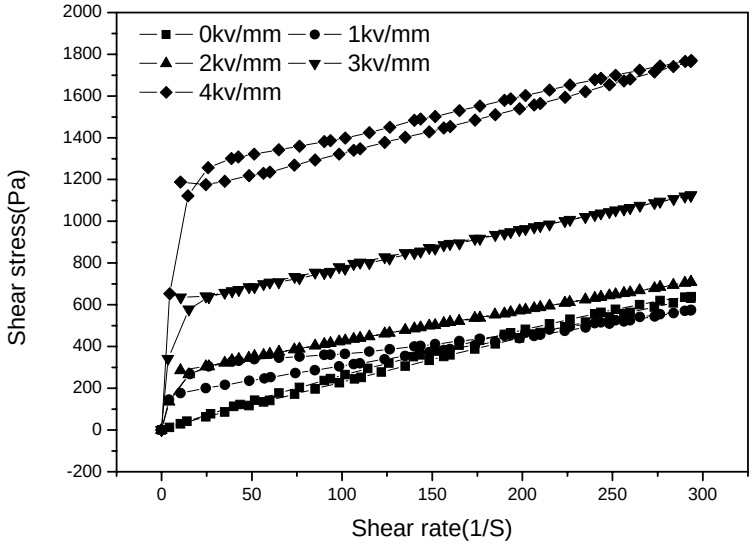

Figure 5.5 ER effect of the $SrTiO_3$/PANI-silicone oil under DC field.

Figure 5.5 depicts the ER effect of the nano-composites. The experiments were conducted in the direction of increasing shear rate followed by a decrease in shear rate under a different external DC field for the observation of shear stress. The shear stress vs. shear rate curves show superimposed curves for both directions with smooth linear feature beyond yield stress, indicating excellent suspension and electric stabilities for the ER fluid, important behavior for the application of ER fluids (**Figure 5.5**). No drop-down or fluctuation was observed in the plot at high electric field (4kV/mm). The yield stresses increased with the increasing of electric field as expected. These nano-composites showed as high as 1300Pa yield stress and 1800Pa shear stress at 4kv/mm field.

STO and PANI nanoparticles were individually synthesized by using the same reverse micelle process. A comparison of the ER effects of the STO/PANI nano-composite, PANI, and STO was made at 3kv/mm where the yield stress for the composite is 580Pa; STO, 330Pa; PANI, 190Pa. The STO/PANI nano-composite,

with a 2:1 weight ratio of STO:PANI, has double the ER effect of the sum of the weighted contribution from STO and PANI, i.e., a synergistic effect was clearly observed (**Figure 5.6**).

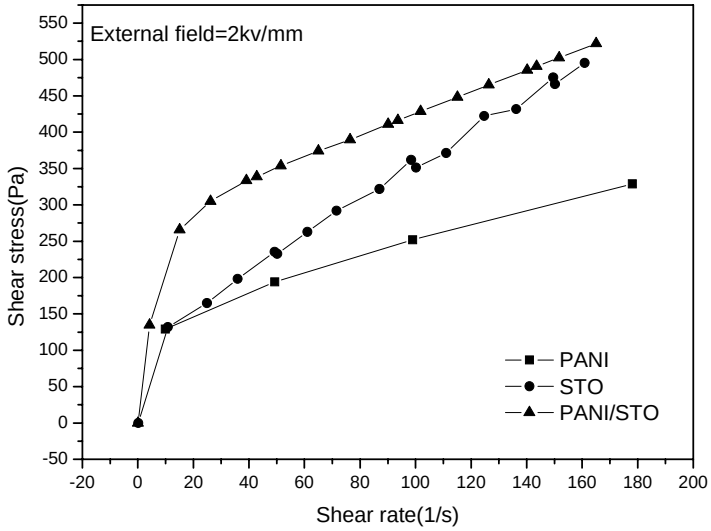

(a) Bingham model

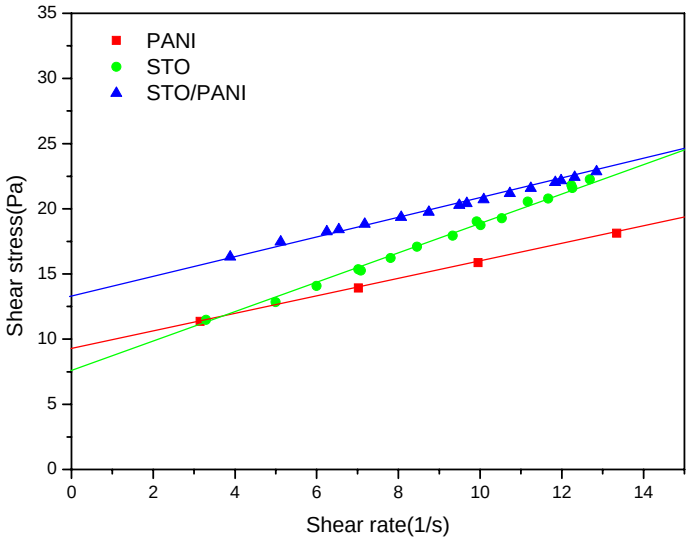

(b) Casson model

Figure 5.6 Comparison of the ER effects.

The shear-stress-shear-rate relationship is usually characterized as a Bingham behavior. In an ideal Bingham behavior, there is a yield stress at an infinitely small shear rate. For most of the ER fluids, the flow behavior does not show an abrupt change at the infinitely small shear rate under the electric field. Bingham behavior can be described in the following equation:

$$\tau(E,r,\dot{r}) = \eta(E)\cdot\dot{\gamma} + \tau_y(E) \tag{5.3}$$

, where τ is the shear stress, τ_y is the yield stress, η is the viscosity and $\dot{\gamma}$ is the shear rate.

To more effectively describe the flow behavior, we present the Casson model for the nano-composites. The Casson model is well known for describing the flow behavior of blood and chocolate.[30] This model is suitable for describing flow behaviors with nonlinear yield-stress-pseudoplastic nature, which can be observed in the stress-strain behavior in **Figure 5.6**. Casson model can be described as:

$$\tau^{\frac{1}{2}}(E,r,\dot{r}) = \eta_{PL}^{\frac{1}{2}}(E)\cdot\dot{\gamma}^{\frac{1}{2}} + \tau_y^{\frac{1}{2}}(E) \tag{5.4}$$

, where τ is the shear stress, τ_y is the yield stress, η_{PL} is so called "plastic viscosity" and $\dot{\gamma}$ is the shear rate. Using the Casson model, we re-depicted the ER effect in **Figure 5.7**.

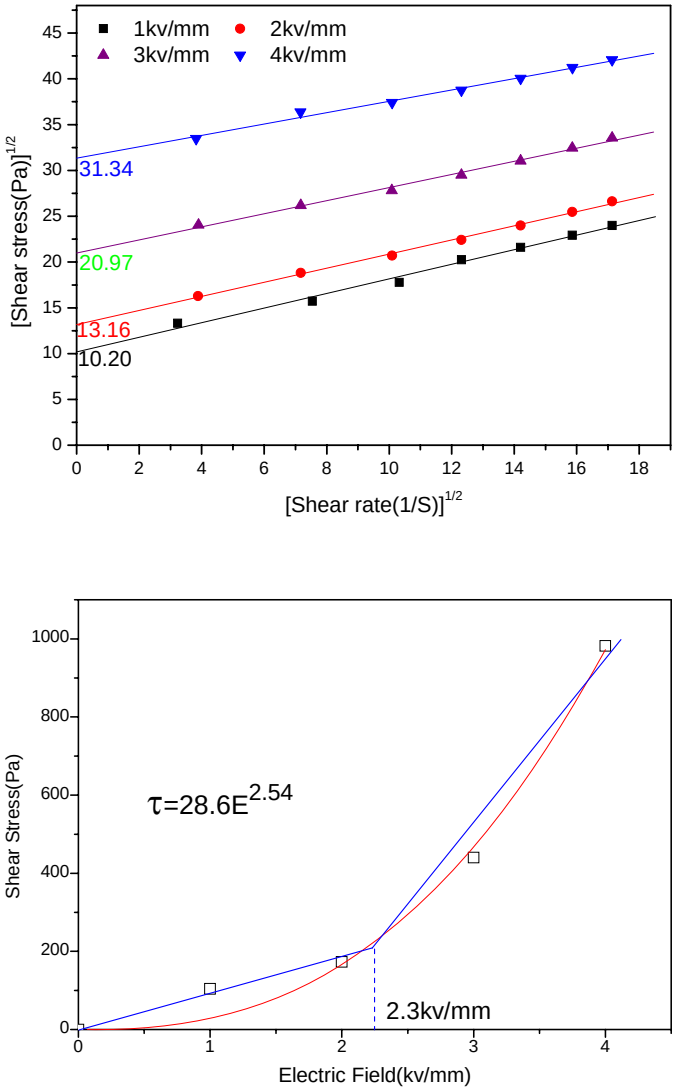

Figure 5.7 The relationship of $\tau^{0.5} \sim \dot{\gamma}^{0.5}$.

Figure 5.7 shows an excellent linear relationship between $\tau^{0.5}$ and $\dot{\gamma}^{0.5}$, which indicates the effectiveness of Casson model to describe the flow behavior. Although this is the first time using Casson model to describe the flow behavior of our current ER fluids, some previous results can also be fitted into this model very well (**Figure 5.6 (b)**). It's important to introduce the Casson model to replace the Bingham model

because the behavior under DC and AC fields are different. Under AC, the direction of the electric field varies so the local field direction varies. Faster polarizations can catch the changes but the slower ones can not. On the other hand, DC field gives enough relaxation time for all the polarizations. That's the reason why the same ER material shows higher ER effect under DC than under AC. Also, the current leakage and electric breakthrough can occur much easier under DC. All these differences give totally different ER behaviors for DC and AC even for the same ER material. For AC, most of the ER behavior can fit the Bingham model. But in DC, nonlinear behavior was observed by using Bingham model. However, it fit the Casson model well and shows linear behavior. The reason for the nonlinearity in the Bingham model is that the fluid is not only Bingham but also pseudoplastic. The Casson model works because the model is designed for the combination of Bingham and pseudoplastic behaviors.

In addition, in the Casson model (**Figure 5.7**), one can observe that the slope of the lines are similar, which indicates that the plastic viscosities, η_{PL}, are similar. This observation suggests that the influence of the external electric field is mainly on the yield stress but not the plastic viscosity. The bottom plot in **Figure 5.7** gives the relationship between the yield stress and the external filed. It shows that there is a critical external field, 2.3kv/mm. As shown in the blue lines, the relationship is linear below 2.3kv/mm. Above 2.3kv/mm, it can be fitted by a polynomial giving the relationship of $\tau_y \infty \dot{\gamma}^{2.54}$.

5.4 Conclusions

A novel STO/PANI nanocomposite ER material with a stuffed-sphere morphology was prepared via a reverse micelle system in a one-pot, open-bench synthesis. The nano-composite spheres with semiconducting shell and strontium titanate embedded in polyaniline core showed very stable and strong ER effect. A synergistic ER effect was observed due to the combination of atomic polarizable nanocrystals embedded in a matrix with electronic polarization. The Lorentz Field (E_3, **Figure 5.4**) associated with electronically polarizable PANI medium is likely to play a significant role. The Casson model was employed to give a more appropriate description of the ER behavior of the STO/PANI nanocomposites.

Chapter 6

Conclusions and Perspectives

Nanoelectronics has been emerging in recent years as one of the most exciting scientific explorations. This dissertation reports our discoveries on organic nanoswitches with fast response time, inorganic high-*K* nanocrystals for supercapacitor and FeRAM, and nanocomposites with novel morphology for electromechanics. These findings are based on the exploitation of surface physicochemical principles. A polymerization-crystallization system mediated by an interfacial region was used to prepare the first organic polymer single crystalline nanoneedles. A self-assembly of bolaamphiphilic nano-doughnuts with unique cavity surface properties was applied as templates to fabricate at room temperature ferroelectric barium titanate nanocrystals (6 to 12 nm). The approach of using reverse micelles as nanoreactors to control local reaction volume and kinetics resulted in the first open-bench synthesis of high-quality STO, BTO nanocrystals and BST nano-solid-solutions as well as nano-sphere composites with an insulating shell and high-*K* inorganics embedded in an organic conductor. The size of the nano-single-crystals can be controlled from 80nm to less than 10nm. Our $Ba_{0.7}Sr_{0.3}TiO_3$ nanocrystals with a giant dielectric constant ($1.4X10^5$) are of particularly significant technological applications to ferroelectric memories, FeRAM.

We demonstrated the versatility and significance of systems involving surface of two simple liquids for the preparation of important elements for nanoelectronics. Our laboratory is currently in the process of investigating more complex interfaces

from water/ionic liquid micelles. Preliminary results showed the success of synthesis of conducting polymer nano-hollow-spheres, potential vehicles for controlled release.

A new synthetic methodology based on self-assembly of bolaamphiphilic nano-doughnuts as templates was proposed to fabricate ferroelectric barium titanate nanocrystals, from 6 to 12 nm, at room temperature. Prospectively, this synthetic method using peptide nano-doughnuts may have a broad impact in the growth of various important crystals that do not grow at room temperature and ambient pressure. Recent examples include a similar approach for the synthesis of gallium oxide nanostructures.[1] The advancement of this novel approach will continue to provide more important nanoelements with different functions.

Bibliography

Chapter One

1. Feynman, R. P., There's Plenty of Room at the Bottom. *American Physical Society Meeting, Pasadena, CA, 29 Dec. 1959; American Physical Society Meeting, Pasadena, CA, 29 Dec. 1959; originally published in Caltech's Engineering and Science magazine, Feb. 1960; reprinted as R.P. Feynman, "Infinitesimal Machinery," J. Microelectromech. Syst.* **1992,** 1, 60-66.

2. Piner, R. D.; Zhu, J.; Xu, F.; Hong, S.; Mirkin, C. A., "Dip-Pen" Nanolithography. *Science* **1999,** 283, (5402), 661-663.

3. Binnig, G.; Rohrer, H., Scanning Tunneling Microscopy. *IBM J. Res. Develop.* **1986,** 30, (4), 355-369.

4. Dujardin, E.; Mann, S., Bio-inspired Materials Chemistry. *Adv. Mater.* **2002,** 14, (11), 775-788.

5. Heath, J. R., Nanoscale Materials. *Acc. Chem. Res.* **1999,** 32, (5), 388-388.

6. Li, J.; Papadopoulos, C.; Xu, J., Nanoelectronics: Growing Y-junction carbon nanotubes. *Nature* **1999,** 402, (6759), 253-254.

7. Canham, L. T., Silicon quantum wire array fabrication by electrochemical and chemical dissolution of wafers. *Appl. Phys. Lett.* **1990,** 57, (10), 1046-1048.

8. Hill, N. A., Why are there so few magnetic ferroelectrics? *J. Phys. Chem. B* **2000,** 104, (29), 6694-6709.

9. Zheng, H.; Wang, J.; Lofland, S. E.; Ma, Z.; Mohaddes-Ardabili, L.; Zhao, T.; Salamanca-Riba, L.; Shinde, S. R.; Ogale, S. B.; Bai, F.; Viehland, D.; Jia, Y.; Schlom, D. G.; Wuttig, M.; Roytburd, A.; Ramesh, R., Multiferroic $BaTiO_3$-$CoFe_2O_4$ Nanostructures. *Science* **2004,** 303, (5658), 661-663.

10. Ahn, C. H.; Rabe, K. M.; Triscone, J. M., Ferroelectricity at the nanoscale: local polarization in oxide thin films and heterostructures. *Science* **2004,** 303, (5657), 488-491.

11. O'Brien, S.; Brus, L.; Murray, C. B., Synthesis of monodisperse nanoparticles of barium titanate: toward a generalized strategy of oxide nanoparticle synthesis. *J. Am. Chem. Soc.* **2001,** 123, (48), 12085-12086.

12. Urban, J. J.; Yun, W. S.; Gu, Q.; Park, H., Synthesis of single-crystalline perovskite nanorods composed of barium titanate and strontium titanate. *J. Am. Chem. Soc.* **2002,** 124, (7), 1186-1187.

13. Yun, W. S.; Urban, J. J.; Gu, Q.; Park, H., Ferroelectric properties of individual barium titanate nanowires investigated by scanned probe microscopy. *Nano Lett.* **2002,** 2, (5), 447-450.

14. Urban, J. J.; Spanier, J. E.; Lian, O. Y.; Yun, W. S.; Park, H., Single-crystalline barium titanate nanowires. *Adv. Mater.* **2003,** 15, (5), 423-426.

15. Mao, Y.; Banerjee, S.; Wong, S. S., Large-scale synthesis of single-crystalline perovskite nanostructures. *J. Am. Chem. Soc.* **2003,** 125, (51), 15718-15719.

16. Mao, Y.; Banerjee, S.; Wong, S. S., Hydrothermal synthesis of perovskite nanotubes. *Chem. Comm.* **2003**, (3), 408-409.

17. Mao, Y. B.; Park, T. J.; Wong, S. S., Synthesis of classes of ternary metal oxide nanostructures. *Chem. Comm.* **2005**, (46), 5721-5735.

18. Niederberger, M.; Garnweitner, G.; Pinna, N.; Antonietti, M., Nonaqueous and halide-free route to crystalline $BaTiO_3$, $SrTiO_3$, and $(Ba,Sr)TiO_3$ nanoparticles via a mechanism involving C-C bond formation. *J. Am. Chem. Soc.* **2004,** 126, (29), 9120-9126.

19. Petkov, V.; Gateshki, M.; Niederberger, M.; Ren, Y., Atomic-scale structure of nanocrystalline $Ba_xSr_{1-x}TiO_3$ (x= 1, 0.5, 0) by X-ray diffraction and the atomic pair distribution function technique. *Chem. Mater.* **2006,** 18, (3), 814-821.

20. Liu, H.; Hu, C.; Wang, Z. L., Composite-hydroxide-mediated approach for the synthesis of nanostructures of complex functional-oxides. *Nano Lett.* **2006,** 6, (7), 1535-1540.

21. Nuraje, N.; Su, K.; Haboosheh, A.; Samson, J.; Manning, E. P.; Yang, N.-L.; Matsui, H., Room temperature synthesis of ferroelectric barium titanate nanoparticles using peptide nanorings as templates. *Adv. Mater.* **2006,** 18, (6), 807-811.

22. Brutchey, R. L.; Morse, D. E., Template-free, low-temperature synthesis of crystalline barium titanate nanoparticles under bio-inspired conditions. *Angew. Chem., Int. Ed.* **2006,** 45, (39), 6564-6566.

23. Bansal, V.; Poddar, P.; Ahmad, A.; Sastry, M., Room-temperature biosynthesis of ferroelectric barium titanate nanoparticles. *J. Am. Chem. Soc.* **2006,** 128, (36), 11958-11963.

24. Shirakawa, H.; Louis, E. J.; MacDiarmid, A. G.; Chiang, C. K.; Heeger, A. J., Synthesis of electrically conducting organic polymers: halogen derivatives of polyacetylene, $(CH)_x$. *J. Chem. Soc., Chem. Commun.,* **1977**, (16), 578-580.

25. Heeger, A. J., Semiconducting and metallic polymers: the fourth generation of polymeric materials (Nobel lecture). *Angew. Chem. Int. Ed.* **2001,** 40, (14), 2591-2611.

26. MacDiarmid, A. G., "Synthetic metals": A novel role for organic polymers (Nobel lecture). *Angew. Chem. Int. Ed.* **2001,** 40, (14), 2581-2590.

27. Shirakawa, H., The discovery of polyacetylene film: the dawning of an era of conducting polymers (Nobel lecture). *Angew. Chem. Int. Ed.* **2001,** 40, (14), 2574-2580.

28. Shirakawa, H.; MacDiarmid, A.; Heeger, A., Twenty-five years of conducting polymers. *Chem. Comm.* **2003**, (1), 1-4.

29. Kuhn, R., Über die Synthese höherer Polyene. *Angew. Chem.* **1937,** 50, (34), 703-708.

30. Bohlmann, F.; Mannhardt, H.-J., Konstitution und Lichtabsorption, VIII. Mitteil.: Darstellung und Lichtabsorption von Dimethyl-polyenen. *Chem. Ber.* **1956,** 89, (5), 1307-1315.

31. Sondheimer, F.; Ben-Efraim, D. A.; Gaoni, Y., Unsaturated macrocyclic compounds. XVIII.1 the prototropic rearrangement of linear 1,5-diynes to conjugated polyen-ynes. *J. Am. Chem. Soc.* **1961,** 83, (7), 1682-1685.

32. Pople, J. A.; Walmsley, S. H., Bond alternation defects in long polyene molecules. *Mol. Phys.* **1962,** 5, (1), 15-20.

33. Pauson, P. L.; Proctor, G. R.; Rodger, W. J., 1-Thio-4-pyrone. *J. Chem. Soc.* **1965**, 3037-3040.

34. Ito, T.; Shirakawa, H.; Ikeda, S., Simultaneous polymerization and formation of polyacetylene film on the surface of concentrated soluble Ziegler-type catalyst solution. *J. Polym. Sci. Polym. Chem. Ed.* **1974,** 12, (1), 11-20.

35. Penn, D. R., Electron mean-free-path calculations using a model dielectric function. *Phys. Rev. B* **1987,** 35, (2), 482-486.

36. Sakaguchi, H.; Matsumura, H.; Gong, H., Electrochemical epitaxial polymerization of single-molecular wires. *Nat. Mater.* **2004,** 3, (8), 551-557.

37. Sirringhaus, H.; Brown, P. J.; Friend, R. H.; Nielsen, M. M.; Bechgaard, K.; Langeveld-Voss, B. M. W.; Spiering, A. J. H.; Janssen, R. A. J.; Meijer, E. W.; Herwig, P.; de Leeuw, D. M., Two-dimensional charge transport in self-organized, high-mobility conjugated polymers. *Nature* **1999,** 401, (6754), 685-688.

38. Meng, H.; Perepichka, D. F.; Bendikov, M.; Wudl, F.; Pan, G. Z.; Yu, W.; Dong, W.; Brown, S., Solid-state synthesis of a conducting polythiophene via an unprecedented heterocyclic coupling reaction. *J. Am. Chem. Soc.* **2003,** 125, (49), 15151-15162.

39. Su, K.; Nuraje, N.; Zhang, L.; Chu, I. W.; Peetz, R. M.; Matsui, H.; Yang, N.-L., Fast conductance switching in single-crystal organic nanoneedles prepared from an interfacial polymerization-crystallization of 3,4-ethylenedioxythiophene. *Adv. Mater.* **2007,** 19, (5), 669-672.

40. Qu, Y.; Zhang, G.; Ma, W.; Yao, K.; Yang, L., Electrochemically prepared heterojunction of polyaniline on n-SrTiO3. *Synth. Met.* **1997,** 89, (1), 57-62.

41. Blackwood, K. M., Device applications of side-chain ferroelectric liquid crystalline polymer films. *Science* **1996,** 273, (5277), 909-912.

42. Winslow, W. M., Induced fibration of suspensions. *J. Appl. Phys.* **1949,** 20, (12), 1137-1140.

43. Block, H.; Kelly, J. P., Electro-rheology. *J. Phys. D: Appl. Phys.* **1988,** 21, (12), 1661-1677.

44. Klingenberg, D. J.; Zukoski, C. F., Studies on the steady-shear behavior of electrorheological suspensions. *Langmuir* **1990,** 6, (1), 15-24.

45. Hao, T., Electrorheological Fluids. *Adv. Mater.* **2001,** 13, (24), 1847-1857.

Chapter Two

1. Nuraje, N.; Su, K.; Haboosheh, A.; Samson, J.; Manning, E. P.; Yang, N.-L.; Matsui, H., Room temperature synthesis of ferroelectric barium titanate nanoparticles using peptide nanorings as templates. *Adv. Mater.* **2006,** 18, (6), 807-811.

2. von Hippel, A.; Breckenridge, R. G.; Chesley, F. G.; Tisza, L., High dielectric constant ceramics. *Ind. Eng. Chem. Res.* **1946,** 38, (11), 1097-1109.

3. Matthias, B. T., Ferroelectricity. *Science* **1951,** 113, (2943), 591-599.

4. Cohen, R. E., Origin of ferroelectricity in perovskite oxides. *Nature* **1992,** 358, (6382), 136-138.

5. Chandler, C. D.; Roger, C.; Hampden-Smith, M. J., Chemical aspects of solution routes to perovskite-phase mixed-metal oxides from metal-organic precursors. *Chem. Rev.* **1993,** 93, (3), 1205.

6. Hill, N. A., Why are there so few magnetic ferroelectrics? *J. Phys. Chem. B* **2000,** 104, (29), 6694-6709.

7. Pena, M. A.; Fierro, J. L. G., Chemical structures and performance of perovskite oxides. *Chem. Rev.* **2001,** 101, (7), 1981-2018.

8. Ahn, C. H.; Rabe, K. M.; Triscone, J. M., Ferroelectricity at the nanoscale: local polarization in oxide thin films and heterostructures. *Science* **2004,** 303, (5657), 488-491.

9. Gherardi, P.; Matijevic, E., Homogeneous precipitation of spherical colloidal barium titanate particles. *Colloids Surf.* **1988,** 32, 257-274.

10. Corriu, R. J. P.; Leclercq, D.; Lefèvre, P.; Mutin, P. H.; Vioux, A., Preparation of monolithic metal oxide gels by a non-hydrolytic sol-gel process. *J. Mater. Chem.* **1992,** 2, (6), 673-674.

11. Dutta, P. K.; Gregg, J. R., Hydrothermal synthesis of tetragonal barium titanate ($BaTiO_3$) *Chem. Mater.* **1992,** 4, (4), 843-846.

12. Potdar, H. S.; Deshpande, S. B.; Godbole, P. D.; Gunjikar, V. J.; Date, S. K., Low temperature synthesis of ultrafine strontium titanate ($SrTiO_3$) powders. *J. Mater. Res.* **1992,** 7, (2), 429-434.

13. Pfaff, G., sol-gel synthesis of strontium titanate powders of various compositions. *J. Mater. Chem.* **1993,** 3, (7), 721-724.

14. Dutta, P. K.; Asiaie, R.; Akbar, S. A.; Zhu, W., Hydrothermal Synthesis and Dielectric Properties of Tetragonal $BaTiO_3$. *Chem. Mater.* **1994,** 6, (9), 1542-1548.

15. Wang, F.; Lauri, N., Preparation of strontium titanate using strontium titanyl oxalate as precursor. *Mater. Res. Bull.* **1994,** 29, (4), 451-458.

16. Frey, M. H.; Payne, D. A., Synthesis and processing of barium titanate ceramics from alkoxide solutions and monolithic gels. *Chem. Mater.* **1995,** 7, (1), 123-129.

17. Potdar, H. S.; Deshpande, S. B.; Date, S. K., Alternative route for synthesis of barium titanyl oxalate: molecular precursor for macrocrystalline barium titanate powders. *J. Am. Ceram. Soc.* **1996,** 79, (10), 2795-2797.

18. Vioux, A., Nonhydrolytic Sol-Gel Routes to Oxides. *Chem. Mater.* **1997,** 9, (11), 2292-2299.

19. Choi, J. Y.; Kim, C. H.; Kim, D. K., Hydrothermal synthesis of spherical perovskite oxide powders using spherical gel powders. *J. Am. Ceram. Soc.* **1998,** 81, (5), 1353-1356.

20. Clark, I. J.; Takeuchi, T.; Ohtori, N.; Sinclair, D. C., Hydrothermal synthesis and characterisation of $BaTiO_3$ fine powders: precursors, polymorphism and properties. *J. Mater. Chem.* **1999,** 9, (1), 83-91.

21. Khalil, K. M. S., Low temperature evolution of crystalline $BaTiO_3$ from alkali-metal free precursor using sol-gel process. *Mater. Res. Innovat.* **1999,** 2, (5), 256-262.

22. Wang, J.; Fang, J.; Ng, S.-C.; Gan, L.-M.; Chew, C.-H.; Wang, X.; Shen, Z., Ultrafine Barium Titanate Powders via Microemulsion Processing Routes. *J. Am. Ceram. Soc.* **1999,** 82, (4), 873-881.

23. Hu, M. Z. C.; Miller, G. A.; Payzant, E. A.; Rawn, C. J., Homogeneous (co)precipitation of inorganic salts for synthesis of monodispersed barium titanate particles. *J. Mater. Sci.* **2000,** 35, (12), 2927-2936.

24. Um, M. H.; Kumazawa, H., Hydrothermal synthesis of ferroelectric barium and strontium titanate extremely fine particles. *J. Mater. Sci.* **2000,** 35, (5), 1295-1300.

25. Ciftci, E.; Rahaman, M. N.; Shumsky, M., Hydrothermal precipitation and characterization of nanocrystalline BaTiO3 particles. *J. Mater. Sci.* **2001,** 36, (20), 4875-4882.

26. Lee, T.; Yao, N.; Imai, H.; Aksay, I. A., Barium titanate nanoparticles in block copolymer. *Langmuir* **2001,** 17, (24), 7656-7663.

27. O'Brien, S.; Brus, L.; Murray, C. B., Synthesis of monodisperse nanoparticles of barium titanate: toward a generalized strategy of oxide nanoparticle synthesis. *J. Am. Chem. Soc.* **2001,** 123, (48), 12085-12086.

28. Rumpf, H.; Modrow, H.; Hormes, J.; Glasel, H. J.; Hartmann, E.; Erdem, E.; Bottcher, R.; Hallmeier, K. H., Preparation of nanocrystalline BaTiO3 characterized by in situ x-ray absorption spectroscopy. *J. Phys. Chem. B* **2001,** 105, (17), 3415-3421.

29. Wada, S.; Tsurumi, T.; Chikamori, H.; Noma, T.; Suzuki, T., Preparation of nm-sized BaTiO3 crystallites by a LTDS method using a highly concentrated aqueous solution. *J. Cryst. Growth* **2001,** 229, (1-4), 433-439.

30. Wu, X.; Zou, L.; Yang, S.; Wang, D., Structural characterizations of organo-capped barium titanate nanoparticles prepared by the wet chemical route. *J. Colloid Interface Sci.* **2001,** 239, (2), 369-373.

31. Soten, I.; Miguez, H.; Yang, S. M.; Petrov, S.; Coombs, N.; Tetreault, N.; Matsuura, N.; Ruda, H. E.; Ozin, G. A., Barium titanate inverted opals-synthesis, characterization, and optical properties. *Adv. Funct. Mater.* **2002,** 12, (1), 71-77.

32. Urban, J. J.; Yun, W. S.; Gu, Q.; Park, H., Synthesis of single-crystalline perovskite nanorods composed of barium titanate and strontium titanate. *J. Am. Chem. Soc.* **2002,** 124, (7), 1186-1187.

33. Xu, H.; Gao, L.; Guo, J., Hydrothermal synthesis of tetragonal barium titanate from barium chloride and titanium tetrachloride under moderate conditions. *J. Am. Ceram. Soc.* **2002,** 85, (3), 727.

34. Yun, W. S.; Urban, J. J.; Gu, Q.; Park, H., Ferroelectric properties of individual barium titanate nanowires investigated by scanned probe Microscopy. *Nano Lett.* **2002,** 2, (5), 447-450.

35. Arya, P. R.; Jha, P.; Ganguli, A. K., Synthesis, characterization and dielectric properties of nanometer-sized barium strontium titanates prepared by the polymeric citrate precursor method. *J. Mater. Chem.* **2003,** 13, (2), 415-423.

36. Hung, K.-M.; Yang, W.-D.; Huang, C.-C., Preparation of nanometer-sized barium titanate powders by a sol-precipitation process with surfactants. *J. Eur. Ceram. Soc.* **2003,** 23, (11), 1901-1910.

37. Mao, Y.; Banerjee, S.; Wong, S. S., Large-scale synthesis of single-crystalline perovskite nanostructures. *J. Am. Chem. Soc.* **2003,** 125, (51), 15718-15719.

38. Mao, Y.; Banerjee, S.; Wong, S. S., Hydrothermal synthesis of perovskite nanotubes. *Chem. Comm.* **2003**, (3), 408-409.

39. Pérez-Maqueda, L. A.; Diánez, M. J.; Gotor, F. J.; Sayagués, M. J.; Real, C.; Criado, J. M., Synthesis of needle-like $BaTiO_3$ particles from the thermal decomposition of a citrate precursor under sample controlled reaction temperature conditions. *J. Mater. Chem.* **2003,** 13, (9), 2234-2241.

40. Urban, J. J.; Spanier, J. E.; Lian, O. Y.; Yun, W. S.; Park, H., Single-crystalline barium titanate nanowires. *Adv. Mater.* **2003,** 15, (5), 423-426.

41. Xu, H. R.; Gao, L., Tetragonal nanocrystalline barium titanate powder: preparation, characterization, and dielectric properties. *J. Am. Ceram. Soc.* **2003,** 86, (1), 203-205.

42. Li, J.; Wu, Y. J.; Tanaka, H.; Yamamoto, T.; Kuwabara, M., Preparation of a monodispersed suspension of barium titanate nanoparticles and electrophoretic deposition of thin films. *J. Am. Ceram. Soc.* **2004,** 87, (8), 1578-1581.

43. Niederberger, M.; Garnweitner, G.; Pinna, N.; Antonietti, M., Nonaqueous and halide-free route to crystalline $BaTiO_3$, $SrTiO_3$, and $(Ba,Sr)TiO_3$ nanoparticles via a mechanism involving C-C bond formation. *J. Am. Chem. Soc.* **2004,** 126, (29), 9120-9126.

44. Niederberger, M.; Pinna, N.; Polleux, J.; Antonietti, M., A general soft-chemistry route to perovskites and related materials: synthesis of $BaTiO_3$, $BaZrO_3$, and $LiNbO_3$ nanoparticles. *Angew. Chem., Int. Ed.* **2004,** 43, (17), 2270-2273.

45. Ahmad, T.; Kavitha, G.; Narayana, C.; Ganguli, A. K., Nanostructured barium titanate prepared through a modified reverse micellar route: Structural distortion and dielectric properties. *J. Mater. Res.* **2005,** 20, (6), 1415-1421.

46. Hakuta, Y.; Ura, H.; Hayashi, H.; Arai, K., Continuous production of BaTiO3 nanoparticles by hydrothermal synthesis. *Ind. Eng. Chem. Res.* **2005,** 44, (4), 840-846.

47. Hwu, J.-M.; Yu, W.-H.; Yang, W.-C.; Chen, Y.-W.; Chou, Y.-Y., Characterization of dielectric barium titanate powders prepared by homogeneous precipitation chemical reaction for embedded capacitor applications. *Mater. Res. Bull.* **2005,** 40, (10), 1662-1679.

48. Joshi, U. A.; Lee, J. S., Template-free hydrothermal synthesis of single-crystalline barium titanate and strontium titanate nanowires. *Small* **2005,** 1, (12), 1172-1176.

49. Mao, Y. B.; Park, T. J.; Wong, S. S., Synthesis of classes of ternary metal oxide nanostructures. *Chem. Comm.* **2005**, (46), 5721-5735.

50. Qi, J. Q.; Wang, Y.; Ping Chen, W.; Tu Li, L.; Lai Wah Chan, H., Direct large-scale synthesis of perovskite barium strontium titanate nano-particles from solutions. *J. Solid State Chem.* **2005,** 178, (1), 279-284.

51. Reverón, H.; Aymonier, C.; Loppinet-Serani, A.; Elissalde, C.; Maglione, M.; Cansell, F., Single-step synthesis of well-crystallized and pure barium titanate nanoparticles in supercritical fluids. *Nanotechnology* **2005**, (8), 1137-1143.

52. Wang, X.; Zhuang, J.; Peng, Q.; Li, Y., A general strategy for nanocrystal synthesis. *Nature* **2005,** 437, (7055), 121-124.

53. Xie, X. H.; Dong, Y. M.; Chen, C. J.; Lin, L., Nonhydrolytic Sol-Gel Synthesis of $Ba_{1-x}Sr_xTiO_3$ Nanopowder. *Ind. Eng. Chem. Res.* **2005,** 44, (4), 811-815.

54. Yuh, J.; Nino, J. C.; Sigmund, W. M., Synthesis of barium titanate ($BaTiO_3$) nanofibers via electrospinning. *Mater. Lett.* **2005,** 59, (28), 3645-3647.

55. Liu, H.; Hu, C.; Wang, Z. L., Composite-hydroxide-mediated approach for the synthesis of nanostructures of complex functional-oxides. *Nano Lett.* **2006,** 6, (7), 1535-1540.

56. Huang, L.; Chen, Z.; Wilson, J. D.; Banerjee, S.; Robinson, R. D.; Herman, I. P.; Laibowitz, R.; O'Brien, S., Barium titanate nanocrystals and nanocrystal thin films: Synthesis, ferroelectricity, and dielectric properties. *J. Appl. Phys.* **2006,** 100, (3), 034316-10.

57. Bansal, V.; Poddar, P.; Ahmad, A.; Sastry, M., Room-temperature biosynthesis of ferroelectric barium titanate nanoparticles. *J. Am. Chem. Soc.* **2006,** 128, (36), 11958-11963.

58. Brutchey, R. L.; Morse, D. E., Template-free, low-temperature synthesis of crystalline barium titanate nanoparticles under bio-inspired conditions. *Angew. Chem., Int. Ed.* **2006,** 45, (39), 6564-6566.

59. Rogan, R. C.; Tamura, N.; Swift, G. A.; Ustundag, E., Direct measurement of triaxial strain fields around ferroelectric domains using X-ray microdiffraction. *Nat. Mater.* **2003,** 2, (6), 379-381.

60. Tenne, D. A.; Bruchhausen, A.; Lanzillotti-Kimura, N. D.; Fainstein, A.; Katiyar, R. S.; Cantarero, A.; Soukiassian, A.; Vaithyanathan, V.; Haeni, J. H.; Tian, W.; Schlom, D. G.; Choi, K. J.; Kim, D. M.; Eom, C. B.; Sun, H. P.; Pan, X. Q.; Li, Y. L.; Chen, L. Q.; Jia, Q. X.; Nakhmanson, S. M.; Rabe, K. M.; Xi, X. X., Probing nanoscale ferroelectricity by ultraviolet Raman spectroscopy. *Science* **2006,** 313, (5793), 1614-1616.

61. Petkov, V.; Gateshki, M.; Niederberger, M.; Ren, Y., Atomic-scale structure of nanocrystalline $Ba_xSr_{1-x}TiO_3$ (x= 1, 0.5, 0) by X-ray diffraction and the atomic pair distribution function technique. *Chem. Mater.* **2006,** 18, (3), 814-821.

62. Yashima, M.; Hoshina, T.; Ishimura, D.; Kobayashi, S.; Nakamura, W.; Tsurumi, T.; Wada, S., Size effect on the crystal structure of barium titanate nanoparticles. *J. Appl. Phys.* **2005,** 98, (1), 014313-8.

63. Ohno, T.; Suzuki, D.; Suzuki, H., Size effect for barium titanate nano-particles. *Kona* **2004,** 22, 195-201.

64. Yan, T.; Shen, Z.-G.; Chen, J.-F.; Liu, X.-L.; Tao, X.; Yun, J., Synthesis of well-isolated barium titanium trioxide nanocubes. *Chem. Lett.* **2005,** 34, (8), 1196-1197.

65. Cha, J. N.; Stucky, G. D.; Morse, D. E.; Deming, T. J., Biomimetic synthesis of ordered silica structures mediated by block copolypeptides. *Nature* **2000,** 403, (6767), 289-292.

66. Sarikaya, M.; Tamerler, C.; Jen, A. K. Y.; Schulten, K.; Baneyx, F., Molecular biomimetics: nanotechnology through biology. *Nat. Mater.* **2003,** 2, (9), 577-585.

67. Whitling, J. M.; Spreitzer, G.; Wright, D. W., A Combinatorial and informatics approach to CdS nanoclusters. *Adv. Mater.* **2000,** 12, (18), 1377-1380.

68. Reches, M.; Gazit, E., Casting metal nanowires within discrete self-assembled peptide nanotubes. *Science* **2003,** 300, (5619), 625-627.

69. Bansal, V.; Sanya, A.; Rautaray, D.; Ahmad, A.; Sastry, M., Bioleaching of sand by the fungus fusarium oxysporum as a means of producing extracellular silica nanoparticles. *Adv. Mater.* **2005,** 17, (7), 889-892.

70. Walsh, D.; Arcelli, L.; Ikoma, T.; Tanaka, J.; Mann, S., Dextran templating for the synthesis of metallic and metal oxide sponges. *Nat. Mater.* **2003,** 2, (6), 386-390.

71. Douglas, T.; Young, M., Virus particles as templates for materials synthesis. *Adv. Mater.* **1999,** 11, (8), 679-681.

72. Loste, E.; Park, R. J.; Warren, J.; Meldrum, F. C., Precipitation of calcium carbonate in confinement. *Adv. Funct. Mater.* **2004,** 14, (12), 1211-1220.

73. Aizenberg, J.; Muller, D. A.; Grazul, J. L.; Hamann, D. R., Direct fabrication of large micropatterned single crystals. *Science* **2003,** 299, (5610), 1205-1208.

74. Kogiso, M.; Ohnishi, S.; Yase, K.; Masuda, M.; Shimizu, T., Dicarboxylic oligopeptide bolaamphiphiles: proton-triggered self-assembly of microtubes with loose solid surfaces. *Langmuir* **1998,** 14, (18), 4978-4986.

75. Banerjee, I. A.; Yu, L.; Matsui, H., Cu nanocrystal growth on peptide nanotubes by biomineralization: Size control of Cu nanocrystals by tuning peptide conformation. *Proc. Natl. Acad. Sci. USA* **2003,** 100, (25), 14678-14682.

76. Djalali, R.; Samson, J.; Matsui, H., Doughnut-shaped peptide nano-sssemblies and their applications as nanoreactors. *J. Am. Chem. Soc.* **2004,** 126, (25), 7935-7939.

77. Nuraje, N.; Su, K.; Samson, J.; Haboosheh, A.; Maccuspie, R. I.; Matsui, H., Self-assembly of Au aanoparticle-containing peptide nano-rings on surfaces. *Supramol. Chem.* **2006,** 18, (5), 429-434.

78. Dutta, P. K.; Gallagher, P. K.; Twu, J., Raman spectroscopic study of the formation of barium titanate from an oxalate precursor. *Chem. Mater.* **1993,** 5, (12), 1739-1743.

79. Krauss, T. D.; Brus, L. E., Charge, polarizability, and photoionization of single semiconductor nanocrystals. *Phys. Rev. Lett.* **1999,** 83, (23), 4840-4843.

80. Krauss, T. D.; O'Brien, S.; Brus, L. E., Charge and photoionization properties of single semiconductor nanocrystals. *J. Phys. Chem. B* **2001,** 105, (9), 1725-1733.

81. Cherniavskaya, O.; Chen, L.; Weng, V.; Yuditsky, L.; Brus, L. E., Quantitative noncontact electrostatic force imaging of nanocrystal polarizability. *J. Phys. Chem. B* **2003,** 107, (7), 1525-1531.

82. Jiang, J.; Krauss, T. D.; Brus, L. E., Electrostatic force microscopy characterization of trioctylphosphine oxide self-assembled monolayers on graphite. *J. Phys. Chem. B* **2000,** 104, (50), 11936-11941.

83. Heim, T.; Lmimouni, K.; Vuillaume, D., Ambipolar charge injection and transport in a single pentacene monolayer island. *Nano Lett.* **2004,** 4, (11), 2145-2150.

Chapter Three

1. Chandler, C. D.; Roger, C.; Hampden-Smith, M. J., Chemical aspects of solution routes to perovskite-phase mixed-metal oxides from metal-organic precursors. *Chem. Rev.* **1993,** 93, (3), 1205.

2. Pena, M. A.; Fierro, J. L. G., Chemical structures and performance of perovskite oxides. *Chem. Rev.* **2001,** 101, (7), 1981-2018.

3. Hill, N. A., Why are there so few magnetic ferroelectrics? *J. Phys. Chem. B* **2000,** 104, (29), 6694-6709.

4. Ahn, C. H.; Rabe, K. M.; Triscone, J. M., Ferroelectricity at the nanoscale: local polarization in oxide thin films and heterostructures. *Science* **2004,** 303, (5657), 488-491.

5. Huang, L.; Chen, Z.; Wilson, J. D.; Banerjee, S.; Robinson, R. D.; Herman, I. P.; Laibowitz, R.; O'Brien, S., Barium titanate nanocrystals and nanocrystal thin films: Synthesis, ferroelectricity, and dielectric properties. *J. Appl. Phys.* **2006,** 100, (3), 034316-10.

6. O'Brien, S.; Brus, L.; Murray, C. B., Synthesis of monodisperse nanoparticles of barium titanate: toward a generalized strategy of oxide nanoparticle synthesis. *J. Am. Chem. Soc.* **2001,** 123, (48), 12085-12086.

7. Urban, J. J.; Yun, W. S.; Gu, Q.; Park, H., Synthesis of single-crystalline perovskite nanorods composed of barium titanate and strontium titanate. *J. Am. Chem. Soc.* **2002,** 124, (7), 1186-1187.

8. Yun, W. S.; Urban, J. J.; Gu, Q.; Park, H., Ferroelectric properties of individual barium titanate nanowires investigated by scanned probe Microscopy. *Nano Lett.* **2002,** 2, (5), 447-450.

9. Urban, J. J.; Spanier, J. E.; Lian, O. Y.; Yun, W. S.; Park, H., Single-crystalline barium titanate nanowires. *Adv. Mater.* **2003,** 15, (5), 423-426.

10. Mao, Y.; Banerjee, S.; Wong, S. S., Large-scale synthesis of single-crystalline perovskite nanostructures. *J. Am. Chem. Soc.* **2003,** 125, (51), 15718-15719.

11. Mao, Y.; Banerjee, S.; Wong, S. S., Hydrothermal synthesis of perovskite nanotubes. *Chem. Comm.* **2003**, (3), 408-409.

12. Niederberger, M.; Garnweitner, G.; Pinna, N.; Antonietti, M., Nonaqueous and halide-free route to crystalline $BaTiO_3$, $SrTiO_3$, and $(Ba,Sr)TiO_3$ nanoparticles via a mechanism involving C-C bond formation. *J. Am. Chem. Soc.* **2004,** 126, (29), 9120-9126.

13. Niederberger, M.; Pinna, N.; Polleux, J.; Antonietti, M., A general soft-chemistry route to perovskites and related materials: synthesis of $BaTiO_3$, $BaZrO_3$, and $LiNbO_3$ nanoparticles. *Angew. Chem., Int. Ed.* **2004,** 43, (17), 2270-2273.

14. Mao, Y. B.; Park, T. J.; Wong, S. S., Synthesis of classes of ternary metal oxide nanostructures. *Chem. Comm.* **2005**, (46), 5721-5735.

15. Nuraje, N.; Su, K.; Haboosheh, A.; Samson, J.; Manning, E. P.; Yang, N.-L.; Matsui, H., Room temperature synthesis of ferroelectric barium titanate nanoparticles using peptide nanorings as templates. *Adv. Mater.* **2006,** 18, (6), 807-811.

16. Bansal, V.; Poddar, P.; Ahmad, A.; Sastry, M., Room-temperature biosynthesis of ferroelectric barium titanate nanoparticles. *J. Am. Chem. Soc.* **2006,** 128, (36), 11958-11963.

17. Brutchey, R. L.; Morse, D. E., Template-free, low-temperature synthesis of crystalline barium titanate nanoparticles under bio-inspired conditions. *Angew. Chem., Int. Ed.* **2006,** 45, (39), 6564-6566.

18. Liu, H.; Hu, C.; Wang, Z. L., Composite-hydroxide-mediated approach for the synthesis of nanostructures of complex functional-oxides. *Nano Lett.* **2006,** 6, (7), 1535-1540.

19. Wada, S.; Tsurumi, T.; Chikamori, H.; Noma, T.; Suzuki, T., Preparation of nm-sized BaTiO3 crystallites by a LTDS method using a highly concentrated aqueous solution. *J. Cryst. Growth* **2001,** 229, (1-4), 433-439.

20. Xu, H. R.; Gao, L., Tetragonal nanocrystalline barium titanate powder: preparation, characterization, and dielectric properties. *J. Am. Ceram. Soc.* **2003,** 86, (1), 203-205.

21. Arya, P. R.; Jha, P.; Ganguli, A. K., Synthesis, characterization and dielectric properties of nanometer-sized barium strontium titanates prepared by the polymeric citrate precursor method. *J. Mater. Chem.* **2003,** 13, (2), 415-423.

22. Dutta, P. K.; Gregg, J. R., Hydrothermal synthesis of tetragonal barium titanate ($BaTiO_3$) *Chem. Mater.* **1992,** 4, (4), 843-846.

23. Dutta, P. K.; Asiaie, R.; Akbar, S. A.; Zhu, W., Hydrothermal Synthesis and Dielectric Properties of Tetragonal $BaTiO_3$. *Chem. Mater.* **1994,** 6, (9), 1542-1548.

24. Um, M. H.; Kumazawa, H., Hydrothermal synthesis of ferroelectric barium and strontium titanate extremely fine particles. *J. Mater. Sci.* **2000,** 35, (5), 1295-1300.

25. Frey, M. H.; Payne, D. A., Synthesis and processing of barium titanate ceramics from alkoxide solutions and monolithic gels. *Chem. Mater.* **1995,** 7, (1), 123-129.

26. Fu, H.; Bellaiche, L., Ferroelectricity in barium titanate quantum dots and wires. *Phys. Rev. Lett.* **2003,** 91, (25), 257601.

27. Dawber, M.; Chandra, P.; Littlewood, P. B.; Scott, J. F., Depolarization corrections to the coercive field in thin-film ferroelectrics. *J. Phys.: Condens. Matter* **2003**, (24), L393-L398.

28. Junquera, J.; Ghosez, P., Critical thickness for ferroelectricity in perovskite ultrathin films. *Nature* **2003,** 422, (6931), 506-509.

29. Petkov, V.; Gateshki, M.; Niederberger, M.; Ren, Y., Atomic-scale structure of nanocrystalline $Ba_xSr_{1-x}TiO_3$ (x= 1, 0.5, 0) by X-ray diffraction and the atomic pair distribution function technique. *Chem. Mater.* **2006,** 18, (3), 814-821.

30. Lee, J.; Kim, L.; Kim, J.; Kim, Y.; Jung, D., *in Fundamental Physics of Ferroelectrics 2002*. American Insitute of Physics: Washington DC, 2002; p 178-187.

31. Pileni, M.-P., The role of soft colloidal templates in controlling the size and shape of inorganic nanocrystals. *Nat. Mater.* **2003,** 2, (3), 145-150.

32. Su, K.; Yang, N.-L., Synthesis of strontium titanate/polyaniline nanocomposites and the study of their electrorheological effect. *Polym. Prep.* **2004,** 45, (2), 533-534.

33. Davis, L.; Rubin, L. G., Some dielectricproperties of barium-strontium titanate ceramics at 3000 megacycles. *J. Appl. Phys.* **1953,** 24, (9), 1194-1197.

34. Kisaka, S.; Ikegami, S.; Sasaki, H., Dielectric properties of mixed crystals of barium-strontium titanate. *J. Phys. Soc. Jpn.* **1959,** 14, (12), 1680-1685.

35. Hilton, A. D.; Ricketts, B. W., Dielectric properties of $Ba_{1-x}Sr_xTiO_3$ ceramics. *J. Phys. D: Appl. Phys.* **1996,** 29, 1321-1325.

36. Tanaka, H.; Tabata, H.; Ota, K. i.; Kawai, T., Molecular-dynamics prediction of structural anomalies in ferroelectric and dielectric $BaTiO_3$-$SrTiO_3$-$CaTiO_3$ solid solutions. *Phys. Rev. B* **1996,** 53, (21), 14112-14116.

37. Yashima, M.; Hoshina, T.; Ishimura, D.; Kobayashi, S.; Nakamura, W.; Tsurumi, T.; Wada, S., Size effect on the crystal structure of barium titanate nanoparticles. *J. Appl. Phys.* **2005,** 98, (1), 014313-8.

Chapter Four

1. Su, K.; Nuraje, N.; Zhang, L.; Chu, I. W.; Peetz, R. M.; Matsui, H.; Yang, N. L., Fast conductance switching in single-crystal organic nanoneedles prepared from an interfacial polymerization-crystallization of 3,4-ethylenedioxythiophene. *Adv. Mater.* **2007,** 19, (5), 669-672.

2. Gross, M.; Muller, D. C.; Nothofer, H.-G.; Scherf, U.; Neher, D.; Brauchle, C.; Meerholz, K., Improving the performance of doped π-conjugated polymers for use in organic light-emitting diodes. *Nature* **2000,** 405, (6787), 661-665.

3. Tretiak, S.; Saxena, A.; Martin, R. L.; Bishop, A. R., Photoexcited breathers in conjugated polyenes: An excited-state molecular dynamics study. *Proc. Natl. Acad. Sci. USA* **2003,** 100, (5), 2185-2190.

4. Chen, L.; McBranch, D. W.; Wang, H.-L.; Helgeson, R.; Wudl, F.; Whitten, D. G., Highly sensitive biological and chemical sensors based on reversible fluorescence quenching in a conjugated polymer. *Proc. Natl. Acad. Sci. USA* **1999,** 96, (22), 12287-12292.

5. Hide, F.; Diaz-Garcia, M. A.; Schwartz, B. J.; Andersson, M. R.; Pei, Q.; Heeger, A. J., Semiconducting polymers: a new class of solid-state laser materials. *Science* **1996,** 273, (5283), 1833-1836.

6. Dimitrakopoulos, C. D.; Mascaro, D. J., Organic thin-film transistors: A review of recent advances. *IBM J. Res. Rev.* **2001,** 45, (1), 11-27.

7. Collier, C. P.; Wong, E. W.; Belohradsk, M.; Raymo, F. M.; Stoddart, J. F.; Kuekes, P. J.; Williams, R. S.; Heath, J. R., Electronically Configurable Molecular-Based Logic Gates. *Science* **1999,** 285, (5426), 391-394.

8. He, H.; Zhu, J.; Tao, N. J.; Nagahara, L. A.; Amlani, I.; Tsui, R., A Conducting Polymer Nanojunction Switch. *J. Am. Chem. Soc.* **2001,** 123, (31), 7730-7731.

9. Ramachandran, G. K.; Hopson, T. J.; Rawlett, A. M.; Nagahara, L. A.; Primak, A.; Lindsay, S. M., A bond-fluctuation mechanism for stochastic switching in wired molecules. *Science* **2003,** 300, (5624), 1413-1416.

10. Terabe, K.; Hasegawa, T.; Nakayama, T.; Aono, M., Quantized conductance atomic switch. *Nature* **2005,** 433, (7021), 47-50.

11. Sakaguchi, H.; Matsumura, H.; Gong, H., Electrochemical epitaxial polymerization of single-molecular wires. *Nat. Mater.* **2004,** 3, (8), 551-557.

12. Ong, B. S.; Wu, Y.; Liu, P.; Gardner, S., Structurally ordered polythiophene nanoparticles for high-performance organic thin-film transistors. *Adv. Mater.* **2005,** 17, (9), 1141-1144.

13. Winther-Jensen, B.; Chen, J.; West, K.; Wallace, G., Vapor phase polymerization of pyrrole and thiophene using iron(iii) sulfonates as oxidizing agents. *Macromolecules* **2004,** 37, (16), 5930-5935.

14. Krebs, F. C.; Biancardo, M.; Winther-Jensen, B.; Spanggard, H.; Alstrup, J., Strategies for incorporation of polymer photovoltaics into garments and textiles. *Sol. Energy Mater. Sol. Cells* **2006,** 90, (7-8), 1058-1067.

15. Krebs, F. C.; Jorgensen, M., High carrier mobility in a series of new semiconducting PPV-type polymers. *Macromolecules* **2003,** 36, (12), 4374-4384.

16. Ulanski, J.; Goeckelmann, K.; Wegner, G., Electrochemically induced deterioration of conductivity of radical-cation salt of quaterphenyl. *Mat. Sci.* **1987,** 13, (1-2), 283-286.

17. Wegner, G.; Monkenbusch, M.; Wieners, G.; Weizenhoefer, R.; Lieser, G.; Wernet, W., New routes to conducting polymers and new insights into structure-properties relations. *Mol. Cryst. Liq. Cryst.* **1985,** 118, (1-4), 85-94.

18. Sirringhaus, H.; Brown, P. J.; Friend, R. H.; Nielsen, M. M.; Bechgaard, K.; Langeveld-Voss, B. M. W.; Spiering, A. J. H.; Janssen, R. A. J.; Meijer, E. W.; Herwig, P.; de Leeuw, D. M., Two-dimensional charge transport in self-organized, high-mobility conjugated polymers. *Nature* **1999,** 401, (6754), 685-688.

19. Meng, H.; Perepichka, D. F.; Bendikov, M.; Wudl, F.; Pan, G. Z.; Yu, W.; Dong, W.; Brown, S., Solid-state synthesis of a conducting polythiophene via an unprecedented heterocyclic coupling reaction. *J. Am. Chem. Soc.* **2003,** 125, (49), 15151-15162.

20. Heeger, A. J., Semiconducting and metallic polymers: the fourth generation of polymeric materials (Nobel lecture). *Angew. Chem. Int. Ed.* **2001,** 40, (14), 2591-2611.

21. Leclerc, M.; Diaz, F. M.; Wegner, G., Structural analysis of poly(3-alkylthiophene)s. *Makromol. Chem.* **1989,** 190, (12), 3105-3116.

22. Andreani, F.; Bizzari, P. C.; Casa, C. D.; Salatelli, E., First approach to ester-functionalized poly(3-alkylthienylene)s. *Polym. Bull.* **1991,** 27, (2), 117-121.

23. Abdou, M. S. A.; Lu, X.; Xie, Z. W.; Orfino, F.; Deen, M. J.; Holdcroft, S., Nature of impurities in π-conjugated polymers prepared by ferric chloride and their effect on the electrical properties of metal-insulator-semiconductor structures. *Chem. Mater.* **1995,** 7, (4), 631-641.

24. McCullough, R. D., The chemistry of conducting polythiophenes. *Adv. Mater.* **1998,** 10, (2), 93-116.

25. Huang, J.; Kaner, R. B., A General Chemical Route to Polyaniline Nanofibers. *J. Am. Chem. Soc.* **2004,** 126, (3), 851-855.

26. Joo, J.; Long, S. M.; Pouget, J. P.; Oh, E. J.; MacDiarmid, A. G.; Epstein, A. J., Charge transport of the mesoscopic metallic state in partially crystalline polyanilines. *Phys. Rev. B* **1998,** 57, (16), 9567-9580.

27. Mo, Z.; Lee, K. B.; Moon, Y. B.; Kobayashi, M.; Heeger, A. J.; Wudl, F., X-ray scattering from poly(thiophene): crystallinity and crystallographic structure. *Macromolecules* **1985,** 18, (10), 1972-1977.

28. Granstrom, M.; Inganas, O., Electrically conductive polymer fibers with mesoscopic diameters .1. studies of structure and electrical-properties. *Polymer* **1995,** 36, (15), 2867-2872.

29. Groenendaal, L.; Jonas, F.; Freitag, D.; Pielartzik, H.; Reynolds, J. R., Poly(3,4-ethylenedioxythiophene) and its derivatives: past, present, and future. *Adv. Mater.* **2000,** 12, (7), 481-494.

30. Aasmundtveit, K. E.; Samuelsen, E. J.; Inganas, O.; Pettersson, L. A. A.; Johansson, T.; Ferrer, S., Structural aspects of electrochemical doping and dedoping of poly(3,4-ethylenedioxythiophene). *Synth. Met.* **2000,** 113, (1-2), 93-97.

31. Niu, L.; Kvarnstrom, C.; Froberg, K.; Ivaska, A., Electrochemically controlled surface morphology and crystallinity in poly(3,4-ethylenedioxythiophene) films. *Synth. Met.* **2001,** 122, (2), 425-429.

32. Ozaki, M.; Kratohvil, S.; Matijevic, E., Formation of monodispersed spindle-type hematite particles. *J. Colloid Interface Sci.* **1984,** 102, (1), 146-151.

33. Shafi, K. V. P. M.; Ulman, A.; Yan, X.; Yang, N. L.; Estournes, C.; White, H.; Rafailovich, M., Sonochemical synthesis of functionalized amorphous iron oxide nanoparticles. *Langmuir* **2001,** 17, (16), 5093-5097.

34. Donhauser, Z. J.; Mantooth, B. A.; Kelly, K. F.; Bumm, L. A.; Monnell, J. D.; Stapleton, J. J.; Price, D. W., Jr.; Rawlett, A. M.; Allara, D. L.; Tour, J. M.;

Weiss, P. S., Conductance switching in single molecules through conformational changes. *Science* **2001,** 292, (5525), 2303-2307.

35. Ulanski, J.; Glatzhofer, D. T.; Wegner, G., Comment on the Application of the Voltage Shorted Compaction (Vsc) Technique to Conducting Polymers. *Makromol. Chem. Rapid Commun.* **1986,** 7, (6), 361-363.

36. Huang, J.; Kaner, R. B., Nanofiber formation in the chemical polymerization of aniline: a mechanistic study. *Angew. Chem. Int. Ed.* **2004,** 43, (43), 5817-5821.

Chapter Five

1. Su, K.; Yang, N.-L., Synthesis of strontium titanate/polyaniline nanocomposites and the study of their electrorheological effect. *Polym. Prep.* **2004,** 45, (2), 533-534.

2. Winslow, W. M., Induced Fibration of Suspensions. *J. Appl. Phys.* **1949,** 20, (12), 1137-1140.

3. Block, H.; Kelly, J. P., Electro-rheology. *J. Phys. D: Appl. Phys.* **1988,** 21, (12), 1661-1677.

4. Wang, Z. H.; Javadi, H. H. S.; Ray, A.; MacDiarmid, A. G.; Epstein, A. J., Electron localization in polyaniline derivatives. *Phys. Rev. B* **1990,** 42, (8), 5411.

5. Abdou, M. S. A.; Lu, X.; Xie, Z. W.; Orfino, F.; Deen, M. J.; Holdcroft, S., Nature of impurities in p-conjugated polymers prepared by ferric chloride and their effect on the electrical properties of metal-insulator-semiconductor structures. *Chem. Mater.* **1995,** 7, (4), 631-641.

6. Jun, J.-B.; Suh, K.-D., Preparation and electrorheological characterization of suspensions of poly(urethane acrylate)/clay nanocomposite particles. *J. Appl. Polym. Sci.* **2003,** 90, (2), 458-464.

7. Wang, B.; Zhao, X., Preparation of kaolinite/titania coated nanocomposite particles and their electrorheological properties. *J. Mater. Chem.* **2003,** 13, (9), 2248-2253.

8. Wen, W. J.; Huang, X. X.; Yang, S. H.; Lu, K. Q.; Sheng, P., The giant electrorheological effect in suspensions of nanoparticles. *Nat. Mater.* **2003,** 2, (11), 727-730.

9. Cho, M. S.; Choi, H. J.; Ahn, W. S., Enhanced Electrorheology of Conducting Polyaniline Confined in MCM-41 Channels. *Langmuir* **2004,** 20, (1), 202-207.

10. Hirano, S.-i.; Yogo, T.; Sakamoto, W.; Banno, K.; Fukuzawa, R., Novel electro-rheological nanocrystalline dielectric particles modified with or embedded in organics. *J. Eur. Ceram. Soc.* **2004,** 24, (6), 1911-1917.

11. Wei, J. H.; Shi, J.; Guan, J. G.; Yuan, R. Z., Synthesis and electrorheological effect of PAn-$BaTiO_3$ nanocomposite. *J. Mater. Sci.* **2004,** 39, (10), 3457-3460.

12. Park, S. J.; Cho, M. S.; Lim, S. T.; Choi, H. J.; Jhon, M. S., Electrorheology of Multiwalled Carbon Nanotube/Poly(methyl methacrylate) Nanocomposites. *Macromol. Rapid Commun.* **2005,** 26, (19), 1563-1566.

13. Ong, B. S.; Wu, Y.; Liu, P.; Gardner, S., Structurally ordered polythiophene nanoparticles for high-performance organic thin-film transistors. *Adv. Mater.* **2005,** 17, (9), 1141-1144.

14. Lozano, K.; Hernandez, C.; Petty, T. W.; Sigman, M. B.; Korgel, B., Electrorheological analysis of nano laden suspensions. *J. Colloid Interface Sci.* **2006,** 297, (2), 618-624.

15. Yin, J.; Zhao, X., Titanate nano-whisker electrorheological fluid with high suspended stability and ER activity. *Nanotechnology* **2006,** 17, (1), 192-196.

16. Klingenberg, D. J.; Zukoski, C. F., Studies on the steady-shear behavior of electrorheological suspensions. *Langmuir* **1990,** 6, (1), 15-24.

17. Hao, T.; Kawai, A.; Ikazaki, F., Mechanism of the Electrorheological Effect: Evidence from the Conductive, Dielectric, and Surface Characteristics of Water-Free Electrorheological Fluids. *Langmuir* **1998,** 14, (5), 1256-1262.

18. Quadrat, O.; Stejskal, J., Polyaniline in electrotheology. *J. Ind. Eng. Chem.* **2006,** 12, (3), 352-361.

19. Qu, Y.; Zhang, G.; Ma, W.; Yao, K.; Yang, L., Electrochemically prepared heterojunction of polyaniline on n-SrTiO3. *Synth. Met.* **1997,** 89, (1), 57-62.

20. Pileni, M.-P., The role of soft colloidal templates in controlling the size and shape of inorganic nanocrystals. *Nat. Mater.* **2003,** 2, (3), 145-150.

21. Mao, Y.; Banerjee, S.; Wong, S. S., Hydrothermal synthesis of perovskite nanotubes. *Chem. Comm.* **2003**, (3), 408-409.

22. Niederberger, M.; Garnweitner, G.; Pinna, N.; Antonietti, M., Nonaqueous and halide-free route to crystalline $BaTiO_3$, $SrTiO_3$, and $(Ba,Sr)TiO_3$ nanoparticles via a mechanism involving C-C bond formation. *J. Am. Chem. Soc.* **2004,** 126, (29), 9120-9126.

23. Um, M. H.; Kumazawa, H., Hydrothermal synthesis of ferroelectric barium and strontium titanate extremely fine particles. *J. Mater. Sci.* **2000,** 35, (5), 1295-1300.

24. Niederberger, M.; Pinna, N.; Polleux, J.; Antonietti, M., A general soft-chemistry route to perovskites and related materials: synthesis of $BaTiO_3$, $BaZrO_3$, and $LiNbO_3$ nanoparticles. *Angew. Chem., Int. Ed.* **2004,** 43, (17), 2270-2273.

25. O'Brien, S.; Brus, L.; Murray, C. B., Synthesis of Monodisperse Nanoparticles of Barium Titanate: Toward a Generalized Strategy of Oxide Nanoparticle Synthesis. *J. Am. Chem. Soc.* **2001,** 123, (48), 12085-12086.

26. Urban, J. J.; Yun, W. S.; Gu, Q.; Park, H., Synthesis of single-crystalline perovskite nanorods composed of barium titanate and strontium titanate. *J. Am. Chem. Soc.* **2002,** 124, (7), 1186-1187.

27. Mao, Y.; Banerjee, S.; Wong, S. S., Large-scale synthesis of single-crystalline perovskite nanostructures. *J. Am. Chem. Soc.* **2003,** 125, (51), 15718-15719.

28. Zhang, L.; Su, K.; Li, X., Electrorheological effects of polyaniline-type electrorheological fluids. *J. Appl. Polym. Sci.* **2003,** 87, (5), 733-740.

29. Su, K.; Nuraje, N.; Zhang, L.; Chu, I. W.; Peetz, R. M.; Matsui, H.; Yang, N. L., Fast conductance switching in single-crystal organic nanoneedles prepared from an interfacial polymerization-crystallization of 3,4-ethylenedioxythiophene. *Adv. Mater.* **2007,** 19, (5), 669-672.

30. Joye, D. D., Shear rate and viscosity corrections for a Casson fluid in cylindrical (Couette) geometries. *J. Colloid Interface Sci.* **2003,** 267, (1), 204-210.

Chapter Six

1. Lee, S. Y.; Gao, X.; Matsui, H., Biomimetic and aggregation-driven crystallization route for room-temperature material synthesis: growth of b-Ga_2O_3 nanoparticles on peptide assemblies as nanoreactors. *J. Am. Chem. Soc.* **2007,** 129, (10), 2954-2958.